RED BLOOD CELL AGGREGATION CHARACTERIZATION: QUANTIFICATION AND MODELING IMPLICATIONS OF RED BLOOD CELL AGGREGATION AT LOW SHEAR RATES

by

Rym Mehri

Thesis submitted to the

Faculty of Graduate and Postdoctoral Studies

in Partial Fulfillment of the Requirements

for the Doctorate in Philosophy degree in Mechanical Engineering

Ottawa-Carleton Institute for Mechanical and Aerospace Engineering

Faculty of Engineering

University of Ottawa

Acknowledgements

Je tiens à remercier toutes les personnes grâce à qui la concrétisation de ce projet fut possible.
Je voudrais remercier tout d'abord mes deux superviseurs Dr. Catherine Mavriplis et Dr. Marianne Fenech pour leur encadrement et support professionnel et moral pendant toutes ces années. J'ai grandement bénéficié de leurs connaissances et expériences ce qui a enrichi mes propres connaissances dans le domaine. Je leur suis très reconnaissante pour leur dévouement, apports, contributions et leurs disponibilités tout au long de ce projet.
Je voudrais remercier spécialement toutes les personnes qui ont contribué à cette recherche dont Jérémie Laplante, Matt Laporte, et sans oublier Erfan Niazi, Sawyer Woodside, Jory Seguin and Reeham Hammouda. Je voudrais également remercier Dr. Marc Dubé et Dr. Laura Haya qui ont bien voulu fournir le POLYOX^{TM} WSR 301 et les sphère en verre, SPHERICELL. Je voudrais également remercier Rob Vandusen et Angela McCormick de "Carleton University MicroFabrication Facility". J'exprime aussi toute ma gratitude à mon beau-père Dr. Atef Kassem pour son aide, commentaires et support. Je remercie aussi toutes les personnes rencontrées dans le cadre de ces recherches et qui ont accepté de répondre à mes questions avec gentillesse.
Finalement, je dédie ce travail à mes parents Dr. Hechmi Mehri et Dr. Raoudha Mehri-Kamoun, mes modèles, qui m'ont encouragée et soutenue dans les moments les plus joyeux mais surtout les plus difficiles. Je tiens à leur exprimer toute ma reconnaissance pour m'avoir conduite à ce que je suis actuellement.
Ce travail a été financé par le CRSNG (Conseil de Recherches en Sciences Naturelles et en Génie du Canada) par le biais de la bourse d'études supérieures du Canada Alexander-Graham-Bell ainsi que par le biais de Dr. Catherine Mavriplis et Dr. Marianne Fenech. L'infrastructure a été financée par la fondation canadienne pour l'innovation (FCI) et les Fonds pour la recherche en Ontario (FRO) par le biais de Dr. Marianne Fenech. Les simulations numériques ont été effectuées grâce au support du "High Performance Computing Virtual Laboratory (HPCVL)", à l'Univesité Queen's aisni que "SciNet HPC Consortium" à l'Université de Toronto par le biais de Dr. Catherine Mavriplis.

Statement of Ethics Approval

The research involving human subjects that is reported in this thesis was conducted with the approval of the ethics committee of the University of Ottawa (H11-13-06).

Abstract

Mehri, Rym. Ph.D. University of Ottawa, May 2016. *Red Blood Cell Aggregation Characterization: Quantification and Modeling Implications of Red Blood Cell Aggregation at Low Shear Rates.* Supervised by Dr. Catherine Mavriplis, Ph.D and Dr. Marianne Fenech, Ph.D.

Red blood cells (RBCs) are the most abundant cells in human blood, representing 40 to 45% of the blood volume (hematocrit). These cells have the particular ability to deform and bridge together to form aggregates under very low shear rates. The theory and mechanics behind aggregation are, however, not yet completely understood.

The purpose of this work is to provide a novel method to analyze, understand and mimic blood behaviour in microcirculation. The main objective is to develop a methodology to quantify and characterize RBC aggregates and hence enhance the current understanding of the non-Newtonian behaviour of blood at the microscale. For this purpose, suspensions of porcine blood and human blood are tested *in vitro* in a Poly-di-methylsiloxane (PDMS) microchannel to characterize RBC aggregates within these two types of blood. These microchannels are fabricated using standard photolithography methods. Experiments are performed using a micro Particle Image Velocimetry (μPIV) system for shear rate measurements coupled with a high speed camera for the flow visualization. Corresponding numerical simulations are conducted using a research Computational Fluid Dynamic (CFD) solver, Nek5000, based on the spectral element method solution to the incompressible non-Newtonian Navier-Stokes equations. RBC aggregate sizes are quantified in controlled and measurable shear rate environments for 5, 10 and 15% hematocrit. Aggregate sizes are determined using image processing techniques. Velocity fields of the blood flow are measured experimentally and compared to numerical simulations using simple non-Newtonian models (Power law and Carreau models).

This work establishes for the first time a relationship between RBC aggregate sizes and corresponding shear rates in a microfluidic environment as well as one between RBC aggregate sizes and apparent blood viscosity at body temperature in a microfluidic controlled environment. The results of the investigation can be used to help develop new numerical models for non-Newtonian blood flow, provide a better understanding of the mechanics of RBC aggregation and help determine aggregate behaviour in clinical set-

tings such as for degenerative diseases like diabetes and heart disease.

Keywords:
red blood cell aggregation, erythrocytes, aggregate sizes, blood, microchannel, non-Newtonian, controlled shear rate, μPIV, blood viscosity, spectral element method.

Table of Contents

List of Tables

List of Figures

List of Symbols

a	Shape parameter
amp	Amplitude
A $[\mu m^2]$	Cross-sectional area of blood layer
A_{exp} $[\mu m^2]$	Cross-sectional area of the microchannel branch
$A_{projected}$ $[\mu m^2]$	Projected area of one aggregate
A_{sim}	Cross-sectional area of simulation microchannel branch
AI	Aggregation index
$Area_A$	Area of light reflectance
$Area_B$	Area of light transmittance
ASI	Aggregation size index
ASP	Aggregation shape parameter
c $[Pa.s]$	Plastic viscosity
C_p $[J/K]$	Heat capacity
$C(x, y)$	Cross-correlation function
$d_{particle}$ $[\mu m]$	Diameter of the fluorescent particle
D_H $[\mu m]$	Hydraulic diameter
dt $[\mu s]$	Time between two frames
$Entities_{count}$	Number of entities in non-aggregating blood
f $[N]$	Forcing function
$F(y, z)$ $[\frac{\mu m}{s}]$	Three-dimensional velocity profile
h $[\mu m]$	Depth of microchannel
$H_{estimated}$	Estimated hematocrit
$I(x, y)$	Image intensity of frame 1
$I'(x, y)$	Image intensity of frame 2
k	Casson model constant
K $[cP]$	Fluid consistency index
$\mathbb{L}$	Simulation length
$\mathcal{L}$	Simulation length scale
L_n	n^{th} order Legendre polynomial
$\mathbb{M}$	Simulation mass
$\mathcal{M}$	Simulation mass scale

MAI	Microscopic aggregation index
$Meas$	Measurement
n	Non-Newtonian behaviour index
n_{images}	Total number of recorded images
N	Highest order of polynomial
N_{RBC}	Number of Red Blood Cells
NA	Numerical Aperture
$pixel_{im}$	Intensity of any pixel in image im
P	Pressure
Pe	Perimeter of blood layer
$Peri\ [m]$	Perimeter of one aggregate
q	Generic variable (e.g. Velocity, pressure or viscosity) to express as a polynomial expansion in *Nek5000*
$Q\ [\frac{\mu L}{hr}]$	Total flow rate in the channel
$Q_{exp}\ [\frac{\mu L}{hr}]$	Experimental flow rate in the microchannel branch
Q_{sim}	Simulated flow rate in the microchannel branch
$Q_1\ [\frac{\mu L}{hr}]$	Flow rate of reference fluid
$Q_2\ [\frac{\mu L}{hr}]$	Flow rate of test fluid
R^2	Coefficient of determination or R-squared
$R^2_{adjusted}$	Adjusted coefficient of determination
RBC_{count}	Entities in aggregates
$T\ [K]$	Temperature
$\mathbb{T}$	Simulation time
$\mathcal{T}$	Simulation time scale
Th	Threshold
$u\ [\frac{mm}{s}]$	Streamwise velocity
$\mathbf{u}$	Simulation velocity vector with components (u,v,w)
$V_{bloodlayer}\ [\mu m^3]$	Volume of blood layer
$V_{RBC}\ [\mu m^3]$	Volume of one red blood cell
$V_{interface}\ [\frac{mm}{s}]$	Velocity at the interface
$V_{wall}\ [\frac{mm}{s}]$	Velocity at the microchannel wall
$w\ [\mu m]$	Width of the microchannel
$w_b\ [\mu m]$	Width of the microchannel branches
$w_1\ [\mu m]$	Width of the PBS layer
$w_2\ [\mu m]$	Width of the blood layer
$x\ [\mu m]$	Position along the channel length

y $[\mu m]$	Position across the channel width
y' $[\mu m]$	Position across the channel branch width
y^*	Dimensionless position across the channel width
$y_{interface}$ $[\mu m]$	Location of interface across the channel
y_{wall} $[\mu m]$	Location of wall across the channel
Y	Dimensionless location of the fluid interface
z $[\mu m]$	Position across the channel depth
α_{conv} $[\frac{mm}{px}]$	Conversion factor
β	Microchannel aspect ratio
$\dot{\gamma}$ $[s^{-1}]$	Shear rate
δ_b	Precision error
δ_p	Bias error
δ_T	Total measurement uncertainty
λ	Relaxation time
λ_{abs} $[nm]$	Absorption wavelength of fluorescent particle
$\lambda_{emission}$ $[nm]$	Emission wavelength of fluorescent particle
μ_{app} $[cP]$	Apparent viscosity of blood
μ_{exp} $[cP]$	Experimental viscosity
μ_{inf} $[cP]$	Infinite shear viscosity
μ_H $[Pa.s]$	Viscosity of blood at high shear rate
μ_L $[Pa.s]$	Viscosity of blood at low shear rate
μ_p $[cP]$	Plasma viscosity
μ_{sim} $[cP]$	Simulation viscosity
μ_0 $[cP]$	Zero shear viscosity
μ_1 $[cP]$	Viscosity of reference fluid
μ_2 $[cP]$	Viscosity of test fluid
$\mu^j{}_{fit}$ $[cP]$	Viscosity of the fitted data point j
ρ	Simulation density
τ $[Pa]$	Shear stress
τ_y $[Pa]$	Yield stress
ϕ	Passive scalar

List of Acronyms

AAS	Average Aggregate Size
BGK	Bhatnagar-Gross-Krook
CAD	Computer-Aided-Design
CCD	Charged-Coupled Device
CFD	Computational Fluid Dynamics
CFL	Cell Free layer
DOC	Depth Of Correlation
DOF	Depth Of Field
DPD	Dissipative Particle Dynamic
EDTA	Ethyleneiaminetetraacetic
ESR	Erythrocyte Sedimentation Rate
FEM	Finite Element Method
GL	Gauss-Legendre
GLL	Gauss-Lobatto-Legendre
H	Hematocrit
Hb	Hemoglobin
IBM	Immersed Boundary Method
IFEM	Immersed Finite Element Method
LBM	Lattice Boltzmann Method
LD-RBC	Low-Dimensional Red Blood Cell
LDV	Laser Doppler Velocimetry
LR	Light reflection
LT	Light Transmission
MAS	Mean Aggregate Size
MD	Molecular Dynamics Method
NO	Nitric Oxide
N-S	Navier-Stokes
PBS	Phosphate Buffered Saline
PDMS	Poly-Di-Methyl-Siloxane
PETG	Polyethylene Terephthalate glycerol
PIV	Particle Image Velocimetry

PMMA	Poly(methyl methacrylate)
RBCs	Red Blood Cells
RGB	Red-Green-Blue
RKPM	Reproducing Kernel Particle Method
RMS	Root Mean Square
RMSE	Root Mean Square Error
SEM	Spectral Element Method
WBCs	White Blood Cells
WLC	Wormlike chains
WSR	Water Soluble Resin
2D	Two-dimensional
3D	Three-dimensional
μPIV	Micro Particle Image Velocimetry

Chapter 1

Introduction

1.1 Motivation and purpose of research

Human blood is a complex biofluid that performs essential tasks in our bodies. It is responsible, *inter alia*, for oxygen and nutrient delivery as well as waste removal such as carbon dioxide. Blood is composed of several cells: Red Blood Cells (RBCs, also known as erythrocytes), White Blood Cells (WBCs, also known as leukocytes) and platelets (or thrombocytes) suspended in blood plasma. RBCs are the most abundant cells in blood. They occupy 40 to 45% of the blood volume, whereas the WBCs and platelets represent less than 1% of the blood volume. The rest (55%) is occupied by blood plasma. Due to the presence of RBCs, blood represents one of the most challenging fluids to understand, analyze and model.

Understanding RBC behaviour is of a great interest to the field of hemorheology, which is the study of blood flow properties, since RBCs play a crucial role in determining the rheological properties of blood. They are almost singularly responsible for the particular blood behaviour, due to their unique properties. Healthy RBCs are able to deform and adapt to any vessel diameter in the human body. They also have the ability to assemble and form entities called aggregates (three-dimensional) or "rouleaux" (one-dimensional). The formation of these aggregates dictates the variation of blood viscosity, particularly in microcirculation. An example of these entities is shown in Fig. 1.1.

Due to its two phase flow nature and the aggregates' presence, blood is considered as a non-Newtonian fluid, whose behaviour at the microscales still requires investigation. In fact, the mechanism of RBC aggregation has not yet been completely understood. It is known, however, that RBCs aggregate under extremely low shear rates (defined as the velocity gradient within the flow) and tend to disaggregate when subjected to higher shear rates on the order of 20 to 40 s^{-1}. Viscometric studies [1–5] have demonstrated the existence of an inverse relationship between shear rate and aggregate sizes. Therefore,

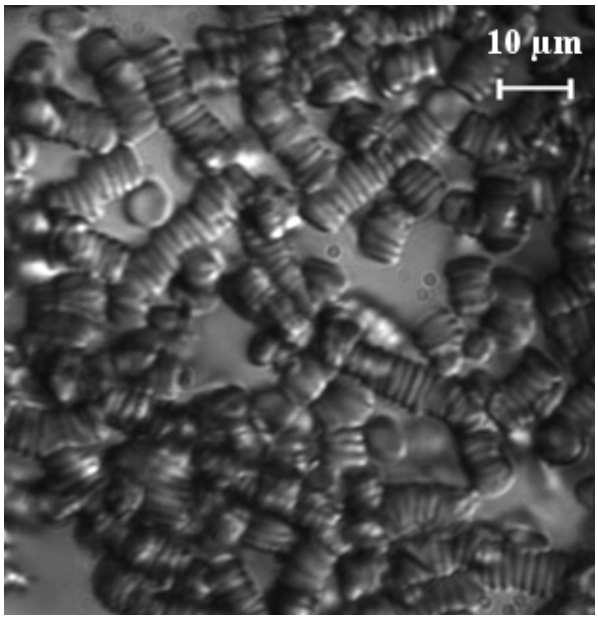

Figure 1.1: Red Blood Cell rouleaux.

aggregation size is an important factor in understanding the microrheological behaviour of blood. Measuring RBC aggregates presents a challenge in the hemorheology field, due to the varying nature of blood, not only from person to person but from day to day. Hence, a controlled method is needed in order to analyze more efficiently and more precisely RBC aggregates.

Numerous studies have attempted to understand and analyze the mechanism of RBC aggregation. Degrees of aggregation have been determined based on several methods, such as erythrocyte sedimentation rate, microscopic aggregation index and syllectometry methods [6, 7]. While these methods provide several indirect indices of RBC aggregation allowing to study RBCs at stasis, they do not provide sufficient information to understand the microrheological behaviour of blood dynamically in the microcirculation.

Few studies, however, have attempted to determine the degree of aggregation under controlled flow conditions [8–10]. These studies indirectly investigated RBC aggregate sizes by determining the ratio of the occupied space in a shearing system, measured from microscopic blood images. This provides information on the degree of aggregation as well as the local viscosity. Chen *et al.* [11] presented a direct measurement technique for RBC aggregate sizes and provided RBC aggregate size distributions for different shear stresses by varying the flow rate of the suspensions while monitoring the pressure drop across a

flow chamber. The shear stresses are calculated based on the monitored pressure using Stokes' equation. These previous studies demonstrated the existence of a relationship between RBC aggregates and the shear stress within the flow. However, since blood is non-Newtonian, *i.e.* having a variable viscosity, it has not been possible to directly relate aggregate sizes to the shear rate applied. A direct correlation between applied shear rate and RBC aggregation is needed to enhance the understanding of the RBC aggregation mechanism.

Numerical studies have been a great tool for investigation and modelling of RBC deformability and aggregation to understand the behaviour of RBCs under physiological and pathological conditions [12–18]. However, large discrepancies between numerical model and experimental results still exist. Therefore, there is a need to develop a non-Newtonian model for blood based on experimental data, accounting for the behaviour of RBC aggregates in microcirculation.

1.2 Thesis statement

This thesis proposes a new method to analyze blood behaviour in microcirculation by characterizing RBC aggregates at these microscales. The work presented is based on the system designed by Mehri *et al.* [19], where RBC aggregates from different blood suspensions were investigated qualitatively under controlled and measurable shear rates. A simple and efficient methodology is developed in order to quantify aggregates in microcirculation. Numerical simulations are combined with image processing techniques, micro Particle Image Velocimetry measurements and optical viscometry techniques to investigate and determine RBC aggregate sizes and viscosity under specific and controlled conditions: those of constant shear rates. Suspensions of porcine and human blood are tested experimentally (*in vitro*) and numerically (using Power law and Carreau models) in a double Y-microchannel. The ultimate goal of this research is to reveal a relationship between RBC aggregate sizes and corresponding shear rates. The results obtained from this research may contribute to advancement in the hemorheology field by providing an experimental based-model for blood flow accounting for RBC aggregates to be incorporated into numerical models.

With this work, we present a new procedure that directly quantifies RBC aggre-

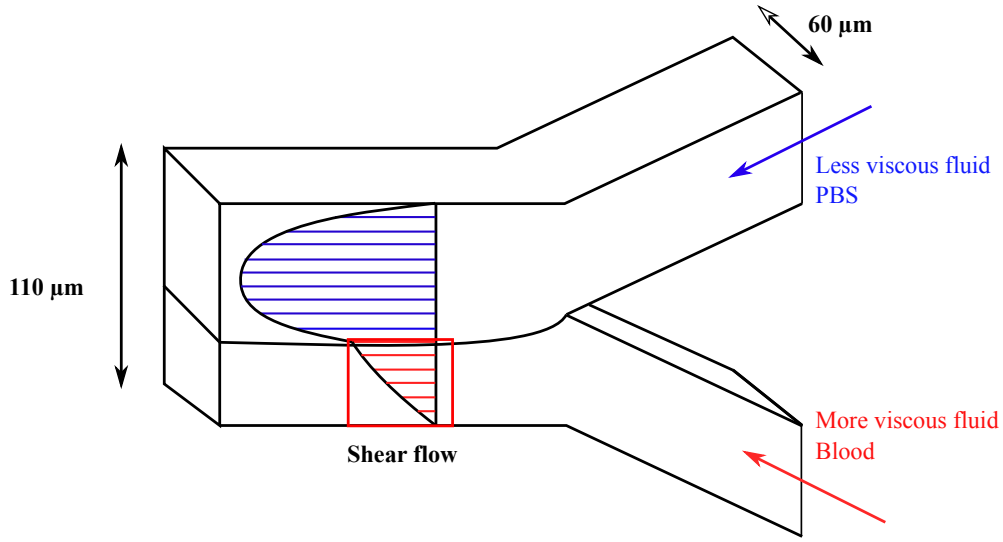

Figure 1.2: Blood entrained by Phosphate Buffered Saline (PBS) in a double Y-microchannel configuration creating a shear flow within the blood layer.

gates in microcirculation, dynamically, under controlled and constant shear rates and provides quantitative results relating RBC aggregate size to the shear rate applied in a controlled microscopic environment. In this procedure, RBC-suspensions are entrained in a double Y-microchannel (as illustrated in Fig. 1.2), with a Phosphate Buffered Saline (PBS) solution hence creating a shear flow in the blood layer. Within this blood layer a controlled measurable shear rate can be obtained. The RBC-suspensions are tested at different hematocrit levels (H), which represent the percentages by volume of RBCs in blood, (5%, 10% and 15% H), under different shear rates (2.8-74 s^{-1}) at room and body temperature ($T = 23°C$ and $T = 37°C$, respectively). Low hematocrits were used in this study to mimic the microcirculation local hematocrit that does not exceed 20% [20]. The blood velocity and shear rate are determined using a micro Particle Image Velocimetry (μPIV) system while the flow is visualized using a high speed camera. The viscosity is determined based on the theory of optical viscometers with co-flowing fluids [21–25]. The blood flow is directly observed in the shearing system normal to the velocity variation hence providing a different angle for the flow investigation compared to the previous studies, where the visualization of the aggregates was done in the direction of the velocity variation. When the flow is observed in the direction of the velocity variation, the RBC aggregates appear to overlap since they flow at different velocities within the different planes, whereas the current method does not allow for the cells to overlap. The proposed

method also allows the visualization of the entire domain while previous studies only observe a small portion of the domain. The results obtained are then processed based on the image intensities in order to detect the RBCs and determine the aggregate sizes. The aggregate sizes and viscosity are then related to the corresponding shear rate for each flow condition. Results at room temperature can serve for the design of lab-on-a-chip devices, providing a relationship between viscosity, shear rate and aggregate sizes.

1.3 Thesis outline

The document is organized as follows; the present chapter provides a brief introduction to the thesis and the motivation for the research. It also provides a broad introduction to blood, its properties and characteristics.

Chapter 2 presents an overview of the previous studies performed in the hemorheology field, more specifically concerning RBCs and RBC aggregates in microcirculation.

Chapter 3 provides a complete and detailed description of the methodology and materials used experimentally as well as numerically.

In Chapter 4, validation of the image processing code, the viscosity measurement technique and the non-Newtonian implementation of the numerical code is provided.

Chapter 5 presents the major thesis findings including experimental data of porcine and human blood as well as the numerical data obtained using the experimental data, for different temperatures.

Chapter 6 provides a relevant and detailed discussion of the results obtained in Chapter 5 with possible factors affecting the experimental findings. Uncertainties of the experimental work are also provided in Chapter 6.

Finally, the ensuing contributions to the hemorheology field are summarized in Chapter 7, with perspectives for future investigations.

1.4 Background: blood properties

Human blood is a biofluid composed of several elements suspended in a Newtonian fluid known as plasma. The elements consist of White Blood Cells (WBCs) or leukocytes, platelets or thrombocytes and Red Blood Cells (RBCs) or erythrocytes. This study focuses on RBCs as well as their properties and aggregation.

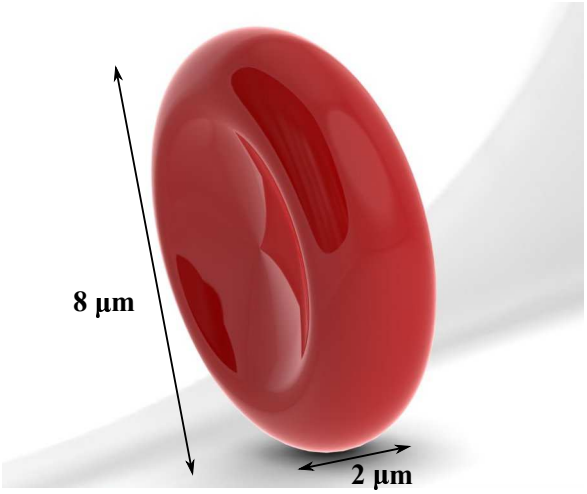

Figure 1.3: Geometry of a single Red Blood Cell.

1.4.1 Geometry and properties of RBCs

In a healthy individual, RBCs represent biconcave discs with an approximate diameter of 8 μm and a thickness of 2 μm [26], as shown in Fig. 1.3. RBCs have a volume of about 90 μm^3 for a surface area of about 140 μm^2, which represents a large surface area to volume ratio, about 40% larger than the ratio for a sphere. This large surface to volume ratio, combined with membrane flexibility, provides the RBCs with the ability to adapt to any vessel geometry in the body. Under normal conditions, in the human body, $20-30\times10^{12}$ RBCs (5×10^6 RBC per microliter) are contained in blood to occupy 40 to 45% of the blood volume. Low hematocrit is usually a symptom of anemia, while an excessive blood hematocrit is an indication of polycythemia which is described as an unusual increase of the RBC count [27].

1.4.2 Function

The main function of the RBCs is to transport oxygen from the lungs to the rest of the tissues and organs and to then carry carbon dioxide from the organs to the lungs. The heart, acting as a pump to deliver blood to the organs, makes the transport of oxygen and carbon dioxide possible within 30 to 45 seconds. RBCs carry oxygen and carbon dioxide via the hemoglobin molecule (Hb) that represents one third of the RBC volume. The iron contained in this molecule provides the red colour of RBCs. In 1960, Perutz [28] noted that Hb is, in fact, a conjugated protein, with a non-protein part attached to

it. It represents four polypeptide components attached to four heme groups, where an iron atom can be found at the center of each heme group. The oxygen collected from the lungs is then able to attach to the ferric portion of the molecule allowing up to four molecules to be connected. The binding of oxygen greatly depends on oxygen pressure. However, carbon dioxide is only able to bind to the polypeptide chains [27]. Due to the absence of inner cell material, such as mitochondria and the nucleus, RBCs do not consume the oxygen being carried. This absence of inner cell material allows the cells to have the biconcave geometry thus providing a large surface to volume ratio. This ratio is important since it provides a better and quicker diffusion of oxygen in Hb. The life time of a RBC is about 125 days: during that time, it performs its function. At the end of their lives, RBCs disintegrate due to the macrophages present in blood, leaving the iron that is transported to the bone marrow to generate new erythocytes, a process known as erythropoiesis.

1.4.3 Membrane mechanics and deformation

Erythrocytes have been the focus of several studies in order to understand their great capabilities and unique properties. In fact, one of the most impressive characteristics of RBCs is their ability to deform and adapt to the smallest vessel diameters such as capillaries. In order to meet with the demands of the function and to reach the capillary network, the RBC membrane needs to simultaneously be strong and flexible. This strength and flexibility of the cell membrane is due to the protein networking of the inner layer of the membrane known as the membrane skeleton as shown in Fig. 1.4. Vera *et al.* described it as "a microscopic geodesic dome" [29]. The structure of the RBC membrane consists of three distinct layers: the outer layer, which is rich in carbohydrates, the lipid bilayer, mainly composed of lipid molecules, and the inner layer, containing of the structural protein network that represents the membrane skeleton. This membrane skeleton is a network of roughly 33,000 protein hexagons [29]. A closer look at the inner structure of the protein network reveals that it is mainly composed of two proteins, spectrin and actin, that give the membrane its elasticity and strength. The RBC membrane has been shown to be 100 times more elastic than a latex membrane of the same thickness [30] but also very viscoelastic with a surface viscosity of about $10 \times 10^{-3} \frac{dyn.s}{cm}$ ($10^{-3} Pa.s$) [31, 32].

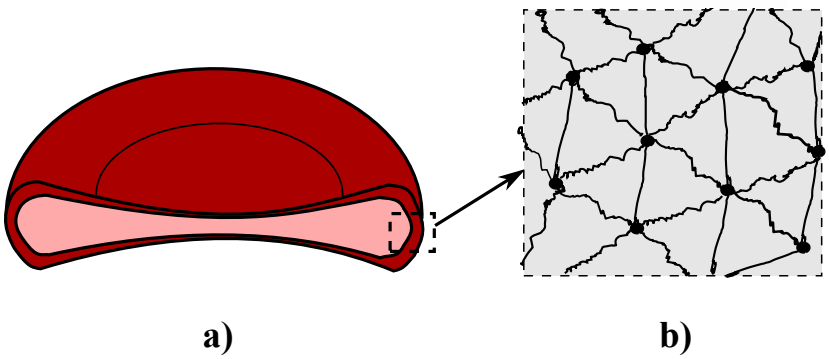

Figure 1.4: Red blood cell section (a) and protein networking structure of membrane inner layer.

This deformability is of physiological significance since it enables RBCs to flow in vessels of diameters as small as 4 μm in the body. Reduction in cell deformability also results in reduction of RBC aggregation.

The RBC membrane surrounds the inner fluid which is a solution of Hb (containing 33% of Hb). This solution behaves as a Newtonian fluid with a viscosity of about 6 to 7 cP [33] with an average density of RBCs of about $1096\frac{Kg}{m^3}$. [33]

1.4.4 Aggregation of RBCs

Another major characteristic of RBCs is their ability to aggregate at low appropriate shear rates as described in Section 1.1. Blood aggregation was first observed and described by Fåhraeus in 1921 [34], where the relationship between the aggregate formation and the sedimentation rate was investigated. From Fåhraeus's research, the structure of aggregates in healthy and non-healthy individuals was clearly differentiated. However, the research of Fåhraeus only included observations of stationary blood and RBC aggregates contained within two microscope slides. *In vivo* experiments were subsequently carried out in order to visualize blood behaviour in vessels [35–38]. These studies focused on the visualization of the *bulbar conjunctiva*[1] in anaesthetized healthy and non-healthy humans and rats. They provided evidence that, in the capillary vessels, RBCs do not aggregate but flow as individual cells. Also, depending on the pathological conditions, blood will behave differently.

[1]Membrane covering the anterior portion of the eyeball

The mechanism of RBC aggregation has yet to be completely understood. There are two theories, nowadays, that explain the aggregation of RBCs: 1) the bridging of cells due to the cross-linking of the macromolecules [39] and 2) the force attraction caused by depletion of the molecules due to the osmotic gradient [40]. The former theory states that aggregation is due to the bridging of the cells by the cross-linking of the macromolecules [39] and that aggregation occurs when the bridging force is greater than the forces due to electrostatic repulsion, membrane strain and mechanical shearing [40]. The latter theory affirms that the aggregation mechanism is due to the osmotic gradient that is caused by the relative depletion of molecules near the cell surface with respect to the suspending fluid [40]. This osmotic gradient engenders an attraction force between the cells that causes aggregation.

1.4.4.1 Effect of plasma protein on aggregation

Due to the complexity of blood flow, further studies were performed in order to investigate and understand the rouleaux formation. Studies such as Merrill *et al.* [41] investigated the effect of fibrinogen on RBC aggregation by removing elements from blood plasma and observing the rheological properties of blood. Chien *et al.* [42] investigated the aggregation ability of several proteins and molecules in plasma and showed that globulin also plays a role in RBC aggregation, while albumin has no effect on aggregate formation. When blood plasma is replaced with Ringer's solution, such as Phosphate Buffered Saline (PBS), where no proteins or macromolecules are contained within the suspending fluid, no RBC aggregation was observed [43]. Rouleaux formation is greatly affected by the protein and macromolecules present in plasma, however, it has been shown that RBC aggregation can be affected by unnatural molecules. Chien and Jan [39] presented a study of erythrocytes suspended in Ringer's solution where polyglucose Dextran, at different molecular weights, was added. They explored the relationship between the spaces between RBC aggregates and the Dextran molecular weight. They observed that Dextran, having a molecular weight above 40 kDa (kilodalton), induced RBC aggregation, while below 40 kDa, the solution actually inhibited aggregation. In fact, Dextran affected the electronegativity of erythrocytes which has a great effect on rouleaux formation. Dextran induced aggregation mechanism does not only depend on

the molecular weight of Dextran but also on its concentration in blood. The Dextran induced aggregation increases with increasing concentration of Dextran until reaching a limit that inhibits aggregation, whereas the fibrinogen induced aggregation increases constantly with increasing the fibrinogen concentration [44].

1.4.4.2 Effect of shear rate on aggregation

Several other factors greatly affect erythrocyte aggregation. Shear rate represents one of the most important factors influencing rouleaux formation. In fact, viscometric studies [1–5] show that shear rate or aggregation force is inversely related to aggregate size but also that such aggregates are usually only seen for low shear rates. However, the aggregation force is not completely defined, in that there is no predetermined factor to provide sufficient information to describe RBC aggregates. On the other hand, the disaggregation force is easily defined [45]. Under normal conditions, rouleaux disaggregate when subjected to shear rates ranging from 20 to 40 s^{-1} causing RBCs to flow separately.

1.4.4.3 Effect of hematocrit on aggregation

RBC aggregation is also hematocrit dependent. Kim *et al.* [46, 47] investigated the link between the collision rate of erythrocytes and the degree of aggregation. They found that the number of RBCs present within the medium greatly affects the collision rate since the fewer the number of cells, the lower the probability of the RBCs to encounter, collide and initiate rouleaux formation, thereby decreasing aggregation. Experimental studies, conducted on healthy individuals with blood samples at different hematocrit subjected to different flow rates, showed that hematocrit has a significant effect on viscosity at high shear rate (above 10 s^{-1}), but that this effect is more significant for very low shear rates (below 1 s^{-1}) [48]. Moreover, the biconcave discoid shape of the RBCs as well as the membrane elasticity can also affect the aggregability of RBCs. In fact, the shape and elasticity of the cell provide the required geometry and freedom to adapt to the adjacent cell and increase aggregation probability. A small variation in shape, caused by a change in osmotic pressure [49], or an increase in cell rigidity [50], could decrease RBC aggregation.

1.4.4.4 Effect of temperature on aggregation

Temperature is also an important factor that influences RBC aggregation. Viscosity is shown to decrease with increasing temperature but the effect of temperature on viscosity increases with decreasing shear rate [45, 51]. It is also known that temperature greatly affects the aggregation mechanism. Neumann *et al.* [52] did show the temperature dependence on RBC aggregation and stated that a decrease in temperature engenders a higher resistance of the RBC aggregates to the hydrodynamic dispersion and hence would increase the absorption energy of the aggregates due to an increase in molecular adsorption stress. However, this temperature dependence was not directly related to RBC aggregate sizes.

1.4.4.5 Effect of aggregation on blood viscosity

These different RBC aggregation behaviours greatly affect the behaviour of the whole blood. One effect that can be visualized and clearly noted is blood sedimentation. Due to the difference in density between cells and plasma, RBCs will settle in the suspended medium. However, the rate of sedimentation depends on the collision rate of RBCs and therefore rouleaux formation. In fact, sedimentation rate has been used as a tool to estimate aggregation properties but is also an indication of the nature of the sample (healthy or pathogenic), as will be detailed in Section 1.4.5. Another important consequence of RBC aggregation is the variable viscosity and hence the non-Newtonian behaviour of blood, as will be detailed in Section 1.4.6. As mentioned previously, the shear rate and hematocrit, having opposite effects on RBC aggregation, have been shown to greatly affect the viscosity of blood [48].

1.4.5 Measurement of RBC aggregation

It is important to quantify these aggregates in order to understand their behaviour under physiological, and most importantly, pathological conditions. Rouleaux formation has been shown to be altered by several factors such as inflammatory or infectious conditions, cardiovascular diseases, genetic disorders and chronic diseases [45]. The major factors considered in several studies in order to qualitatively and quantitatively describe RBC

aggregation are the rate of rouleaux formation, the number of RBCs per aggregate and the force required to hold these entities together. The different methods presented in the following sections focus on determining different aspects of RBC aggregation.

1.4.5.1 Erythrocyte sedimentation rate

The erythrocyte sedimentation rate (ESR) method evaluates blood phase separation. This method was first introduced by Biernacki in 1897 who noted that the phase separation rate increased under pathological conditions [53]. The method was further developed by Fåhraeus [34] and is currently used as an index of inflammation and a screening method. Sedimentation of RBCs in plasma occurs due to the difference in density of plasma and cells under the influence of gravity [54]. The mechanism behind this method is based on Stokes' law where the rate of sedimentation of a particle is proportional to its cross-sectional area and thus the square of the particle's radius. If the particles are dispersed in plasma, the ESR is very low; however, an increase in particle diameter (such as for RBC aggregation) increases the sedimentation rate.

The techniques used in clinical settings include the Witrobe and Westergren methods. In general, these methods consist of measuring the plasma in the tube after a settling period of 60 minutes. The difference between the two methods mentioned is the tube used for the experiment as well as the anticoagulant used for blood. Experimentation performed on healthy individuals between the ages of 17 to 50 years provided an ESR of 10 $\frac{mm}{hr}$ for men and 12 $\frac{mm}{hr}$ for women [55]. Potron *et al.* explored the link between the ESR and RBC aggregation [56] and discovered the existence of a relationship by way of correlations between these two factors [57]. However, a direct link between these two factors could not be determined.

1.4.5.2 Low shear viscosity

The low shear viscosity method is based on the rheology of blood at very low shear rates, below 1 s^{-1} [55]. It uses the technique of viscometry with a viscometer capable of measuring viscosity of blood at low shear rates (rotational viscometer and scanning capillary viscometer [58]). Using this method, the aggregation index, AI, is defined using Eq. (1.1):

$$AI = \frac{\mu_L - \mu_H}{\mu_H} \tag{1.1}$$

where μ_L represents the viscosity at low shear rates and μ_H the viscosity at high shear rates [45]. The low shear viscometry method also provides an index of aggregation and an indirect link between the aggregate size and the shear rate applied in a microfluidic environment. However, this approach may provide altered results of aggregation indices due to RBC deformation. In fact, erythrocyte deformability is related to their ability to aggregate but also has an important effect on the blood viscosity especially at low shear rates.

1.4.5.3 Microscopic aggregation index

The microscopic aggregation index method consists in directly visualizing blood under the microscope to deduce the degree of RBC aggregation, more specifically, to determine the number of RBC per aggregate. The methodology is as follows: first diluted RBC suspensions of about 1% hematocrit in aggregating and non-aggregating media are placed into a hemocytometer chamber and left to settle for 10-15 minutes. The entities in both the aggregating ($Entities_{count}$) and non-aggregating (RBC_{count}) media, including single RBC and rouleaux, are visually counted within the microscopic area [39]. The microscopic aggregation index (MAI) is defined using Eq. (1.2):

$$MAI = \frac{RBC_{count}}{Entities_{count}} \tag{1.2}$$

where RBC_{count} represents the RBCs count in the non-aggregation medium and $Entities_{count}$ the aggregates count in the aggregating medium. The MAI increases with the degree of RBC aggregation since $Entities_{count}$ decreases with increasing the degree of aggregation. This method presents a good indication of the RBC aggregation, however, it does not provide information on the aggregation rate. Another main disadvantage lies in the non-automated and manual counting of RBCs (visually), which can be time consuming [45].

1.4.5.4 Image analysis technique

In order to improve the microscopic aggregation index method, image analysis techniques are used in order to estimate RBCs in each medium in an automated manner. Using these techniques, it is possible to quantitatively study RBC aggregation at stasis (at rest) and under several shear stresses in order to better mimic aggregation behaviour *in vivo*. Since RBCs can be clearly visualized and captured with the digitized system, aggregate shapes can also be investigated along with aggregate sizes. According to Foresto *et al.* an aggregation shape parameter (ASP) can be defined using Eq. (1.3) [59]:

$$ASP = 4\pi \frac{A_{projected}}{Peri^2} \tag{1.3}$$

where $A_{projected}$ represents the projected area of one aggregate and $Peri$, the perimeter of one aggregate. For a perfectly spherical aggregate, which is rarely seen, the ASP is at its maximum and will decrease for cylindrically shaped aggregate structures. Rotstein *et al.* used a different method based on a digitized image analysis technique in order to estimate the aggregate size of blood at stasis [60]. They affirmed that the space between adjacent RBC aggregates, known as the vacuum radius, is a direct indicator of RBC aggregate sizes. Chen *et al.* [11] used a computerized image analysis technique in order to provide RBC aggregate size distribution for different shear stresses by varying the flow rate of the suspensions in the flow chambers while monitoring the pressure drop across these chambers. From this study, the average aggregation size, the peak aggregation size, the aggregation kinetics and the disaggregation force were related and described in terms of the shear stress calculated based on the pressure drop applied. Kavitha and Ramakrishnan [61] applied a two-dimensional wavelets transform to study RBC aggregates. They defined the Aggregation Size Index (ASI) to be the standard deviation of the coefficients generated by the wavelet functions, since it was shown to be directly proportional to the aggregation size.

1.4.5.5 Syllectometry method

The syllectometry method consists of two similar approaches to quantify RBC aggregates: light transmission [6] and light reflection [7]. The light transmission method (LT) is based

on the intensification of light when transmitted through RBC aggregates, while the light reflection method (LR) is based on the diminishing of light intensity when reflected from RBC aggregates. The higher the degree of aggregation, the larger the spaces forming between the rouleaux in the medium. Consequently, the higher the degree of RBC aggregation, the more light is allowed to pass within the gaps separating aggregates and thus the less light is being reflected. Using the syllectometry method, two major aggregation aspects can be investigated: information on aggregation size, shape and the start time of the mechanism can be obtained based on light intensity as well as the time required for this aggregation process, a major factor in diseases diagnosis. In fact, the difference between light intensities, known as amplitude (amp), determined at stasis and low shear rates, provides information on the aggregation morphology and size but not on the rate of the aggregation process. However, parameters such as the aggregation index provide information on the aggregation rate independently from the aggregation morphology. For the LT method, AI can be expressed as follows:

$$AI = \frac{Area_B}{Area_A + Area_B} \times 100 \tag{1.4}$$

whereas, for the LR method, AI is written as follows:

$$AI = \frac{Area_A}{Area_A + Area_B} \times 100 \tag{1.5}$$

where $Area_A$ represents the area for light reflectance and $Area_B$ represents the area for light transmittance. Illustrations of the LT and LR methods are shown in Fig. 1.5. Another major index of RBC aggregation that can be extracted from this method is the disaggregation maximum shear rate value that represents the value of shear rate at the maximum LT or minimum LR [62].

1.4.5.6 Ultrasound backscattering method

The ultrasound backscattering method is based on the Rayleigh scattering theory where scattering is dependent on the ultrasound signal [63]. Cloutier and Qin state that RBCs or RBC aggregates flowing in plasma will act as ultrasound scattering entities where the backscattering is proportional to the volume of the cell or aggregate [64]. Therefore, the

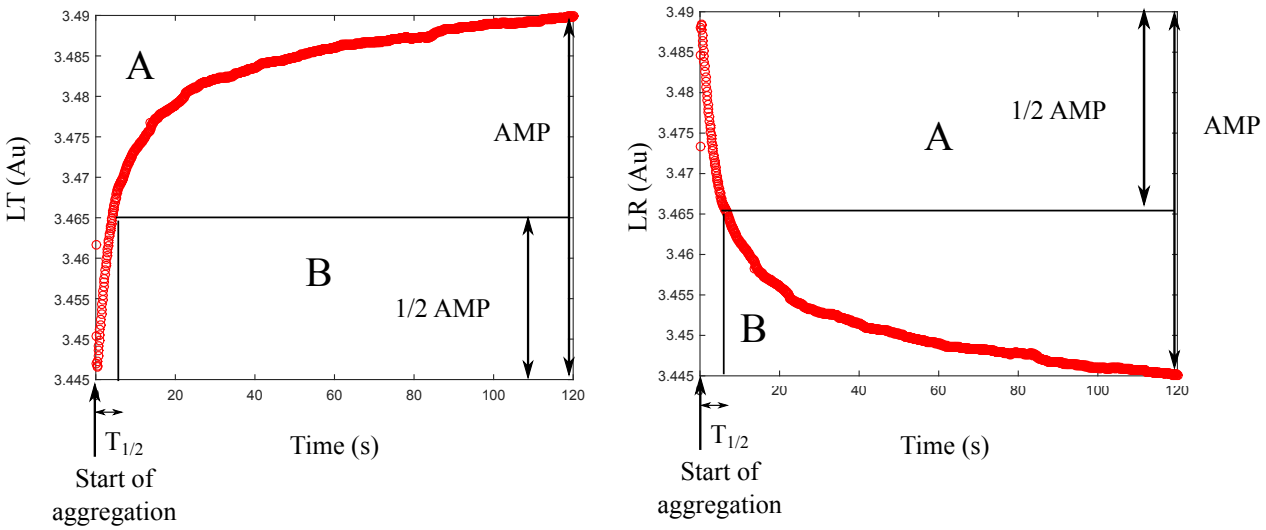

Figure 1.5: Analysis of the time course of (a) light transmittance (LT) and of (b) light reflectance (LR) (b). A and B denote the areas above and below the syllectogram curve and are shaded in different gray tones. LT and LR are expressed in arbitrary units (au). AMP represents the difference between light intensities.

backscattering coefficient increases with increasing RBC aggregability and thus decreases for high shear rates.

The methods presented above provide relevant information (in the form of several indices) on the aspects of aggregation but, except for the study of Chen *et al.* [11], no standard method exists to quantify RBC rouleaux under controlled and measurable shear rates.

1.4.6 Non-Newtonian behaviour

The density of blood is about 1060 $\frac{kg}{m^3}$ and its viscosity, at high shear rate (larger than 50 s^{-1}), is approximately 3 cP. However the viscosity of blood is not constant in time or space, but greatly depends on several factors, which leads to the non-Newtonian behaviour of blood. Blood viscosity, *in vivo*, depends on the shear rate, the plasma viscosity, the hematocrit, as well as the geometry and diameter of the vessels [2, 65]. It is known that for large vessels, such as arteries and veins with diameters larger than 300 μm, the apparent viscosity of blood is almost constant at approximately $\mu_{app} = 3$ cP [66]. Therefore, at this macroscale, blood can be considered as a Newtonian fluid and as

a homogeneous mixture. Aggregation, which considerably affects the viscosity of whole blood, is the major factor for the non-Newtonian behaviour of blood. Therefore, factors affecting rouleaux formation affect blood viscosity. These factors include the composition of the suspension medium, the elasticity of RBC membranes, hematocrit of blood and the shear rate applied as detailed in Section 1.4.4.5. However, blood viscosity, *in vivo*, does not only depend on the factors listed above but is also affected by the geometry and diameter of the vessels [65]. This phenomenon is known as the Fåhraeus-Lindqvist effect where the viscosity decreases as the vessel diameter decreases. With decreasing vessel diameter, at the venules and arterioles level (10-300 μm), the apparent viscosity decreases to reach the minimum value of approximately 1.3 cP [2]. This decrease in viscosity is due to the cell free layer (CFL) near the vessel wall caused by the migration of the cells towards the center of the vessel [12, 13, 66–69]. This phenomenon is emphasized in microcirculation since the thickness of the CFL becomes comparable to the vessel diameter [12]. The smallest capillary diameter in which erythrocytes can flow with a maximum deformation is approximately 2.7 μm. At the capillaries level (4-10 μm), the apparent viscosity of blood increases rapidly. Microcirculation also exhibits a decrease of local hematocrit as the vessel diameter decreases within the range of vessel diameter of 10 to 300 μm, known as the Fåhraeus effect [2]. This decrease of local hematocrit is due to plasma skimming effects in microcirculation that is caused by the CFL formation, which greatly influences the Fåhraeus-Lindqvist effect [70, 71]. Therefore, in microcirculation, the local hematocrit does not exceed 20% [20]. At this microscale, blood is considered to be a two phase substance that is composed of a fluid and solid a phase [14] which behaves as a non-Newtonian fluid. Several non-Newtonian models have been developed for blood flow and blood aggregates.

1.4.6.1 Power law

One of the most known and used non-Newtonian models for blood is the Power law or Ostwald-de Waele Power law [72]. According to this model, the shear stress, τ, can be calculated as:

$$\tau = K\left(\frac{du}{dy}\right)^n \tag{1.6}$$

where K represents the fluid consistency index, n the non-Newtonian behaviour index, u the streamwise velocity of the fluid and y the coordinate normal to the vessel wall. When K increases, the viscosity of the fluid increases. When $n = 1$, the equation describes the behaviour of a Newtonian fluid having a constant viscosity and where the shear stress-shear rate relationship is linear. If $n < 1$, the resultant is a shear-thinning or pseudoplastic fluid where the viscosity decreases with increasing the shear rate. If $n > 1$, the resultant is a shear-thickening or dilatant fluid where the viscosity increases with increasing the shear rate. However, this model is not capable of predicting the behaviour and viscosity of fluids at very high or very low shear rates due to its limitation [73–75]. At low or high shear rate, the viscosity, estimated with the Power law model, tends to infinity rather than reaching a constant value as observed experimentally [66]. Despite this, this model is still widely used for its simplicity.

1.4.6.2 Bingham plastic model

The non-Newtonian Bingham plastic model describes the behaviour of a plastic or viscoplastic material that exhibits yield stress [73, 76]. A Bingham plastic is a viscoplastic material that behaves as a rigid body at low shear stresses but flows as a viscous fluid at high shear stresses [73]. Based on this model, the shear stress, τ, can be calculated as:

$$\tau = c\left(\frac{du}{dy}\right) + \tau_y \quad \text{if } \tau \geq \tau_y \tag{1.7}$$

$$\frac{du}{dy} = 0 \quad \text{if } \tau \leq \tau_y \tag{1.8}$$

where c represents the plastic viscosity and τ_y represents the yield stress of the material. The advantage of this model is the consideration of the yield stress in the equation. It was recently shown by Caton [77] that yield stress is present for high hematocrit and fibrinogen concentrations within the range of pathological conditions, which do not correspond to conditions in the microcirculation.

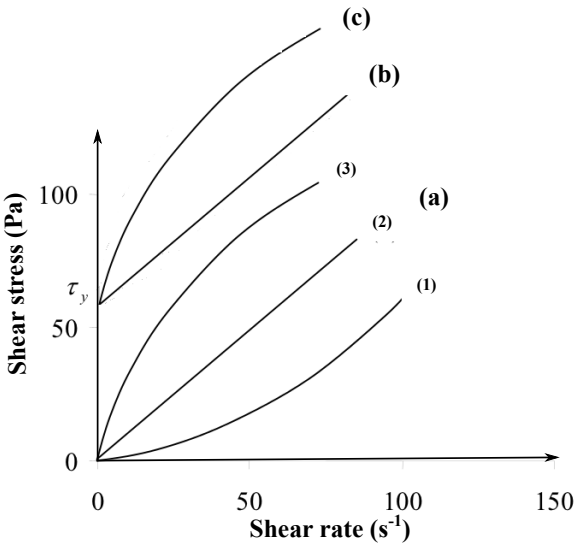

Figure 1.6: Illustration of shear stress in terms of shear rate for (a) the Power law model when (1) $n > 1$, (2) $n = 1$ and (3) $n < 1$, (b) the Bingham plastic model and (c) the Casson model [74]. τ_y represents the yield stress of blood.

1.4.6.3 Casson model

This non-Newtonian model, first introduced by Casson in 1959, is based on the behaviour of the liquid-solid interaction in a two phase flow [78]. The shear stress is expressed as:

$$\sqrt{\tau} = \sqrt{\tau_y} + \sqrt{k}\sqrt{\frac{du}{dy}} \quad \text{if } \tau \geq \tau_y \tag{1.9}$$

$$\frac{du}{dy} = 0 \quad \text{if } \tau \leq \tau_y \tag{1.10}$$

where k represents the Casson model constant. The advantage of this model is its ability to describe a non-Newtonian fluid exhibiting shear-thinning and yield stress simultaneously [79]. Therefore it can better describe the behaviour of blood. An illustration of the shear stress in terms of the shear rate for most of the models described is given in Fig. 1.6.

1.4.6.4 Carreau-Yasuda model

The Carreau-Yasuda model was first introduced by Pierre Carreau and further developed by Kenji Yasuda [80] where the apparent viscosity of the non-Newtonian fluid is given

by:

$$\mu_{app} = \mu_\infty + (\mu_0 - \mu_\infty)\left(1 + (\lambda\dot{\gamma})^a\right)^{\frac{n-1}{a}} \tag{1.11}$$

where $\dot{\gamma}$ represents the shear rate, μ_∞ the infinite shear viscosity, μ_0 the zero shear viscosity, λ the relaxation time, n the power law index and a the shape parameter. The Carreau model represents a special case of the Carreau-Yasuda model where $a = 2$. At high shear rates, the fluid thus behaves as a Newtonian fluid with a viscosity of μ_∞, whereas at low shear rates, the fluid acts as a Newtonian fluid with a viscosity of μ_0. The Carreau-Yasuda model is capable of predicting the shear-thinning behaviour of blood however the thixoropic (time-dependent) behaviour of blood is not taken into account.

1.4.6.5 Other models

Several other models mimicking blood behaviour exist such as the Walburn-Schneck model [81] that considers hematocrit, or the Hershel-Bulkley model which is a combination of the Bingham model and the Power law model [82]. Although it has been shown through experimental studies that these models can predict the behaviour of blood to some level of accuracy, none of these consider the RBC aggregates which greatly influence the micro-rheological behaviour of blood.

Bureau *et al.* presented a dynamical study of blood to investigate the rheological behaviour of blood in transient flow regimes at low shear rates [83]. Several experiments were performed to determine the stress variation in time when the system is subjected to an "échelon" of rectangular and triangular shear rates (hysteresis cycles). They discovered that, dynamically, blood exhibits a viscoelastic, shear-thinning and thixotropic behaviour simultaneously.

Owens [84] developed a new constitutive equation describing whole blood behaviour, based on the linear spring law and the multi-mode generalized Maxwell equation considering RBC aggregation (as a parameter) in the model. The model was compared to the Bureau *et al.* study [83] and showed similar results when subjected to an "échelon" of triangular shear rates.

The existing models described in this section, apart from those of Bureau *et al.* and Owens, do not take the dynamic factor into consideration in that blood samples are

studied over a period of time and thus, the instantaneous effect of aggregation on the viscosity of blood is not accounted for. Moreover, all of these models only consider the macroscopic behaviour of blood. To our knowledge, there is no model that provides enough information on the non-Newtonian behaviour of blood at the microscale.

1.4.7 Cell free layer

As mentioned in Section 1.4.6, the CFL, representing the cell depleted layer adjacent to the vessels wall, is formed as a consequence of the radial migration of the RBCs toward the vessel's centreline. The migration of these cells is primarily due to the tank-treading motion of the RBCs, where the cells orient and deform themselves in the direction of the flow and the membrane of the RBC appears to rotate around the inner core of the cell. RBC tank-treading is due to the compressible and tensile forces acting on the RBC membrane under shear [85]. Therefore, the cells that migrate toward the vessel's centreline are exposed to higher velocities and smaller shear rates than those initially at the vessel's wall. Hence, the migration of the RBC creates a cell depleted zone. The CFL is defined as the distance between the inner vessel wall and the outermost edge of the RBC core. The CFL plays an important role in microcirculation. In fact, it has been shown to reduce the shear stresses on the vessels wall since the cell depleted zone has a lower apparent viscosity. A larger CFL provides a larger reduction of the wall shear stress. However, an extensively large or small CFL might be indicative of pathological conditions. Modulating the wall shear stress causes a balance of the Nitric Oxide (NO) production by the endothelium, which is an important relaxation factor for the smooth muscle cells. Due to the formation of the CFL, a plasma skimming phenomenon is seen in microcirculation, reducing the hematocrit at these microscales [85]. Plasma skimming occurs when, due to bifurcations in microcirculation, only blood plasma flows in bifurcating vessels. Determining the CFL characteristics is of great importance to the hemodynamics field to better understand blood flow in the microcirculation under physiological and pathological conditions.

1.5 Summary

In Chapter 1, we presented the motivation behind this research and clearly presented the thesis statement and objectives. With this work we aim to:

- propose a new method to analyze blood behaviour in microcirculation by characterizing RBC aggregates at these microscales
- quantify RBC aggregates in microcirculation, dynamically, under controlled and constant shear rates
- provide quantitative results relating RBC aggregate size to the shear rate applied in a controlled microscopic environment
- obtain a relationship between the apparent blood viscosity and shear rate for low hematocrit within the microfluidic controlled system
- consequently reveal a relationship between RBC aggregate sizes and apparent blood viscosity simulatanously within the same microfluidic environment.

In this chapter, a broad introduction was also provided demonstrating the need to study and investigate RBC aggregation.

Chapter 2

Literature Review

In this chapter, we present a detailed description of previous relevant numerical and experimental studies on RBC aggregation, highlighting the gaps in the literature and the motivation of this work.

2.1 Numerical simulations

Numerical simulations present a useful tool to better investigate and understand RBC behaviour in microcirculation. Several Computational Fluid Dynamics (CFD) and other numerical models have been developed to mimic RBC aggregation observed in *in vitro* and *in vivo* experimental studies.

Numerous studies have investigated the motion of RBCs at the capillary level [86]. However, early models did not take into consideration the deformability and elasticity of the cell membrane that are major factors in RBC aggregation. The major considerations when modeling the behaviour of one or multiple RBCs flowing in vessels are the fluid-solid interaction between the RBCs and the suspending medium, and more importantly, the cell-cell interaction caused by the depletion of the molecules due to the osmotic gradient as postulated in the depletion mediated aggregation theory [40]. This factor combined with the deformability and elasticity of the cell membrane presents a significant challenge in the field of computational hemodynamics. Several methods have been developed to address this challenge.

Pozrikidis implemented a boundary-element method to simulate, in two dimensions, behaviour of a single RBC in simple shear flow, considering the RBC membrane stiffness [87]. This method is based on the boundary-integral formulation which provides an integral equation describing the localized velocity at a determined point as well as another integral equation describing the velocity on the cell membrane. The contour velocity integral equation is then solved engendering the membrane contour to travel in space by time integration [88]. For his study, Pozrikidis investigated the effect of the viscosity

ratio between the cell inner fluid and the medium, the effect of the initial inclination of the cell in the tube as well as the effect of the membrane bending stiffness. The author showed that a low viscosity ratio of up to 2 between the RBC inner fluid and the blood plasma resulted in a steady orientation of the RBCs in shear flow. However, increasing the viscosity ratio to physiological values results in a flipping motion of the RBCs in a shear flow causing a continuous periodic change of the RBCs' shape between their beconcave shape and "an inverse S shape" [87]. His observations agreed with previous experimental studies.

The Immersed Boundary Method (IBM) is the most extensively used method to numerically describe the behaviour of RBCs in microcirculation. It was first introduced and used by Peskin in 1977 [89] to study the flow in the cardiovascular system accounting for the fluid-solid interaction (blood-vessel). For this method, the medium (plasma) and the solid structure (RBCs) are treated as two separate interacting entities. The fluid domain is represented by uniform Eulerian grids, whereas the solid submerged structure is represented by a Lagrangian fibre network. The interaction between the fluid and the structure is accomplished by interpolating the velocities between the Eulerian and Lagrangian grids with a smoothed approximation of the Dirac delta function [90]. However, the IBM uses finite differences to solve for the structural domain. Eggleton and Popel combined the IBM with the finite element method allowing the submerged structure to be solved three-dimensionally and more accurately when subjected to very large deformations [91]. Bagchi extended the IBM to combine it with the finite element method to model and simulate a group of non-interacting RBCs flowing in vessels of 20 to 300 μm diameter [92]. The front tracking method was used to allow for a deformable interface [93]. The RBCs are not considered as rigid structures but modelled as liquid capsules (viscous liquid drops enveloped by a thin elastic membrane). The advantage of this method is its ability to simulate a large number of deformable RBCs flowing in a vessel [92]. However, these particles do not interact so aggregation cannot be studied with this method.

The lattice Boltzmann method (LBM) was first used by Sun and Munn to simulate two-dimensional (2D) RBCs, where the deformation of the cell was not considered [94]. In 2008, Sun and Munn extended their model to "examine the effect of one cell on

macroscopic blood rheology" accounting for cell-cell and cell-wall interaction to study the RBC-WBC forces. Rather than solving the Navier-Stokes (N-S) equations by the methods mentioned above, the LBM solves the discrete Boltzmann equation to simulate fluid flow with particle collision models such as the Bhatnagar-Gross-Krook (BGK) model [95].

The above overview provides pertinent information on RBC behaviour, especially in microcirculation. Several aspects, shown experimentally, have been validated numerically using these studies such as the Fåhraeus-Lindqvist and the Fåhraeus effects. However, these studies do not include RBC aggregation. In fact, the consideration of aggregation is a major challenge in the computational field due to the complexity and the lack of a precise definition of the existing mechanism (only theories exist). The numerical studies, in fact, aim to better understand the exact mechanism of RBC interaction and to better quantify the rouleaux. Bagchi *et al.* [14] adapted the IBM approach to incorporate cell-cell interaction, based on the Ligand-receptor binding model, in 2D, and to study a two-cell system behaviour in shear flow including the elasticity of the cell membrane. They focused on estimating the rate of bond breakage between the two cells when subjected to several ranges of shear rates and with different membrane elasticities.

Liu and Liu [12] used the Immersed Finite Element Method (IFEM) to provide a three-dimensional (3D) model of RBC aggregation, study its behaviour under several conditions (orientation and shear rate) and investigate its effect on blood rheology. In order to account for the RBC aggregation and deformation, the IFEM, which consists of a modified IBM, was coupled with a cell-cell interaction model and the Mooney-Rivlin strain energy function (for RBC deformation). This IFEM is, indeed, a combination of the IBM, the finite element method or the mesh-free Reproducing Kernel Particle Method (RKPM) for the solid structure to handle the large deformation of RBCs. The advantage of this specific mesh free method is its independence from the material to avoid any mesh distortion but also its ability to handle very large deformation since the connectivity among nodes is generated as part of the computation and can change with time [90]. Since the fluid-structure interaction is based on a smoothed approximation of the RKPM shape function, the higher order smoothness of the equation leads to a higher accuracy for the interaction. From their study, Liu and Liu were able to validate the

dependency of blood mechanical properties on the cell-cell interaction force, the shear rate, the cell deformability and the vessel geometry. They also investigated the adhesion energy and the hematocrit shear rate dependence.

Zhang *et al.* [13] combined the IBM (for the fluid-structure interaction) with the LBM (for the complex boundary conditions) using the Morse potential (for the cell-cell interaction). RBCs are modelled as deformable fluid capsules considering the RBC membrane elasticity (neo-Hookean viscoelastic material) and the cytoplasm viscosity. The advantage of this study is that it considers most of the major aspects influencing RBC aggregation for a more accurate study.

Iolov et al. [96] utilized the finite element method (FEM) to study blood flow in non-trivial geometries, such as an aneurysm, accounting for the contribution of the RBCs, based on the model developed by Owens [84]. The model accounts for the viscoelastic blood behaviour as well as the shear thinning and hysteresis effects. A comparison of Newtonian and non-Newtonian flows was conducted under the same conditions, where considerable differences in behaviour were found. The authors were able to provide a new computational method to study blood flow in a complex geometry.

Fenech *et al.* [15] proposed a two-dimensional particle model to investigate RBC aggregation and explore its effect on the rheological blood behaviour. The advantage of this model is that the molecular mass and the concentration of neutral polymers affecting aggregates can be mimicked so that a large group of interacting RBCs can be investigated. This study couples a particle model of RBCs with an aggregation and elasticity model. The authors based their study on the depletion mediated theory where the Morse potential model is used as the cell-cell interaction method. Several factors were investigated: among them, the effect of the aggregation force intensity as well as the aggregation kinetics and the shear rate dependence. These parameters were explored by estimating the Mean Aggregate Size (MAS) according to the aggregation rate. The observations from this study seem to agree with experimental *in vitro* studies performed under similar conditions.

Other particle based methods have been developed and used for blood flow simulations such as the Dissipative Particle Dynamic (DPD) method. This method originates from

the Molecular Dynamic (MD) method where each particle moves according to Newton's second law. The DPD is advantageous in that each particle in the simulation represents a collection of atoms or molecules rather than a single atom, reducing the computational costs. The DPD particles interact through pairwise soft potentials [97]. Fedosov et al. [97] describe a multiscale RBC model able to predict RBC mechanics, rheology and dynamics in accordance with experimental results. The RBC model is built by a series of points forming 2D triangulated surfaces on the RBC membrane. The triangular structures represent springs with a potential energy function accounting for the bending of the membrane and the area and volume conservation. In order to account for the viscous response of the membrane, a damper is added to each of the springs [98]. The biconcave shape is modelled using a volume reduction equation [99]. To reduce the computational costs, Pan et al. [100] present a Low-Dimensional RBC (LD-RBC) model based on the DPD method. The RBCs are now modelled as rings of 10 colloidal particles connected by wormlike chain (WLC) springs. Each particle represents a colloidal particle simulated with the DPD method, accounting for the bending rigidity of the RBC membrane by incorporating a bending force depending on the angle between two consecutive springs. This method was employed to investigate, among other effects, the CFL thickness and the plasma skimming effect in an asymmetric channel bifurcation at different hematocrit levels for healthy and diseased RBCs [101]. The observations from this study seem to agree with experimental *in vivo* studies performed under similar conditions.

Despite the development of these new approaches, the methods have only been applied to a small group of RBCs aggregating, which does not reflect the real *in vivo* behaviour of blood. Xu *et al.* [102] developed a mathematical model to simulate a large number of RBCs (45% H) by coupling the interaction between the fluid and the RBCs, taking into account the RBC deformation. The results from the mathematical model were compared to experimental studies under similar conditions and provided a very good agreement. However, due to the large experimental domain, the simulations do not reflect the behaviour of RBC in microcirculation.

Previous methods lack the capability of accounting for RBC aggregates and aggregates deformability in a microfluidic confinement. Further investigations are required in

this field in order to develop a numerical model capable of predicting RBC aggregation with realistic hematocrit and RBC deformability, especially in microcirculation.

2.2 Experiments *in vitro*

As discussed previously, due to the complexity of blood flow in microcirculation, several *in vitro* studies have focused on estimating RBC suspension and RBC velocities in microchannels to better understand and estimate blood behaviour in arterioles, venules and capillaries. Several methods have been used for velocity measurement including image analysis of high speed motion pictures [103], double slit photometry [104, 105], laser Doppler anemometry [106, 107] and particle imaging techniques. These methods are detailed in Section 2.2.1 [108–112].

The microchannels used for blood velocity measurements require specific properties to mimic the properties of vessels in the human body. Glass microchannels have been widely used for their optic properties (transparent material) and their well known fabrication procedure. However, due to rigidity and fabrication limitations, numerous recent studies have started to investigate the use of polymer based microchannels such as Polyethylene Terephthalate glycerol (PETG), in poly-di-methyl-siloxane (PDMS) and Poly(methyl methacrylate) (PMMA) [113, 114]. The properties and benefits of these microchannel materials are discussed in Section 2.2.2.

2.2.1 Velocity measurement methods

2.2.1.1 Image analysis of high speed motion pictures

In 1962, Bugliarello *et al.* [103] used an imaging technique to estimate the velocity of RBCs flowing in a tube. This technique consists of following the motion of individual cells between each frame by evaluating the distance travelled by the cell and dividing it by the time between these frames. The velocity profiles obtained in tubes of 40, 70 and 83 μm diameters with hematocrit up to 40% were found to be blunt but with a parabolic trend [105]. The simplicity of the method leads to several limitations.

The main disadvantage of this imaging technique is its time consuming frame correlation, since every frame requires analysis. Numerous other limitations including the

hematocrit (difficulty of detecting single cells), tube diameter (larger diameters increase the number of RBCs seen under the microscope which makes a single cell detection difficult) and the time between the frames (the smaller the rate of frames recorded, the more difficult it is to visualize a single cell due to RBC aggregation) lead to difficulties in velocity measurement. Because of these disadvantages, this technique is limited in accuracy but is simple to implement for estimating velocity of blood with RBC aggregation.

2.2.1.2 Double slit photometry

The double slit photometry method was introduced in 1967 by Wayland and Johnson [115]. It is based on the passage of RBCs in single file flow within two successive slits connected to two photomultipliers causing successive signal outputs (modulations) of the two photomultipliers. The time delay between the two modulations provides an estimation of RBC velocity. Although the method is efficient, it cannot be applied to larger vessels where RBCs do not flow in a single file flow due to the inconsistency of this flow. This method is used for *in vivo* experiments. In 1970, Gaehtgens *et al.* [104] extended this method to estimate the velocity of blood in vessels ranging from 25 μm to 130 μm in diameter. Although a velocity profile was obtained, several limitations of this method were revealed when applied to vessels larger than capillaries. Due to the large amount of RBCs in the channel, the difference in contrast between the cells and the suspension media was not sharp enough to provide a clear output of the photomultiplier, since the modulation of the system is based on the intracellular space between the cells. Also, the rotation and migration of RBCs in the larger channel diameters result in two different signal outputs preventing an exact estimation of the velocity profile in the tube [105]. Due to these limitations, RBC aggregation cannot be studied accurately with the double slit photometry method.

2.2.1.3 Micro particle image velocimetry (μPIV)

The most widely used method nowadays for blood and RBC velocity measurement is the μPIV method. This technique is a particle based flow visualization that is able to determine 2D velocity fields using the cross-correlation method. This μPIV method is, essentially, based on the same principles as the PIV method used for estimating velocities

at the macroscale. Several distinctions can be found between the extensively used PIV method at the macroscale and its application to microfluidics system.

PIV vs. μPIV The PIV method is well documented and has been used extensively for macro fluid flows [116, 117]. It usually requires an interline transfer camera to capture sets of double frames at very short interval times illuminated by a double-pulsed (dual cavity) laser. The time interval between the pair of images, dt, is usually on the order of hundreds to thousands of microseconds, chosen based on the volumetric flow rate, to allow the particles' displacement between the two frames to not exceed one quarter of the correlation window size [118]. The advantage of using an interline transfer camera over a normal camera (that is only able to capture single frames) is the accuracy of the results, since the cross-correlation method is used. Otherwise, the auto-correlation method would be used for the set of single frames, resulting in directional ambiguity of the velocity vectors. In fact, with the auto-correlation method, the particles within the field of view are illuminated multiple times within one recording. Therefore, the same frame is analyzed within a very small lapse of time, which may result in an incorrect estimation of the direction of the particles' displacement. For the cross-correlation method, the pulsed or continuous laser serving to illuminate the region of interest is synchronized with the interline transfer camera so that the set of two frames captured displays the particles flowing with the medium. These particles seeded within the flow fluoresce when exposed to a certain wavelength. The size of the particles for macro flow are, usually, on the order of 10 to 30 μm in diameter [119]. The set of double frames captured (usually, on the order of 100 frames), are post-processed using the appropriate software to be cross-correlated. For this purpose, the pairs of frames are discretized into small interrogation windows. The interrogation window size should be larger than the displacement of the particles in the flow in order to accurately measure the flow velocity. For each correlation window, a correlation map is plotted where the highest point represents the mean displacement of the particles within the correlation window. An illustration of the cross-correlation method is shown in Fig. 2.1

The theory behind the cross-correlation concept is explained by Raffel *et al.* [117], where the displacement using the cross correlation method is found as follows:

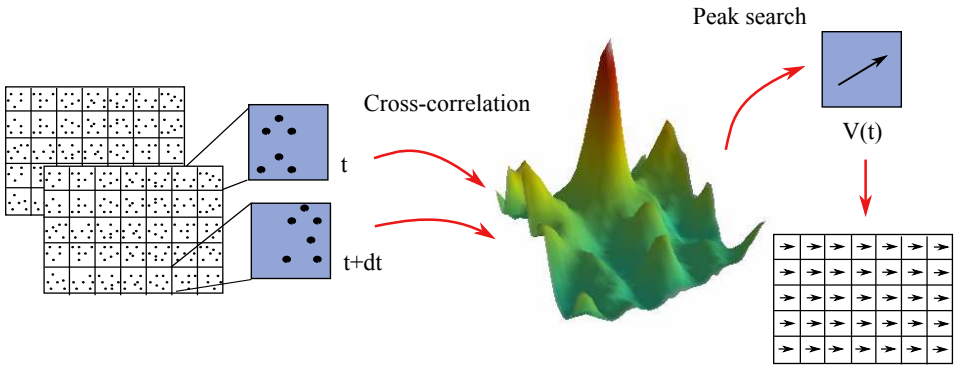

Figure 2.1: Illustration of the cross-correlation technique.

$$C(x,y) = \sum_{i=-L}^{L} \sum_{j=-M}^{M} I(i,j)I'(i+x, j+y) \tag{2.1}$$

where $C(x,y)$ represents the cross-correlation function, $I(x,y)$ and $I'(x,y)$ are the image intensity values of the two frames, L and M represent the size of the interrogation windows. When calculating $C(x,y)$ a cross-correlation plane is formed where the largest value represents the corresponding displacement of the particles in the window [120].

Although the system components and post-processing techniques are the same for standard PIV and μPIV, there are considerable differences between these two methods. For standard PIV, it is assumed that the seeded particles are homogeneously distributed within the flow and that they follow the flow perfectly, which is a reasonable assumption considering the particles' Stokes number. However, for micro flows, several parameters require further attention. As mentioned by Gui and Werely *et al.* [112], there are three main differences: first, the particles for microfluidics devices are on the order of 0.1 to 5 μm since the particles have to be small enough to not interfere with the flow. The problem is that the particles become too small compared to the wavelength of the laser. The solution is to label the particles so that they become fluorescent with the light source. Second, because of the small particle size, the Brownian motion, which is the random movement of the particles suspended in the medium, may have a great effect on the velocity values. However, the averaging of the set of frames captured by the camera drastically reduces this effect. Finally, the illumination technique differs for both methods. For standard PIV, the particles are illuminated via a laser sheet created by a

manipulation of the laser beam. However, for μPIV, a laser sheet cannot be created due to the restricted size of the domain, which can cause a diffraction of the laser beam. As a consequence, the volume illumination technique is required. This technique is mostly used with an optical system that has a depth of focus smaller than the flow depth. This method is explained in more detail by Meinhart *et al.* [111].

Due to the illumination method required for μPIV, two parameters play an important role toward the accuracy of the post processing: the Depth Of Field (DOF) and the Depth Of Correlation (DOC). The DOF represents a measure of the thickness of the focus plane of the microscope. Therefore, the DOF is directly related to the magnification lens, such that the DOF decreases with a higher lens magnification. This parameter plays an important role since the focus plane should be properly positioned in order to clearly visualize the particles in the microchannel mid-plane, where the velocity is expected to be the highest [121]. The DOC represents an estimate of the thickness of the measurement volume [121]. It is a measure that estimates the range of the out of focus particles that affect the image processing algorithm (cross-correlation). It can be expressed as follows [122]:

$$DOC = \frac{1}{2}\left[\left(\frac{1-\sqrt{\varepsilon}}{\sqrt{\varepsilon}}\right)\left(\frac{n^2}{NA^2}-1\right)\left({d_p}^2+\frac{1.49(M+1)^2\lambda_R^2}{M^2NA^2}\right)\right]^{0.5} \tag{2.2}$$

where ε is the fractional intensity of the particle on the object plane in comparison to a focused particle on the focal plane, (according to Meinhart *et al.* [111], this value can be set to 0.1, accounting for 10% of the intensity of an in-focus particle), n is the index of refraction of the immersion medium between the microfluidic device and the lens, λ_R is the wavelength of light (when fluorescent particles emit red light, $\lambda_R = 650\ nm$), d_p is the particle diameter, M is the magnification of the lens and NA is the numerical aperture of the lens. The DOC greatly depends on the particle diameter. Therefore, the choice of the tracer particles is crucial for the μPIV method.

Investigation of blood flows using μPIV Micro Particle Image Velocimetry (μPIV) was first introduced by Santiago *et al.* [109] in 1998 to study pressure driven micro flows. Since then, it was used by several researchers to determine the velocity of Newtonian flows, among them Kim *et al.* [110], where the mixing of two fluids with different refraction indices within a Y-channel configuration was studied. For their study, Newtonian

glycerol solutions with different mass fractions were used. Investigation of velocity profiles of RBC suspensions and RBC *in vitro* have been widely explored using the μPIV method. Since this method is a particle based technique, tracer particles (emitting at a prescribed wavelength) are required. These tracer particles can either be RBCs (dyed or not) flowing in the tube or fluorescent particles seeded in the suspension media. One of the first applications of μPIV to hemorheology was performed by Sugii *et al.* [123], in 2001. They were able to estimate the velocity of blood flow within a 100 μm diameter round glass tube. From this study, the velocities near the tube wall were found to be smaller than the theoretical velocities based on Poiseuille flow due to particle interaction with the walls.

Bitsch *et al.* [124] used μPIV to measure the velocity of "blood plug flow in a flat micro capillary" in order to determine the effect of the focal depth on the velocity. RBCs flowing in an aqueous solution are used as tracer particles. In their study, the velocity profile obtained with a RBC suspension was compared to a suspension of beads in water [124]. Pitts *et al.* [125] tested the "base clipping" method to investigate blood flows using μPIV in two different channel geometries. The "base clipping" method was compared to the overlapping method that was first introduced by Gui and Werely [126] for PIV applications and further extended by Nguyen *et al.* [127] for μPIV applications with a glycerol solution. The authors showed the influence of the channel geometry on the pre-processing and processing methods used.

Due to the complexity of blood flow in microcirculation, the RBC velocity does not directly reflect the bulk velocity of blood. In order to investigate the effect of the particles on blood velocity, Sugii *et al.* [128] separately studied the velocity of RBCs flowing in physiological saline and the velocity of the suspension media (also physiological saline for this test) flowing in a round glass tube of 100 μm diameter. RBCs, labelled with DiC_{16} (fluorescent dye), were used as tracer particles for the RBC velocity measurement while fluorescent particles were used as tracer particles for saline velocity measurement. The authors found the results of both experiments to be in agreement with the theoretical profile, although the profile obtained from the RBC velocity measurement showed a blunter velocity profile and slightly smaller magnitude than for the plasma. The authors attribute these differences to the non-Newtonian characteristics of the RBCs in plasma.

In 2006, Lima *et al.* [129] used the μPIV system to estimate the velocity of RBC suspended in physiological saline within a 100 μm glass square channel using red fluorescent solid polymer microspheres as tracer particles. The results were compared to tests with pure water flowing in the same channel. By combining conventional μPIV with a spinning confocal microscope, they were able to obtain a fully detailed three-dimensional velocity profile of a Newtonian and a non-Newtonian fluid in a square channel. Using their previous findings [129], Lima *et al.* [108] were able to study the effect of hematocrit on the 3D velocity profile of RBCs suspended in physiological saline in a 100 μm glass channel using the confocal μPIV technique. They found that hematocrit has an important effect on the shape of the velocity profile but also that the root mean square error values increases with hematocrit (up to 17%) due to the RBC motion and collision.

Several other techniques have been used to improve the μPIV measurements such as imaging techniques [124, 127], digital holography [130], stereo imaging [131] and other particle based techniques such as particle tracking velocimetry.

2.2.2 Microchannel material

The studies discussed in Section 2.2.1 use glass microchannels for *in vitro* blood velocity measurement. However, for *in vivo* comparisons, glass does not represent an ideal material to mimic vessel behaviour due primarily to its fabrication limitations [113]. In fact, glass microchannel fabrication is limited in depth and size because of the limited durability of the metal mask against the etchant (hydrofluoric acid), which limits the application of the microfluidic system. Also, the glass to glass bonding is difficult to accomplish due to the surface characteristics while the indirect bonding of the surface may block the channels with adhesive. Moreover, glass does not show the same physiological properties as blood vessels such as elasticity and the presence of living tissue [132]. Due to all these limitations, researchers have started investigating the possibility of using polymer based materials such as PMMA and PDMS. The most extensively used material for biomedical applications *in vitro* such as blood velocity measurements is PDMS. It is an optically transparent, non-toxic silicone based polymer. This material presents several advantages for biological applications: the material fabrication is inexpensive (mixing of silicone based elastomer and curing agent) and the material bonding to any surface can

be achieved easily since PDMS consists of polymer chains [133]. Another advantage is its permeability to cells but not to gases, as well as its flexibility and deformation based on the pressure drop in the channel, thus possibly mimicking the elasticity of blood vessels [134].

Lima *et al.* [132] used a 300 μm wide and 45 μm deep rectangular PDMS microchannel to estimate the 3D velocity profile of a RBC suspension in physiological saline (at 20% hematocrit) and compared this velocity profile to the one obtained for pure physiological saline using the confocal μPIV system. Both samples were seeded with fluorescent particles acting as tracer particles ($\sim$ 0.9 μm diameter). A blunt velocity profile was obtained experimentally and was well aligned with the theoretical profile for the same rectangular channel dimensions. Because of its unique properties, PDMS is widely incorporated in microfluidics devices not only for blood flow measurement but also for analytes (the presence of a substance) detection using immunoassays [135], for DNA and protein separation [136, 137] or sorting of cells [133, 138].

2.2.3 Aggregation investigation

Most of the studies discussed above do not consider aggregation effects. However, a few studies have attempted to study RBC aggregation, its effect on the velocity profile and determine the degree of aggregation in controlled flow conditions. Dusting et al. [9] investigated the effect of RBC aggregates on the μPIV velocity measurements in a shearing system. By observing the RBC aggregates under different shear rates (varying from 5.4 s^{-1} to 252 s^{-1}) and defining different aggregation indices, they showed that the velocity measurement depends on the degree of aggregation. This measure of aggregation was assessed based on the microscopic images corresponding to the visualized cell free surfaces, divided by the cell free surfaces obtained based on the hematocrit. A 2D correlation coefficient was determined and used to investigate the degree of aggregation on the accuracy of the velocity measurement. Kaliviotis *et al.* [8] investigated the spatial variation of blood viscosity in a shearing system. A constitutive equation was developed and coupled to shear rates determined from μPIV velocity measurements. The authors were able to show the spatial variation of the viscosity in the shearing system based on the degree of RBC aggregation, hence accounting for the time-dependent behaviour of

the aggregates. In another study [10], Sherwood *et al.* developed an analytical model to predict the distribution of hematocrit in a T-bifurcation channel. The empirical model was then compared to laboratory experiments for aggregating and non-aggregating blood suspensions. The distribution of the hematocrit was determined experimentally based on image processing techniques. The authors were able to obtain the hematocrit, the viscosity and the velocity distribution in a T-bifurcation channel.

These studies investigated RBC aggregates as well as the local viscosity of RBC suspensions for different hematocrit levels. However, the degree of aggregation was determined based on an aggregation index measured from the microscopic blood images. Chen *et al.* [11] presented a direct measurement technique for RBC aggregate sizes and provided RBC aggregate size distribution for different shear stresses by varying the flow rate of the suspensions while monitoring the pressure drop across a flow chamber. The shear stresses were calculated based on the monitored pressure using Stokes' equation. These previous studies were able to demonstrate a relationship between the RBC aggregates and the shear stress within the flow.

2.3 Experiments *in vivo*

Experimental studies of RBC aggregates *in vitro* detailed in Section 1.4.5 investigated the microscopic rheological properties of blood. However, the viscosity of blood, termed as the apparent viscosity, is dependent on several conditions and therefore behaves differently *in vivo*. Numerous studies have analyzed blood flow in living blood vessels. The concept of *in vivo* studies was introduced by Whittaker and Winton in 1933, who looked at the apparent viscosity in an isolated-perfused dog hind limb and compared their finding to their *in vitro* study of blood viscosity in a glass tube [139]. They reached the conclusion that a significant difference exists between the *in vitro* and *in vivo* results especially at high hematocrit, which encouraged researchers to investigate *in vivo* blood properties under several conditions [140–143]. Unfortunately, aggregation was not considered as an alteration factor of blood apparent viscosity in these studies. Cabel *et al.* [144] presented a study relating the flow resistance, depending on RBC aggregation, to the flow rate. Bishop *et al.* [145, 146] investigated the effect of RBC aggregates on the

velocity of the flow for different perfusion pressures, by controlling aggregate formation using Dextran 500. They demonstrated that, under slow flows [146], a blunted velocity profile is obtained which leads to a reduction in the perfusion pressure. Their findings agree with Cabel *et al.'s* observations thus providing confirmation of the dependence of the flow resistance on RBC aggregates. Bishop *et al.* [147] provided a measure of velocity profile as well as a curve-fit based on the linear least squares regression to estimate the parabolic nature of the velocity profile for aggregating and non-aggregating blood. They validated that, for non-aggregating blood, the velocity profiles are parabolic as expected for Newtonian fluids. However, when RBCs aggregate, the velocity profile is greatly affected, especially for slow flows engendering a blunt velocity profile. These studies used intravital microscopy, consisting of an inverted microscope with the appropriate illuminating system, a recording camera, an image analysis system (computer), pressure monitors and suitable perfusion equipment [45], in order to visualize the living venules. The RBCs are usually labelled to fluoresce under the appropriate illumination. Combining a high speed camera to the intravitral microscopy system, Bishop *et al.* were able to show that RBC aggregate sizes were inversely proportional to the shear rate applied [148].

These studies are of a great interest for understanding blood behaviour. However, even with the *in vivo* studies, no model has been developed to estimate the aggregation size according to flow condition (shear stress and shear rate applied), which demonstrates the importance of the current research.

2.4 Summary

In Chapter 2, we looked at studies investigating blood rheology and aggregation. Since Fåhraeus' observation of RBC aggregation in 1921, numerous studies have focused on understanding the mechanism behind these entities, which could lead to a better understanding of blood behaviour under pathological conditions. Non-Newtonian models have been developed with the intention of mimicking blood behaviour. However, these models were only developed to study blood at the macroscale and therefore did not fully consider the effect of aggregation in the microcirculation. Other studies have focused on measuring these aggregates *in vitro* and *in vivo* in order to relate the size of these

aggregates to cases seen under pathological conditions. These studies were only able to provide some aspects of RBC aggregation, which are not sufficient to describe the behaviour of RBC aggregation at the microscale. Numerical studies also attempted to model RBC behaviour and aggregation by considering RBC deformation of a single or a few RBCs. However, due to numerical limitations, the methods developed cannot model blood behaviour considering the RBC aggregation under physiological conditions. Therefore, a controlled system for RBC aggregation size estimation is required to determine the relationship between the aggregate size and the controlled flow conditions. The subsequent findings can be implemented in the previously mentioned models to improve the understanding of blood behaviour in microcirculation by accounting for the RBC aggregation at the microscales.

Chapter 3

Methodology

This chapter presents the methodologies and materials used experimentally and numerically to investigate and characterize RBC aggregates in a controlled microfluidic environment.

3.1 Experimental work

The experimental set-up, shown in Fig. 3.1, consists of a μPIV system (LaVision's MITAS) coupled with a high speed camera (Graftek Imaging, Inc., Austin, TX, USA) controlled using LabVIEW software (National Instruments, USA), and a temperature control system controlled using Arduino software (Arduino, USA). The μPIV system comprises a Charged-Coupled Device (CCD) Imager Intense camera (LaVision GmbH, Germany), a New Wave Solo-II Nd:YAG laser (New Wave Research, USA) emitting a wavelength of $\lambda_{emission} = 532\ nm$ and a MITAS inverted microscope (LaVision GmbH, Germany) with 20X lens magnifications. The 20X objective lens provides a numerical aperture of 0.4 and a depth of field of 4 μm. In order to control the position of the microchannel, the μPIV set-up includes a moving stage (xyz directions) with a minimum step size of 1 μm controlled by Davis Imaging Software (LaVision GmbH, Germany). Tracer particles, required for velocity calculations, diluted at 1% in water ($d_p = 0.79$ μm, $\lambda_{abs} = 542\ nm$ and $\lambda_{emission} = 612\ nm$) are introduced within the fluids, which illuminate when exposed to the appropriate wavelength. The fluids, contained in 25 and 100 μL glass syringes (Hamilton, USA), are inserted into a PDMS microchannel (110 μm in width and 60 μm in depth) at different flow rates using a pressure driven pump (Nexus3000, Chemyx Inc., USA).

Using the described system, the blood flow is directly observed in the shearing system normal to the velocity variation hence providing a different angle for the flow investigation compared to the previous studies, where the visualization of the aggregates was done in the direction of the velocity variation. The laser beam, synchronized with the exposure

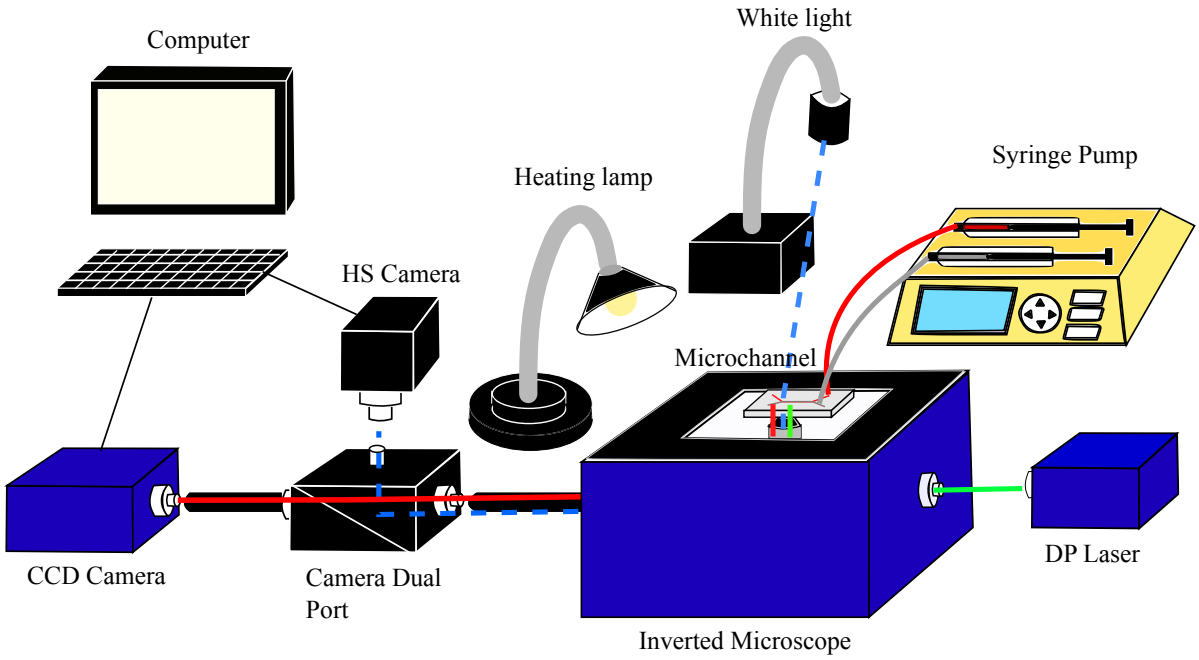

Figure 3.1: Experimental set-up and light path within the system.

time of the interline transfer camera, first encounters a filter to allow only for a certain range of wavelengths. The filtered laser beam encounters a dichroic mirror to be reflected and directed towards the objective lens. Consequently, the excited particles emit a light that passes through the emitter in the filter cube and is then imaged by the CCD camera. In order to control the measurement acquired, a camera dual port (two-camera mount) is used to dictate the light path to the different cameras. When the high speed camera is employed, white light is used for visualization. The CCD camera used is able to record 100 pairs of images with a rate of 5 Hz, in order to average the velocity data obtained. The methodology used for velocity calculations is detailed in Section 3.1.3. The spatial resolution of the camera is 10×10 μm^2 per pixel with 0.27 $\frac{\mu m}{pixel}$ when using the 20X lens magnification. The LaVision's Imager Intense camera was chosen for its high sensitivity and very low read out noise ($< 5e^-$) [149].

The high speed camera used is able to record several frames at different rates with high resolution. However, as for most high speed cameras, higher frame rates can be obtained when using smaller fields of view. For the maximum field of view allowed by the camera (resolution of 5.5×5.5 μm^2 per pixel allowing a 0.23 $\frac{\mu m}{pixel}$ conversion using the 20X lens magnification), the highest frame rate possible is 340 $\frac{frames}{s}$, which

is sufficient for the ranges of flow rates used within the microchannels ($Q = 5$ to 35 $\frac{\mu L}{hr}$). The frame capture is controlled via a program developed in LabVIEW, where parameters such as the exposure time of the camera, the frame rate and the field of view can be varied. Therefore, for each case, the highest image quality can be obtained with proper post-processing.

Throughout the experiment, the temperature of the blood sample is monitored and controlled at 37°C using a custom-made temperature control system to ensure and maintain a constant temperature [150]. The temperature control system includes a heating lamp as the heating source, a dimmer circuit to modify the lamp temperature, a thermocouple (Adafruit, USA) as a feedback sensor and a microcontroller (Adafruit, USA) to control the temperature sensed by the thermocouple. The system is capable of providing the temperature of the fluid every 2 seconds. To provide an effective temperature reading without disturbing the fluid flow, the thermocouple is positioned at the outlet port of the microchannel ensuring no contact with the microchannel walls.

3.1.1 Microchannel fabrication

The fabrication process of the microchannels follows standard photolithography methods. For this study, different microchannel configurations were designed using a Computer-Aided-Design (CAD) software (Draftsight) to be printed on transparency photo-masks as shown in Fig. 3.2. These masks are crucial since they dictate the light path during the fabrication process. In order to fabricate the mold for the microchannels, the following procedure is used:

- SU-8-50 epoxy-based negative photo-resist (MicroChem Corp.,USA) is spun on a silicon wafer at the appropriate speed to obtain the desired microchannel depth according to the manufacturer's instructions [151].

- The photo-resist is then heated to evaporate the solvents and densify the film. This step is known as soft bake.

- Using a mask aligner, the photo-mask is placed and held on top of the photo-resist film to be exposed to UV-light. A UV lamp, delivering 20 $\frac{mW}{cm^2}$, is used for this purpose. Therefore, only the transparent areas of the photo-mask (the microchannel

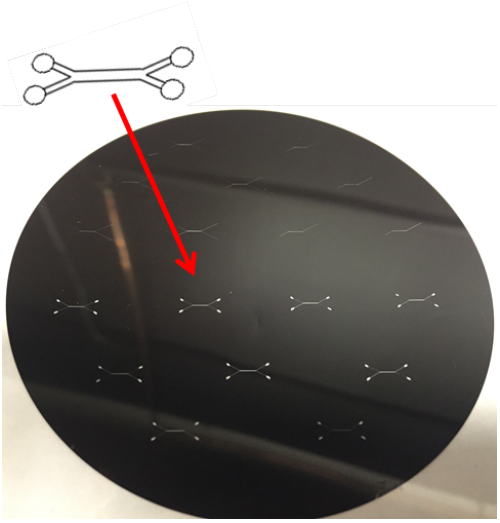

Figure 3.2: Transparency photo-mask including microchannel configuration.

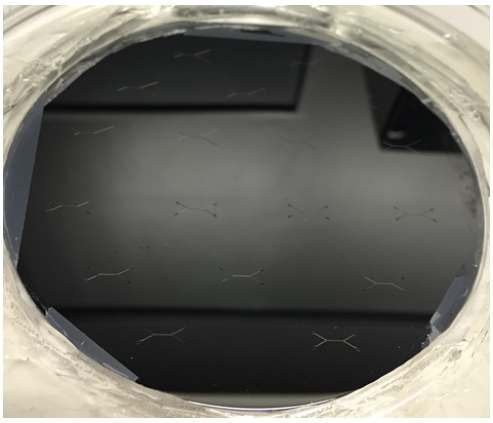

Figure 3.3: Fabricated mold for the microchannels.

configuration) will be exposed causing the polymerization of the polymer chains hence hardening the photo-resist in those specific areas.

- The wafer is then heated to selectively cross-link the polymerized chains. This step is known as post-exposure bake.

- Finally, the silicon wafer is immersed into a developer (SU-8-50, MicroChem, USA) to remove the excess of photo-resist.

The fabricated mold is shown in Fig. 3.3. Poly-di-methyl-siloxane (PDMS), made of a mixture of silicon elastomer base and a curing agent (Sylgard 184, Dow Corning, USA) with a ratio of 10:1, is then poured into the mold to create the microchannel as

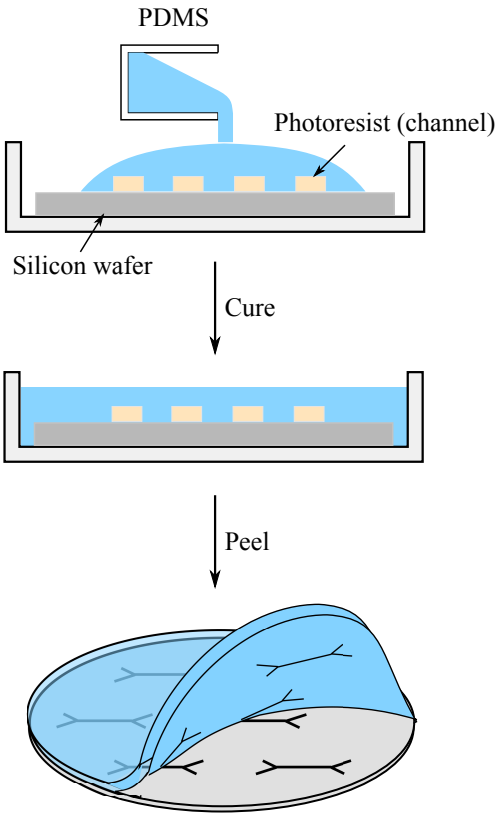

Figure 3.4: Microchannel fabrication process using PDMS.

shown in Fig. 3.4. The ratio of the mixture dictates the mechanical properties of the PDMS. Temperature and curing time are also important factors that alter the mechanical properties of the PDMS. To maintain a flexible membrane, the PDMS was heated for 90 minutes at $65°C$. Although, in these experiments, the physiological flow rates used only engender low pressure drops and hence do not cause significant deformation of the PDMS channel walls. The PDMS is cut into single channels and punched (using a puncher of 1.5 mm) to allow for the channel entries and exits. The punched channels are then bonded to a glass microscope slide using oxygen plasma treatment, performed with the PE-50 series plasma system (Plasma Etch, USA). When the surfaces to be bonded are exposed to oxygen plasma, the uppermost atomic layer of the polymer is oxidized to increase the bond strength. The oxidized surfaces present silanol groups (-OH) that are believed to form strong covalent siloxane bonds (Si-O-Si) when they are brought together [152, 153]. The advantage of using this method is the non-reversible bonding created that comes with clean surfaces to avoid blockage of the channel. However, the clean surfaces engender a hydrophilic behaviour of the PDMS [137], which is not desired.

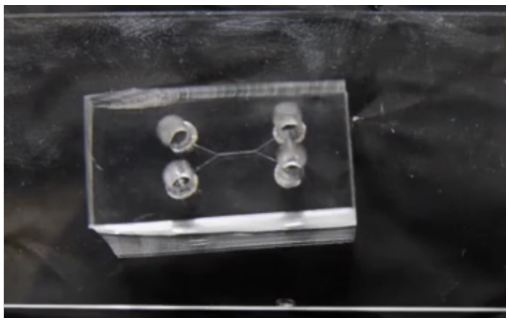

Figure 3.5: Double Y-microchannel configuration with merging and bifurcating channels. The width and depth of the main branch are 110 and 60μm respectively.

This hydrophilic behaviour is, however, reversible in time. In order to minimize the hydrophilic effect, the microchannels are used one week after the bonding process. The microchannel geometry used for this study is shown in Fig. 3.5.

3.1.2 Fluids

Phosphate Buffered Saline (7.4 pH) was used to entrain the blood layer in the microchannel as it maintains the equilibrium concentration with the blood suspension. It is crucial for the concentration to remain in equilibrium to avoid migration of ions in or out or the RBCs causing them to inflate and rupture (hemolysis) or to shrink (crenation). As a preliminary test, porcine blood was used to test the experimental set-up and investigate the RBC aggregate sizes. Ultimately, different human blood samples collected from healthy volunteers were used.

Blood samples preparation

Fresh and healthy porcine blood was collected from an accredited slaughterhouse with the authorization of the Ontario Ministry of Agriculture, Food and Rural Affairs. The blood collected was treated with 4 $\frac{g}{L}$ of ethylenediaminetetraacetic acid (EDTA) as an anticoagulant. Human blood was collected from healthy individuals with the approval of the ethics committee of the University of Ottawa (H11-13-06). The blood was collected in 4 mL tubes coated with EDTA. The blood preparation was similar for both porcine and human blood. All samples (whole blood) were centrifuged three times, following standard procedures, at 3000 rpm for 10 min in order to separate the RBCs from WBCs, platelets

and plasma. Blood plasma was collected only from the first centrifugation to ensure minimum contamination with white blood cells and platelets. The plasma was then filtered using a 0.2 μm plasma filter (Nylon, Non-Sterile, Fisher Scientific, Ireland) to remove any excess of white blood cells and platelets without interfering with the plasma proteins. Removing these constituents for experiments facilitates the use of μPIV, increases the quality of image processing and prevents blood clot formation. The RBCs of each sample were then suspended in their original plasma at three hematocrits (5%, 10%, and 15%) to visualize and determine the effect of the hematocrit on the aggregate sizes. To verify the hematocrit of each suspension, capillary tubes filled with the blood suspensions were centrifuged in microcentrifuge (CritSpin, Thermo Fisher Scientific, China) to determine the volume of the separated RBCs in the tube. Fluorescent tracer particles, used for velocity measurements, were added with a volume of 0.06% particles in 1 ml of each of the RBC suspensions and the PBS (6% of the particle solution). The experiments were performed within 8 hours after blood collection.

3.1.3 Velocity measurements

Velocities were measured with the μPIV method. This technique is a particle based flow visualization that is able to determine instantaneous 2D velocity fields using the cross-correlation method at the microscale level.

The methodology used for the velocity field measurements was previously validated to study blood flows. In a previous study (Pitts *et al.* [125]), we investigated several μPIV processing methods varying the window size, window shape and the percentage of overlapping of the correlation windows, on two microchannel geometries. The results were then compared to pre-processing methods to be cross-correlated. These pre-processing methods include the "base clipping" method introduced by Bitsch *et al.* [124] tested on blood, which consists of screening the pictures obtained with the interline transfer camera and removing the intensities of the out of focus particles that are lower than those of the in focus particles [125]. The second pre-processing method, first introduced by Wereley *et al.* [126] for PIV applications, was further applied to μPIV by Nguyen *et al.* [127]. This method consists of locating the maximum pixel intensities in all the double frames captured by the camera to only cross correlate the pair of pictures with the highest inten-

sities. This image overlapping technique greatly decreases the processing time since only two frames are correlated. It was found that, for two different channel configurations (straight and Y-microchannel), using a correlation window of 32×32 pixels, with 87% overlapping and the oval window shape weighted with a ratio of 4 to 1 in the x-direction, a smoother velocity profile was obtained and it matched the theoretical profiles. Comparing the best case with no-processing to the "base clipping" pre-processing method, the image overlapping pre-processing method and the simulation results, it was found that the velocity profile was smoother for the case where no pre-processing method was applied. The results showed a better accuracy with the straight channel [125] due to the complexity of the interface between the fluid layers in the Y-microchannel.

Based on this investigation, the velocity is determined using the cross-correlation method without pre-processing. A multi-pass approach is used for the velocity calculations within the correlation window, starting from a correlation window size of 64×64 decreasing to a window size of 32×32 with a 50% overlap for the different passes. The correlation windows are weighted in the x-direction with a ratio of 4:1 corresponding to the direction of the flow in the microchannel. The time between the laser pulses, dt, was varied from 2000 to 15000 μs based on the flow rate in the channel (varying from $Q = 35$ to 5 $\frac{\mu L}{hr}$, respectively) to obtain a 6 to 10 pixel displacement of the particles between two consecutive frames. The dt was optimized for the blood layer to obtain accurate shear rate measurements.

3.1.4 Shear rate mesurement

Figure 3.6 represents stacked μPIV images of the tracer particles with the highest intensities for the two-fluids flow in the double Y-microchannel. The blood layer is clearly delimited in this figure. The shear rates associated with each of the measurements are determined based on the velocity field obtained from the μPIV system as demonstrated in Fig. 3.7 (10% H, $Q = 20$ $\frac{\mu L}{hr}$). The velocity profiles are averaged in time (for 100 double frames) and extracted from Fig. 3.7 by averaging the velocity field in space (over the length of the visualization window).

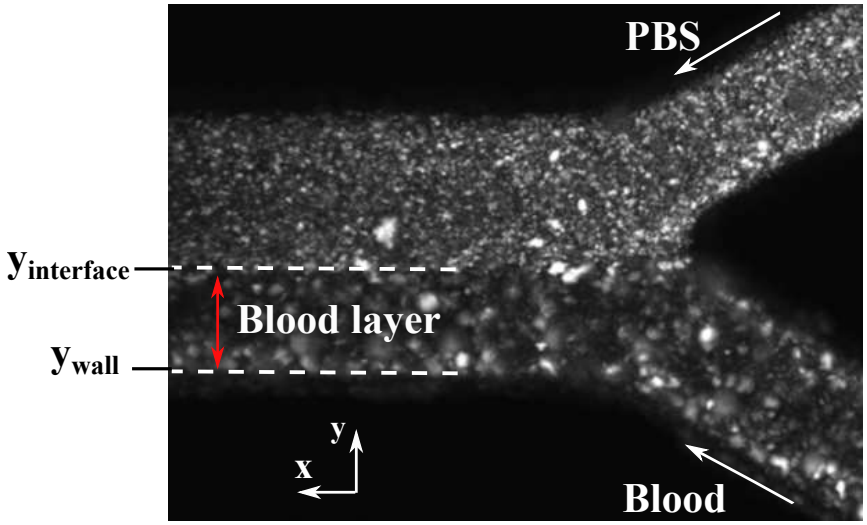

Figure 3.6: Stacked images of tracer particles with the highest intensities for RBCs and PBS in the double Y-microchannel.

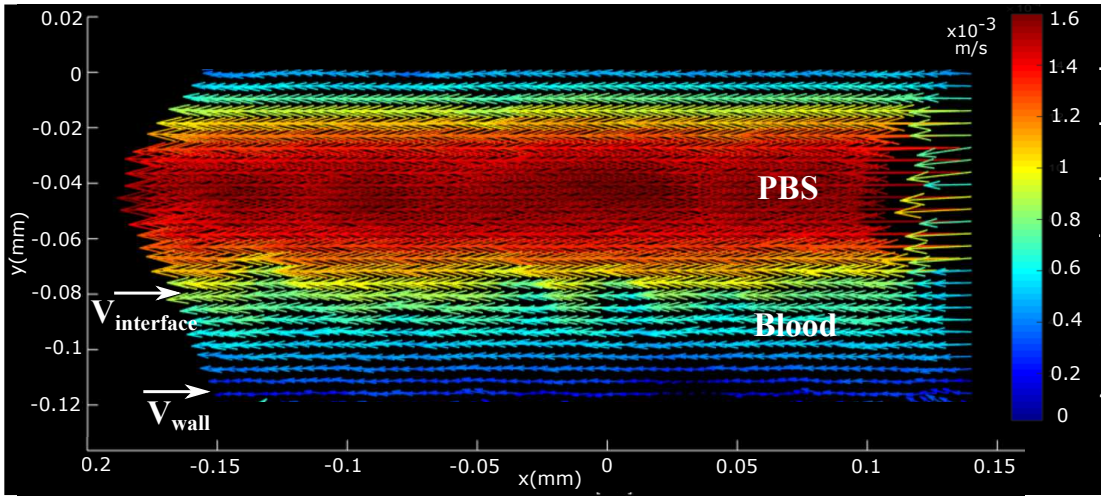

Figure 3.7: Velocity vector field obtained using the μPIV system for human RBCs suspended at 10% H flowing with $Q = 20\ \frac{\mu L}{hr}$.

The velocity profiles are shown in Figs. 3.8 (a) and 3.8 (b) for two different flow rates of 20 and 7.5 $\frac{\mu L}{hr}$ respectively. The shear rate is calculated as the slope of the linear velocity profile at the channel mid-plane within the blood layer as follows:

$$\dot{\gamma} = \frac{du}{dy} = \frac{V_{interface} - V_{wall}}{y_{interface} - y_{wall}} \tag{3.1}$$

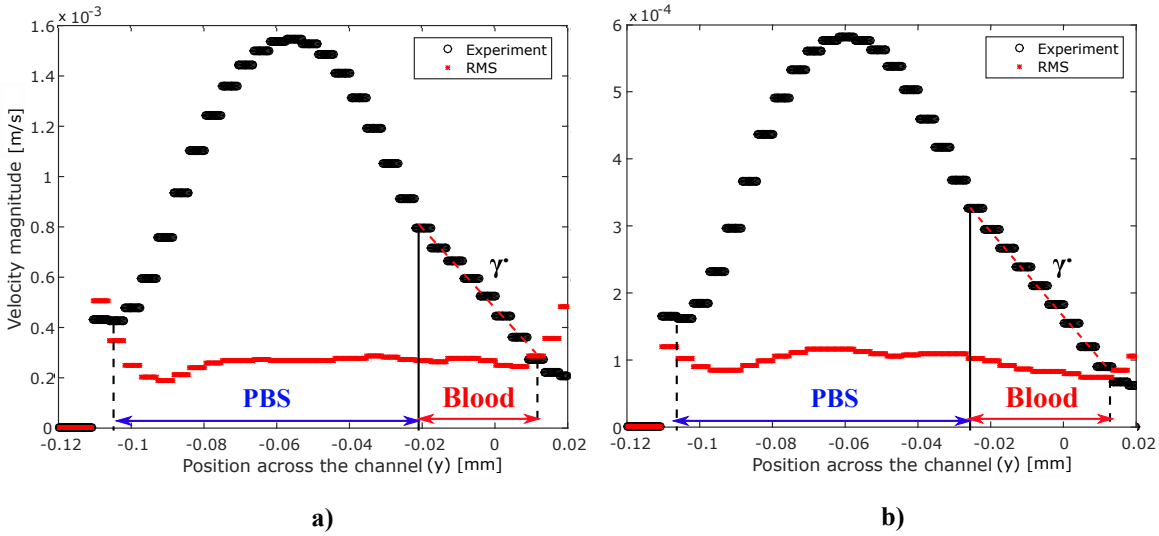

Figure 3.8: Velocity profile (black data points) averaged temporally and spatially and extracted from the vector fields for human RBCs suspended at 10% H flowing with (a) $Q = 20\ \frac{\mu L}{hr}$ and (b) $Q = 7.5\ \frac{\mu L}{hr}$. The red data points show the Root Mean Square (RMS) associated with the velocity measurements.

where $V_{interface}$ represents the velocity at the fluid interface, $y_{interface}$ the interface location, V_{wall} the velocity at the microchannel wall in contact with the blood and y_{wall} the position of the microchannel wall in contact with the blood. Here, $y_{interface} - y_{wall}$ represents the thickness of the blood layer that is measured from the microscopic images of the flow. The blood layer is delimited based on the visualization of the fluorescent tracer particle flow with the μPIV system as shown in Fig. 3.6.

3.1.5 Aggregate detection and image processing technique

For each test, the RBC aggregates flowing in the channel are recorded for 7 seconds, hence capturing 1200 frames. The length of the window captured is about 487 μm, allowing for visualization of multiple aggregates subjected to shear. The captured frames of each test are processed using a MATLAB program based on image pixel intensity. The flowchart of the program is shown in Fig. 3.9. Each image in Fig. 3.9 is of $1286 \times 300\ pixels$. Each original frame captured, $I_{original}$ (Fig. 3.9 (a)), is first filtered based on a median filter where each resultant pixel contains the median value of 15 by 15 neighbouring pixels. The filter is used to reduce the background noise of the image (resulting from possible impurities on the optic lens) and the effect of the non-uniform light distribution on the

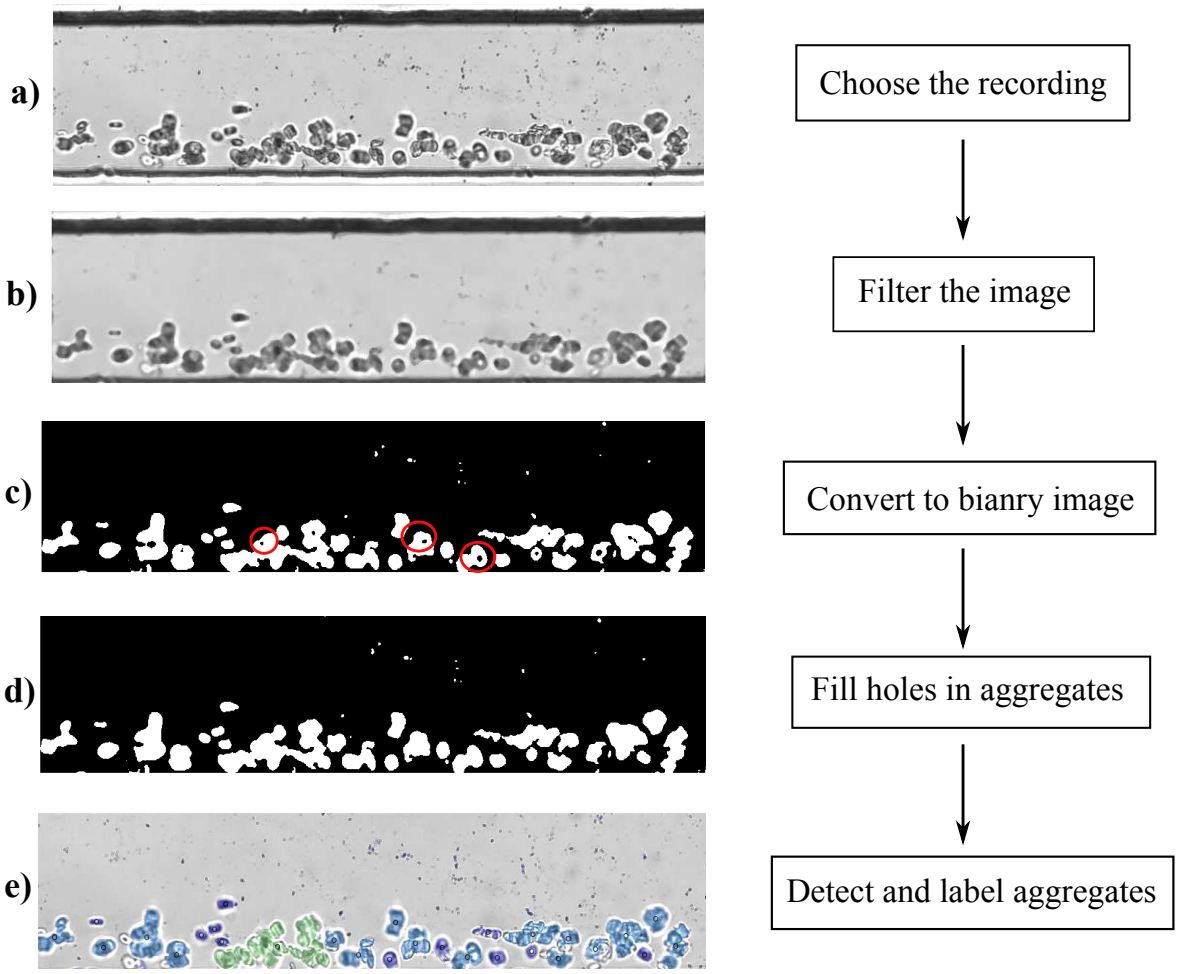

Figure 3.9: Flowchart of the MATLAB code for image processing of RBC aggregates flowing in microchannels. The red circles in the image show the incomplete aggregate detection due to the non-uniform light distribution in the image.

aggregates (Fig. 3.9 (b)). This filter was found to provide the best results compared to other median filter sizes, without altering the image quality. The filtered image, $I_{filtered}$, is then converted into a binary image where a function converts each pixel to black or white depending on the pixel intensity in the original grayscale image by assigning a specific threshold value for each recording as follows:

$$I_{binary}(x,y) = \begin{cases} 1 & \text{if } I_{filtered}(x,y) \geq Th \\ 0 & \text{otherwise} \end{cases}$$

where $I_{binary}(x, y)$ is the threshold function of $I_{filtered}(x, y)$ at a global threshold Th and pixel location (x, y). The global threshold, Th, was chosen for each different case based on the visual inspection of the aggregate detection. Due to non-uniform light distribution, converting the greyscale image into a binary image might result in an incomplete detection of the aggregates as shown in Fig. 3.9 (c). Therefore, if present (circled in red in Fig. 3.9 (c)), the holes are filled to consider the full aggregate (I_{fill} in Fig. 3.9 (d)). Connected pixels are then detected by determining neighbouring objects in the binary image. In this way, adjacent cells are associated to aggregates. The detected aggregates are then labelled and the image is converted into a red-green-blue (RGB) image for better visualization. The processed image is superimposed on the original frame in order to verify the efficiency of the image processing. The final image, I_{final}, is shown in Fig. 3.9 (e). The colour coding in the final image is based on the aggregate sizes detected in pixels and uses the "jet" colour map (range of three to seven colours). The two-dimensional areas of the aggregates are measured for each frame to obtain an average aggregate size per frame, which are in turn averaged for the entire recording to obtain a global average aggregate size per recording. The areas detected in pixels are then converted to μm^2 based on the conversion factor for the specific lens used. Using this method, it is also possible to determine the distribution of RBCs within the aggregates.
Validation and verification of the code were performed and are detailed in Section 4.2.

3.1.6 Viscosity measurements

The viscosity of the blood suspension is measured in the microchannel using the concept of optical viscometers [154–156]. This concept is based on the analytical solution of two co-flowing fluids in a rectangular cross-section that can be obtained by a Fourier series expansion. This method was first developed by Galambos and Forster [21] and was investigated in a T junction transparent device to determine the viscosity of a Newtonian fluid based on the known viscosity of a reference fluid. The reference fluid was mixed with a fluorescent dye that allowed for clearly detecting the fluid interface. High flow rates were used to minimize the diffusion between both miscible fluids. Later, Guillot *et al.* [23] extended the technique in a Y-shaped device to measure the viscosity of non-Newtonian fluids using immiscible fluids, avoiding the interdiffusion phenomenon at very low shear

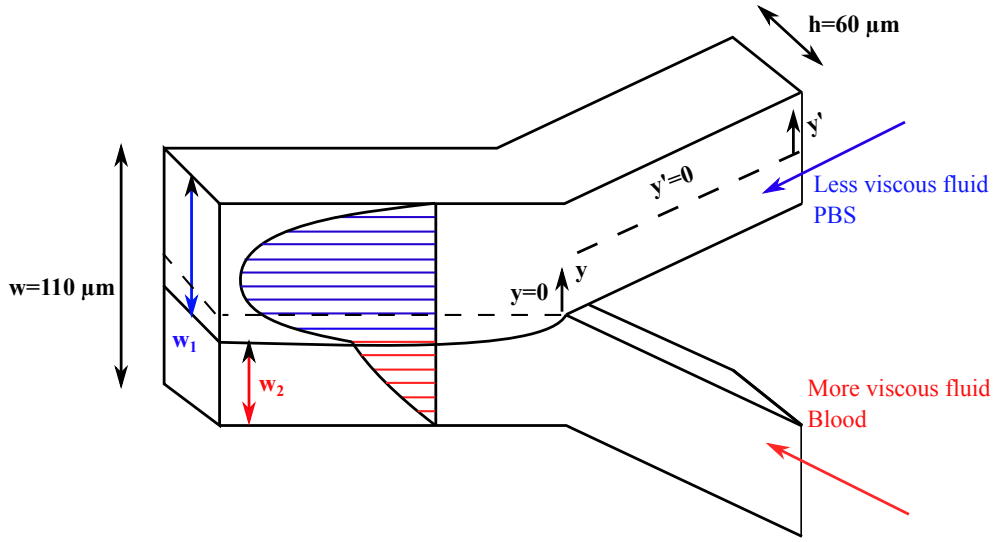

Figure 3.10: Blood entrained by Phosphate Buffered Saline (PBS) in a double Y-microchannel configuration.

rates. However, using immiscible fluids requires detailed knowledge of the interface shape which requires further extensive investigation. For this purpose, a fluorescent confocal microscope was used to map the three-dimensional shape of the interface. Solomon and Vanapalli [25] extended the technique further and designed a multiplexed viscometer allowing measurements of viscosity for up to eight samples simultaneously using miscible Newtonian and non-Newtonian fluids. In this study, the analytical solution of co-flowing streams in a rectangular channel was simplified to obtain two modes to measure the viscosity; the interface displacement (ID) mode and the interface compensation mode (IC). We used this technique to measure the blood viscosity in the double Y-microchannel with simultaneous measurements of shear rates and aggregate sizes.

For a rectangular channel of width w and depth h (Fig. 3.10) the analytical solution of two co-flowing laminar streams of incompressible fluids can be used to obtain the flow rate ratio as a function of the viscosity ratio as follows [25]:

$$\frac{Q_2}{Q_1} = \frac{\mu_1}{\mu_2}\left(\frac{0.5 + Y - \beta\sum_{n=1}^{\infty}\vartheta\left(\zeta - \kappa\xi\varphi\right)}{0.5 - Y - \beta\sum_{n=1}^{\infty}\vartheta\left(\alpha - \xi\chi\right)}\right) \tag{3.2}$$

where:

$$
\begin{aligned}
Y &= \frac{1}{2} - \frac{w_1}{w} \\
\vartheta &= 48\frac{(1-(-1)^n)}{\pi^5 n^5} \\
\zeta &= \frac{sinh\,(2\pi nY/2\beta)}{cosh\,(n\pi/2\beta)} + tanh\,(n\pi/2\beta) \\
\alpha &= \frac{sinh\,(2\pi nY/2\beta)}{cosh\,(n\pi/2\beta)} - tanh\,(n\pi/2\beta) \\
\kappa &= \frac{tanh\,(2\pi nY/2\beta)\,tanh\,(n\pi/2\beta) - 1}{tanh\,(2\pi nY/2\beta)\,tanh\,(n\pi/2\beta) + 1} \\
\varphi &= sinh\,(2\pi nY/2\beta)\,tanh\,(n\pi/2\beta) + cosh\,(2\pi nY/2\beta) - \frac{1}{cosh\,(n\pi/2\beta)} \\
\chi &= sinh\,(2\pi nY/2\beta)\,tanh\,(n\pi/2\beta) + cosh\,(2\pi nY/2\beta) + \frac{1}{cosh\,(n\pi/2\beta)} \\
\xi &= \frac{\left(\frac{\mu_2}{\mu_1} - 1\right)\left(\frac{1}{cosh(2\pi nY/2\beta)} - \frac{1}{(n\pi/2\beta)}\right)}{\left(\frac{\mu_2}{\mu_1} + \kappa\right)tanh\,(2\pi nY/2\beta) + \left(\kappa - \frac{\mu_2}{\mu_1}\right)tanh\,(n\pi/2\beta)}.
\end{aligned}
$$

Here μ_1 represents the viscosity of the reference fluid (PBS or water), μ_2 the viscosity of the test fluid (blood or POLYOX$^{\text{TM}}$), Q_1 the flow rate of the reference fluid, Q_2 the flow rate of the test fluid, w_1 the width of the reference fluid in the channel, w_2 the width of the test fluid in the channel, Y the dimensionless location of the interface and β the channel aspect ratio denoted as $\beta = \frac{h}{w}$. A detailed validation of the methodology will be presented in Section 4.3.

3.1.7 Numerical simulations

3.1.7.1 CFD code overview

The numerical simulations were conducted using the computational fluid dynamics research program *Nek5000* [157], based on the spectral element method [158]. This is a direct simulation solver for laminar, transitional and turbulent incompressible flows with heat transfer or transport phenomena [157] solving for the unsteady incompressible two-dimensional or three-dimensional Navier-Stokes governing equations:

$$\nabla.\mathbf{u} = 0 \tag{3.3}$$

$$\rho\left(\frac{\partial \mathbf{u}}{\partial t}+\mathbf{u}.\nabla\mathbf{u}\right)=-\nabla P+\nabla.\mu\left(\nabla\mathbf{u}+(\nabla\mathbf{u})^{T}\right)+\mathbf{f} \tag{3.4}$$

where the velocity, $\mathbf{u}=(u,v,w)$, and the pressure, P, are the solutions sought by the solver. $\mathbf{f}=f(x,y,z,t)$ represents a user defined forcing function. For constant viscosity μ, the second term of the viscous term is zero by the incompressibility condition, yielding what is known as the Laplacian formulation. However, for the majority of the simulations performed in this research, the stress formulation, consisting of considering the full stress tensor, is used. This formulation is more suitable for variable properties such as a two fluid flow or non-Newtonian fluids. If the flow includes heat transfer, the energy equation is also solved with forced or natural convection heat transfer:

$$\rho C_p\left(\frac{\partial T}{\partial t}+\mathbf{u}.\nabla T\right)=\nabla.k\nabla T+\mathbf{q} \tag{3.5}$$

where $\mathbf{q}=q(x,y,z,t)$ represents a user defined source term, T represents the temperature and C_p the constant heat capacity. In *Nek5000*, an option is provided to specify a passive scalar ϕ solved by essentially the same equation as for temperature:

$$\rho C_p\left(\frac{\partial \phi}{\partial t}+u.\nabla\phi\right)=\nabla.k_d\nabla\phi+\mathbf{q} \tag{3.6}$$

where k_d represents the diffusivity of that passive scalar. The Spectral Element Method (SEM), first introduced by Patera [158], combines the high accuracy of the Spectral Method and the geometric flexibility of the Finite Element Method [159]. For this method, the continuous domain is discretized into elements. Within each element the solution is approximated using tensor products of Nth order Legendre polynomial Lagrangian interpolants. For the velocity, the allocation of points in each element is based on Gauss-Lobatto-Legendre (GLL) quadrature points, whereas for the pressure space, the allocation of points is based on Gauss-Legendre (GL) quadrature points, as described by Maday and Patera [160]: this reflects a choice of the P_N-P_{N-2} formulation within the code, where the velocity is solved in the space P_N of the N^{th} order Legendre polynomials, while pressure is solved in the space P_{N-2} of order $N-2$ polynomials to satisfy the Ladyzenskaya-Brezzi-Babuska condition [161]. This condition prevents the appearance of spurious pressure modes. For a 1D problem, the solution in each element is approximated as follows:

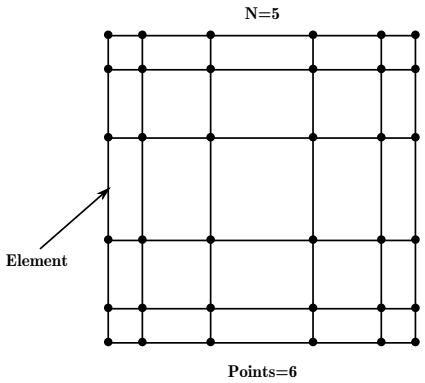

Figure 3.11: Example of a two-dimensional spectral element in the x-y plane with the highest order of polynomial $N = 5$ with 6×6 points.

$$q^{(E)}(r) = \sum_{n=0}^{N} q_n^{(E)} L_n(r) \tag{3.7}$$

where $q^{(E)}(r)$ represents the variable to be approximated, r is the local spatial coordinate of the element E, L_n represents the n^{th} order polynomial whereas N represents the highest order of polynomials. Therefore, the location of the quadrature points in each element is based on the choice of polynomials and more specifically, N, the order of the highest polynomial. Figure 3.11 represents an element with 6×6 points, where $N = 5$. The incompressible Navier-Stokes equations are thus solved with this method allowing for a variable viscosity [160]. The advantage of using this numerical method for smooth solutions such as incompressible Navier-Stokes equations is the rapid exponential convergence of the solution with the order of the Legendre polynomial N. The coarser the elemental grid, the higher the order of the Legendre polynomial can be, however, higher polynomial order requires longer computational time. A balance between the number of elements and the order of the polynomial yields a reasonably efficient solution scheme.

3.1.7.2 Grid generation

The geometry created experimentally is used to generate the grid used for the numerical study. Experimentally, the microchannel configuration was created using a CAD software to obtain the photo-mask required for fabrication and is shown in Figs. 3.12. For the numerical simulations, the two-dimensional geometry of the double Y-microchannel,

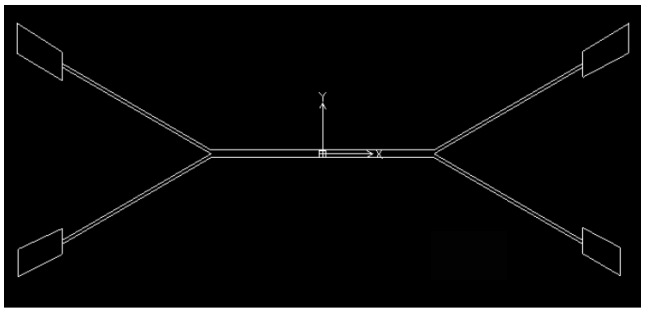

Figure 3.12: Microchannel configurations with merging and bifurcating channels (double Y-microchannel).

shown in Fig. 3.12, was created based on the prescribed points set in the Nekton grid generator, Prenek [157]. To create the three-dimensional mesh, the 2D domain is extended with a specific number of elements in the third direction. Further details on the grid are provided in Section 5.3.2.1.

3.1.7.3 Implementation of the numerical model

The experimental conditions were mimicked in the numerical model to verify the experimental results. For all the numerical tests performed, the $P_N - P_{N-2}$ formulation was used to satisfy the Ladyzenskaya-Brezzi-Babuska condition [161] eliminating the problem of spurious pressure modes. The variables were solved using the semi-implicit temporal scheme (implicit for diffusion and explicit for convection). The stress formulation was also used to allow for variable viscosity. Here, the viscosity is solved using a passive scalar advection diffusion equation, as described in Section 3.1.7.1 with Eq. (3.6), in order to be solved separately and then incorporated, for the next time step, into the solution procedure for the velocity and pressure. The numerical tests performed replicated the experiments performed in the double Y-microchannel with human blood suspended at 5 and 10% hematocrit for two different flow rates ($Q = 20\ \frac{\mu L}{hr}$ and $Q = 7.5\ \frac{\mu L}{hr}$). Since different PDMS chips were used during the experiments for the different hematocrits, the numerical domain was reconstructed for each case. Each grid consisted of 2260 and 1820 elements for the 5 and 10% H cases respectively. The order of the highest Legendre polynomial, N, for the double Y-microchannel configuration was set to be $N = 6$ and was shown to provide a smooth solution within each element. Several grids were employed

and refined until the flow was well resolved. It is especially important to adequately resolve the thin mixing layer arising from the joining of the two flows in the branches. Here, the PBS is treated and solved as a Newtonian fluid while blood is solved using empirical non-Newtonian models fitted from the experimental data presented in this work. The shear rate is calculated using the second invariant of the strain rate tensor as follows:

$$\dot{\gamma} = \sqrt{\frac{1}{2}\left(\dot{\gamma} : \dot{\gamma}\right)} = \sqrt{\frac{1}{2}\sum_{i}\sum_{j}\dot{\gamma_{ij}}\dot{\gamma_{ji}}} \tag{3.8}$$

where the strain rate tensor is calculated from the velocities using spectral operators on an elemental basis and is continuous across element faces. The shear rate solved for each step is used to determine the viscosity based on the empirical non-Newtonian model used. The non-Newtonian implementation in the code was first validated with the analytical solution of planar free jets, then further validated experimentally with a water soluble polyethylene oxide polymer with high molecular weight (POLYOX^{TM} WSR 301, Dow Corning, USA). The validation is detailed in Section 4.1. For the test cases, the Power law model is first tested and compared to the Carreau model [79]. The numerical findings are then compared to the experimental data.

Both fluids are assumed to be incompressible. All the channel walls present a no-slip boundary condition. At the outlet, a null pressure gradient normal to the boundary is prescribed. A three-dimensional parabolic velocity profile (Newtonian for the PBS branch and non-Newtonian for the blood branch) is prescribed as an inlet boundary condition. The velocity profile is prescribed based on the experimental three-dimensional flow rate in each branch.

Chapter 4

Methodology Validation

Methodologies used to achieve the work presented in this thesis require validation to ensure the veracity of the results obtained. This chapter focuses on the validation of the non-Newtonian capabilities of the CFD code, the image processing technique and the viscosity measurement technique.

4.1 Validation of the non-Newtonian capabilities of the Spectral Element code: POLYOX™ test

As mentioned in Section 3.1.7.3, the non-Newtonian capabilities of the Spectral Element code were investigated, further developed, and compared to the analytical solution of planar free jets using the Power law model [162]. To further validate the non-Newtonian capabilities of the code for blood simulations, numerical tests (using the Power law model) were conducted and compared to experiments performed with a water soluble polyethylene oxide polymer with high molecular weight (POLYOX™ WSR 301, Dow Corning, USA), proven to behave as a power law fluid [163]. The simulation and experiments were performed using the double Y-microchannel geometry.

4.1.1 Experiment

To test the power law fluid experimentally, POLYOX™ WSR 301 (Dow Corning, USA) in powder form was dissolved in deionized water at a ratio of 0.3%(wt). The ease and proper dissolution of the POLYOX™ WSR 301 greatly depend of the rate of addition (to avoid viscosity build up or particle clumping) and the type of stirring. Proper dissolution of the resin (POLYOX™) was performed according to the Dow Corning guideline for dissolving [164] using a magnetic stirrer. The viscosity of the mixture was measured using the microVISC-m^{TM} viscometer (Rheosense Inc., USA) prior to the experiment and is shown via a shear stress-shear rate diagram in Fig. 4.1 for different shear rates varying from 10 to 1000 s^{-1}. 6% in volume of the fluorescent tracer particle solution

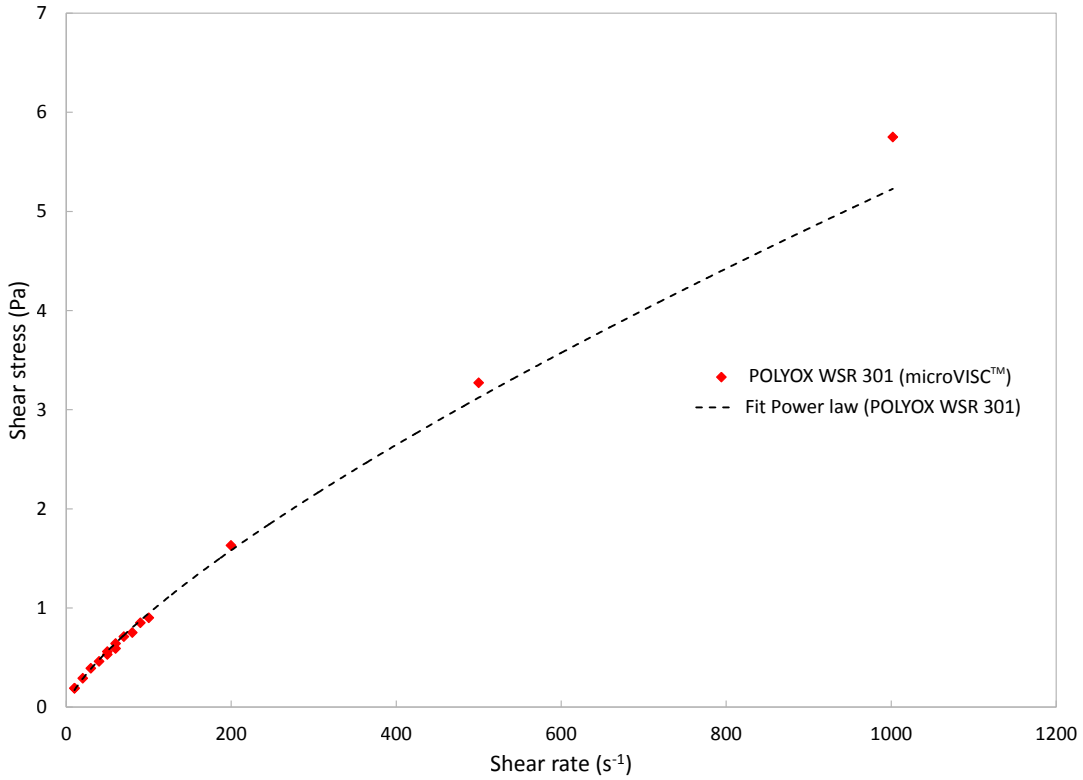

Figure 4.1: Shear stress-shear rate data measured using the microVISC-m^{TM} viscometer and fitted curve of the POLYOX$^{\text{TM}}$ WSR 301 0.3%(wt) solution.

was added to the polymer solution and to deionized water for μPIV measurements. The POLYOX$^{\text{TM}}$ WSR 301 0.3%(wt) solution was introduced in the double Y-microchannel via a 50 μL glass syringe (Hamilton, USA) and entrained with water (introduced via a second 50 μL glass syringe (Hamilton, USA)). Both fluids in the channel were set to flow with the same flow rate of 5 $\frac{\mu L}{hr}$ for each branch.

4.1.2 Simulation

In order to perform the simulations, the experimental viscosity data were used and fitted to a Power law model to find the power law parameters: the consistency index K and the power law index n (Fig. 4.1) as follows:

$$\mu_{app} = K\dot{\gamma}^{n-1} \tag{4.1}$$

where $K = 0.02519\ Pa.s$ and $n = 0.7859$. The coefficient of determination for the linear regression modeling of the Power law was found to be $R^2 = 0.9956$. The Power law parameters were used in the CFD code to reproduce the experiment: 2D and 3D simulations were performed. The velocity profiles of both fluids at their respective branch entries (inlet boundary conditions) were set as parabolic power law velocity profiles using the experimental flow rates as described in the following sections.

4.1.2.1 Implementation of inlet boundary conditions: theoretical behaviour of power law fluids

The inlet velocity boundary conditions for the numerical simulations were implemented based on the experimental flow rates calculated from the μPIV velocity data. The inlet boundary conditions for the viscosity were based on the experimental fits of the viscosity data. For the 2D simulations, a planar laminar flow of a power law fluid between infinite parallel plates separated by a width w_b in the direction perpendicular to the branch length, denoted by y' as shown in Fig. 3.10, was considered at the entry branches of the channel . The boundary conditions are presented based on the dimensions of the domain. The axial velocity profile is given by:

$$u(y') = \frac{1}{1+1/n}\left(\frac{dP}{dL}\frac{1}{K}\right)^{1/n}\left\{\left(\frac{w_b}{2}\right)^{1+1/n} - |y'|^{1+1/n}\right\} \tag{4.2}$$

where $\frac{dP}{dL}$ is the pressure drop along the microchannel. The volumetric flow rate is determined by integration between the plates across a unit depth as follows:

$$\begin{aligned} Q\left[\frac{L^3}{T}\right] &= 1\,[L]\,.\int_{-w_b/2}^{w_b/2}\left\{u(y')\left[\frac{L}{T}\right]\right\}dy'\,[L] \\ &= \frac{w_b}{2+1/n}\left(\frac{dP}{dL}\frac{1}{K}\right)^{1/n}\left(\frac{w_b}{2}\right)^{1+1/n}. \end{aligned} \tag{4.3}$$

Normalizing $u(y')$ by Q gives:

$$\frac{u(y')}{Q} = \frac{1}{w_b}\left(\frac{2+1/n}{1+1/n}\right)\left\{1 - \left(\frac{|y'|}{w_b/2}\right)^{1+1/n}\right\}. \tag{4.4}$$

The maximum velocity u_m is at $y' = 0$. Substituting for $y' = 0$, Eq. (4.4) becomes:

$$\frac{u_m}{Q} = \frac{1}{w_b}\left(\frac{2+1/n}{1+1/n}\right). \tag{4.5}$$

Eq. (4.5) can be used to find the maximum velocity based on the experimental flow rate. The velocity profile can therefore be expressed as:

$$u(y') = u_m\left(1 - \left(\frac{|y'|}{w_b/2}\right)^{1+1/n}\right). \tag{4.6}$$

For the 3D simulations, the velocity profile is extended in the z-direction as follows:

$$u(y')_{3D} = u_{3Dm}\left(1 - \left(\frac{|y'|}{w_b/2}\right)^{1+1/n}\right)\left(1 - \left(\frac{|z|}{h/2}\right)^{1+1/n}\right) \tag{4.7}$$

where h represents the depth of the channel in the z-direction and u_{3Dm} is:

$$u_{3Dm} = \frac{Q}{w_b h}\left(\frac{2+1/n}{1+1/n}\right)^2. \tag{4.8}$$

Flow rate calculations were obtained by extruding the 2D experimental velocity profile in the third dimension by a ratio of the experimental velocity profile to the theoretical Newtonian profile as demonstrated below. The theoretical profile was calculated using the analytical solution of a Newtonian fluid in a rectangular channel [165] as follows:

$$u(y', z) = \frac{4}{\mu w}\frac{dP}{dL}\left[\sum_{n=1}^{\infty}\frac{(-1)^{n+1}}{\varpi^3}\left(1 - \frac{cosh\,(\varpi z)}{cosh\left(\frac{\varpi h}{2}\right)}\right)cosh\,(\varpi y')\right] \tag{4.9}$$

where $\frac{dP}{dL}$ is the pressure drop, μ is the viscosity, h the depth of the channel in the z-direction, w_b is the channel width in the y'-direction and $\varpi = \frac{(2n-1)\pi}{w_b}$. The ratio of the experimental velocity profile $V(y')$ to the theoretical Newtonian profile at the mid-plane $u(y', z = 0)$ is then applied to a three-dimensional theoretical profile $u(y', z)$ (in Eq. (4.9)), resulting in a predicted three-dimensional experimental profile [125] as follows:

$$F(y', z) = u(y', z)\frac{V(y')}{u(y', z = 0)}. \tag{4.10}$$

Hence the experimental flow rate is found by:

$$Q_{exp} = \frac{1}{w_b \times h} \int_{-w_b/2}^{w_b/2} \int_{-h/2}^{h/2} F(y,z) dz dy'. \tag{4.11}$$

An example of the reconstructed experimental profiles is provided in Fig. 4.4 in Section 4.1.3.

4.1.2.2 Example of boundary conditions implementation: Geometry, units and similarity

The bottom (water) and top (POLYOX^{TM} WSR 301) branches of the experimental microchannel have respective widths of 48 μm and 58 μm and a constant depth of 60 μm. The merged channel has a width of 105 μm.

The simulation units for length, time and mass are written as $\mathbb{L}$, $\mathbb{T}$ and $\mathbb{M}$. The simulation length scale $\mathcal{L}$ is fixed based on the width of the bottom branch (water branch):

$$\mathcal{L} = \frac{1\mathbb{L}}{48\mu m}. \tag{4.12}$$

The simulation time scale $\mathcal{T}$ is specified as:

$$\mathcal{T} = 1\mathbb{T}s^{-1}. \tag{4.13}$$

The experimental density, ρ_{exp}, of the pure water and the dilute aqueous solution is taken as that of water at atmospheric pressure and 25^oC. By specifying a constant simulation density, ρ_{sim}, of $1\mathbb{M}\mathbb{L}^{-3}$, the scaling mass $\mathcal{M}$ can be found as follows:

$$\mathcal{M} = \left(\frac{\rho_{sim}}{\rho_{exp}}\right) \mathcal{L}^3 \tag{4.14}$$

Therefore, the similarity of experiment and simulation is ensured by applying these scaling factors to all remaining variables. Initial and boundary velocity profiles in 2D

are set as real multiples of the non-dimensional profile:

$$u_{sim}(y^*) = u_{m,sim}\left\{1 - |y^*|^{1+1/n}\right\} \tag{4.15}$$

$$= \frac{Q_{sim}}{A_{sim}}\left(\frac{2+1/n}{1+1/n}\right)\left\{1 - |y^*|^{1+1/n}\right\} \tag{4.16}$$

$$= Q_{exp}\left(\frac{\mathcal{L}^3}{\mathcal{T}}\right)\left(\frac{1}{A_{sim}}\right)\left(\frac{2+1/n}{1+1/n}\right)\left\{1 - |y^*|^{1+1/n}\right\} \tag{4.17}$$

where, y^* represents the dimensionless location in the y'-direction as $\frac{y'}{w_b/2}$, $A_{sim} = w_b \times h$ the dimensionless cross-sectional area of the branch, Q_{sim} the dimensionless flow rate in the simulation obtained by converting the experimental flow rate Q_{exp} using the length and time scales. Simulated viscosities (K and μ) are also converted from their experimental values:

$$K_{sim} = K_{exp}\left(\frac{\mathcal{M}}{\mathcal{L}\mathcal{T}}\right) \tag{4.18}$$

$$\mu_{sim} = \mu_{exp}\left(\frac{\mathcal{M}}{\mathcal{L}\mathcal{T}}\right). \tag{4.19}$$

4.1.3 Results

Figure 4.2 represents the stacked images of the highest intensity tracer particles illuminated by the laser beam during the μPIV experiment of water and POLYOX^{TM} WSR 301 0.3%(wt) flow in the Y-microchannel. The two distinctive fluid layers are clearly visualized. The velocity profiles are extracted at three different locations: 38 μm, 55 μm and 92 μm from the intersection as shown in Fig. 4.2 and are compared to the numerical velocity profiles at the same locations in Figs. 4.3 (a), 4.3 (b) and 4.3 (c), respectively. The 2D simulations do not represent the actual behaviour of the flow in the experiment. Therefore, 3D simulations were performed by extruding the domain used for the 2D simulations in the third dimension. The three-dimensional velocity profiles, reconstructed based on the two-dimensional experimental profile (Eq. (4.10)) were used for the 3D simulations and are shown in Fig. 4.4 for the three same locations: (a) 38 μm, (b) 55 μm and (c) 92 μm from the intersection. The experimental velocity distribution at the channel branches and in the merging area is shown in Fig. 4.5 (a) and

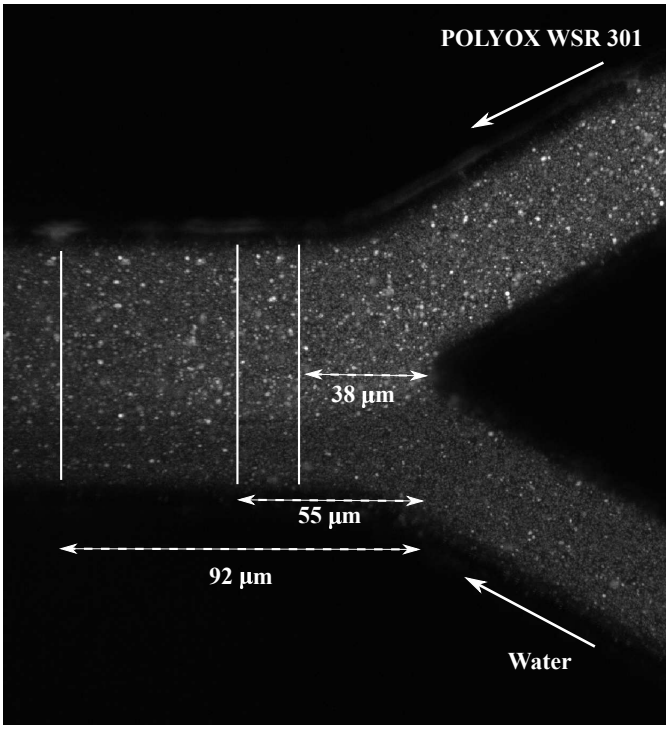

Figure 4.2: Stacked images of tracer particles with the highest intensities for the POLYOX^{TM} WSR 301 0.3%(wt) solution and water in the double Y-microchannel. The lines in the image indicate the different locations of the profile extraction: 38 μm, 55 μm and 92 μm from the intersection.

compared to the numerical velocity distribution at the same location in Fig. 4.5 (b). The similarity between the experiments and the simulations is clear. The velocity profiles are extracted at the same three locations, as above, near the intersection and are shown in Fig. 4.6. These 3D profile comparisons show marked improvement over the 2D ones in Fig. 4.3, illustrating the importance of calculating the 3D velocity profile for flow in confinement microchannel. It is important to note the similarities between the experimental and numerical velocity profiles especially within the POLYOX^{TM} WSR 301 layer. However, differences in velocity amplitude, up to 20%, were noted within the water layer. These differences might result from the selection of the time interval between the laser pulses and the cross-correlation method optimized for the POLYOX^{TM} WSR 301 layer as mentioned in Section 3.1.3. These similarities in the 3D velocity profiles confirm the proper implementation of the non-Newtonian fluid behaviour and validate the non-Newtonian capabilities of the CFD code (*Nek5000*) for a two fluid flow (Newtonian and non-Newtonian fluid) in a branched channel.

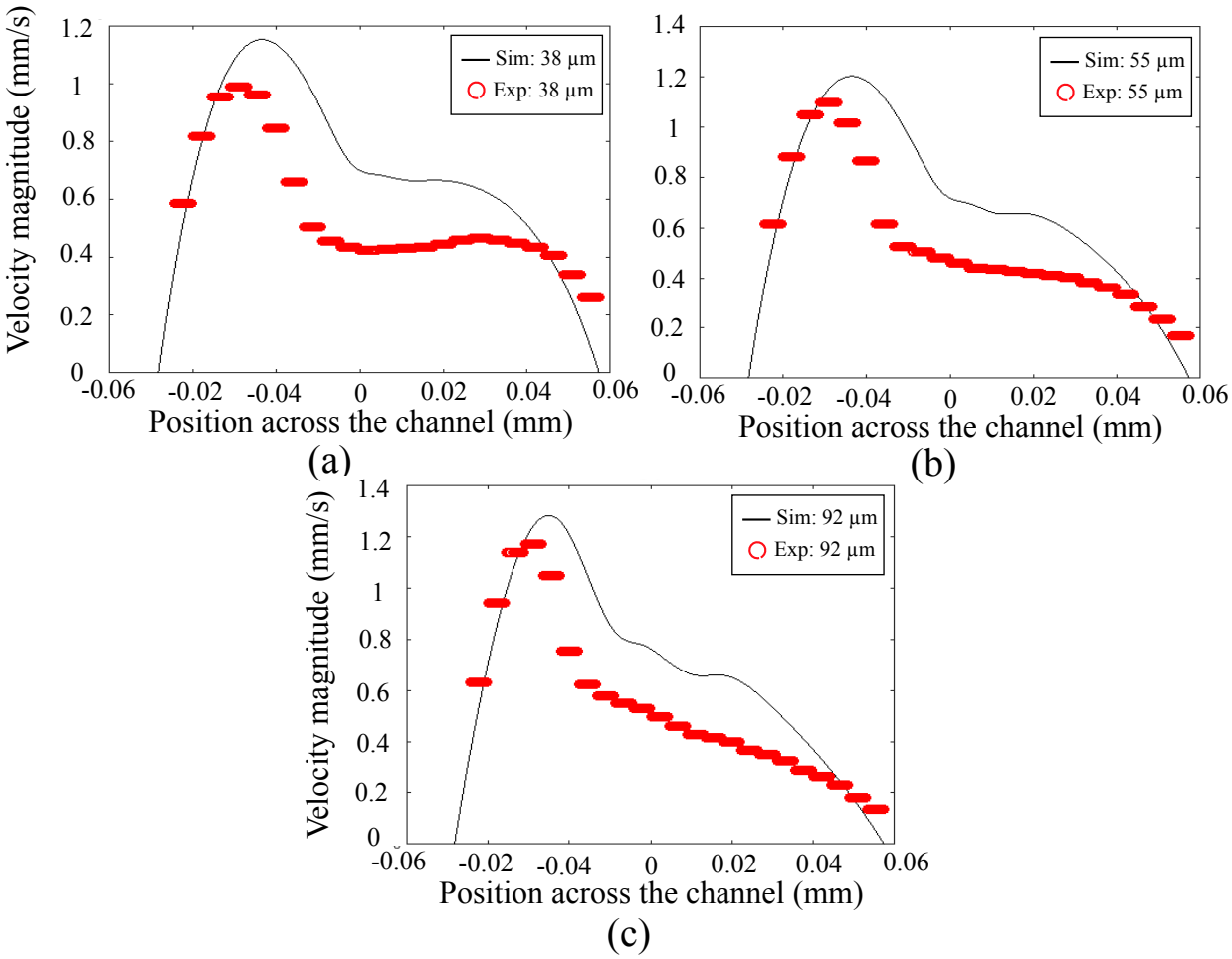

Figure 4.3: Simulated two-dimensional and experimental three-dimensional mid-plane velocity profiles of water and POLYOX^{TM} WSR 301 0.3%(wt) flow in the Y-microchannel for three different locations: (a) 38 μm, (b) 55 μm and (c) 92 μm from the intersection (refer to 4.2).

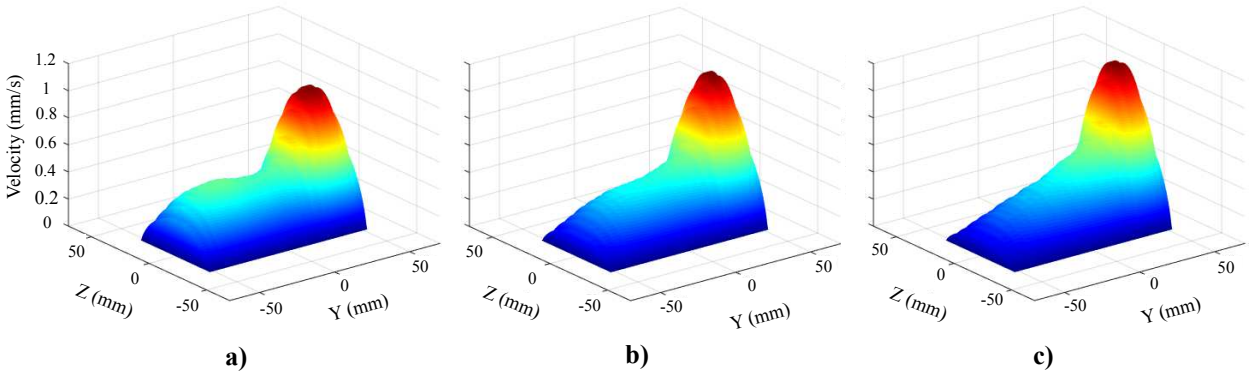

Figure 4.4: Reconstructed experimental three-dimensional velocity profiles of water and POLYOX^{TM} WSR 301 0.3%(wt) flow in the Y-microchannel for three different locations: (a) 38 μm, (b) 55 μm and (c) 92 μm from the intersection (refer to Fig. 4.2).

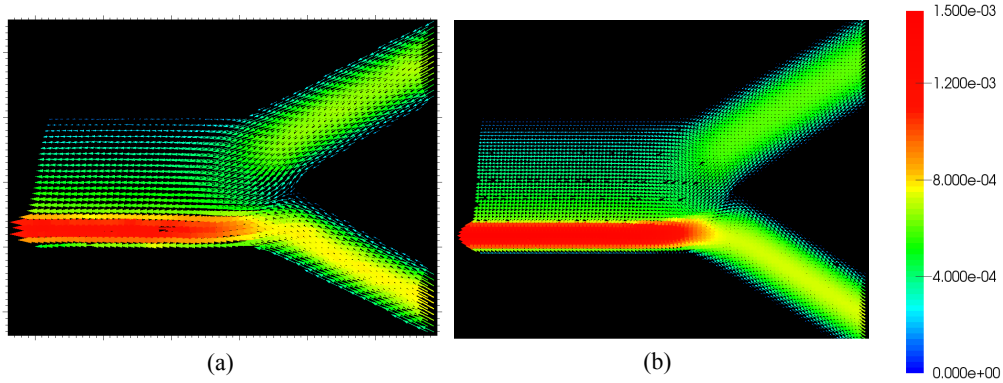

Figure 4.5: Three-dimensional mid-plane velocity vector distribution at the channel intersection for water and POLYOX^{TM} WSR 301 0.3%(wt) flow in the Y-microchannel: a) experimental values and b) numerical values.

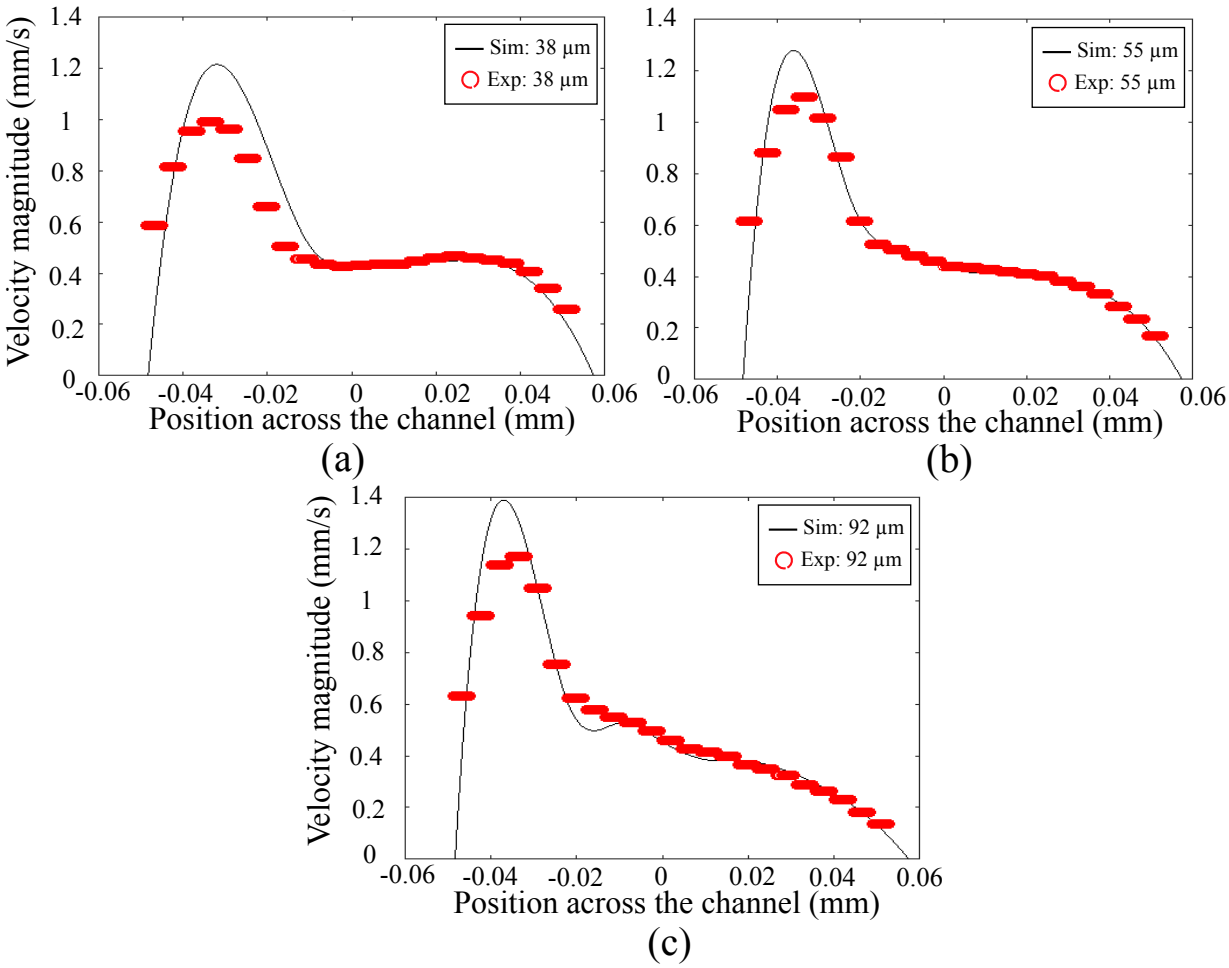

Figure 4.6: Three-dimensional mid-plane velocity profiles compared to the experiment for three different location: (a) 38 μm, (b) 55 μm and (c) 92 μm from the intersection.

4.2 Image processing technique validation

Image processing techniques are used for aggregate size detection. A MATLAB program developed for this purpose was described in Section 3.1.5. However, to ensure the proper functioning of the method, it is important to validate the methodology and hence verify the results (aggregate sizes) obtained using the developed code. First, particles with a known diameter range were inserted in the double Y-microchannel and analyzed to determine the average diameter detected. To validate the code for blood, human RBCs suspended in autologous plasma were inserted in the double Y-microchannel to be analyzed manually and compared to the results of the MATLAB code developed as well as those of the image processing technique using ImageJ [166].

4.2.1 Validation with hollow glass microspheres

Hollow glass microspheres (SPHERICELL, Potters Industries Inc.,) with a nominal diameter of 12 μm (diameter ranging from 2 μm to 25 μm), a density of 1.10 ± 0.05 $\frac{g}{cm^3}$ and a bulk density of 0.49 $\frac{g}{cm^3}$ [167] were suspended in deionized water at a ratio of 40%(v) and inserted into the double Y-microchannel at a flow rate of 10 $\frac{\mu L}{hr}$. Images of the flow were recorded with the high speed camera and were processed using the MATLAB code developed (60 frames at 8 $\frac{frames}{s}$). Figure 4.7 shows the shape and the different sizes of the hollow glass microspheres on a glass slide visualized under a microscope with a 20X lens magnification with $NA = 0.4$ and a DOF of 4 μm. Figure 4.8 shows the processed image of the glass microspheres when flowing at 10 $\frac{\mu L}{hr}$ in the microchannel. The colour coding was performed based on the sizes of the microspheres as shown in Table 4.1.

Table 4.1: Colour coding of the microspheres based on the different sizes.

Diameter (μm)	Colour
< 5	
$5 - 10$	
$10 - 15$	
$15 - 21$	
$21 - 25$	
> 25	

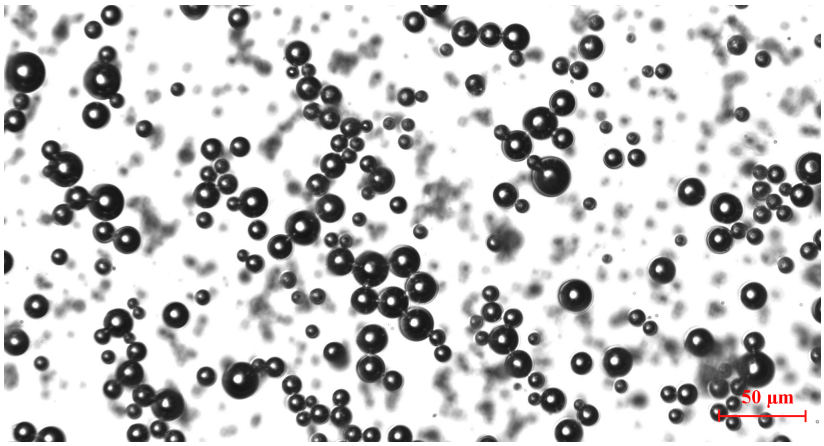

Figure 4.7: Hollow glass microspheres on a glass slide (at stasis) visualized under a microscope with a 20X lens magnification.

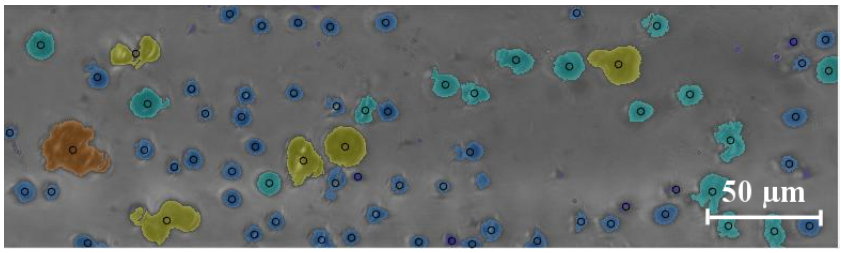

Figure 4.8: Processed image of the hollow glass microspheres flowing in the double Y-microchannel visualized under a microscope with a 20X lens magnification with the MATLAB code. The colour coding is based on the size of the microspheres as shown in Table 4.1.

The average area of the glass microspheres was found to be $64.8 \pm 0.7\ \mu m^2$ which corresponds to an average diameter of $9 \pm 0.05\ \mu m$. The results found do not precisely reflect the data provided by Potters Industries Inc. [167] where the nominal diameter is quoted as approximately 12 μm. Due to the large range of the microsphere sizes, as shown in Fig. 4.7, comparing the average diameter is not sufficient. Therefore, to further investigate the size difference, the size distribution obtained using the MATLAB code and the distribution provided by the manufacturer [167] were compared in Fig. 4.9. The size distribution obtained using image processing was found to be in a very good agreement with the size distribution provided by the manufacturer, where most of the microspheres have diameters ranging from 5 μm to 21 μm. The difference in diameter found could be caused by the size of the sample of microspheres analyzed. Indeed, in this present study, only a few microlitres were used and introduced into the microchannel and the flow was recorded for 7 seconds, which might not give the exact same distribution

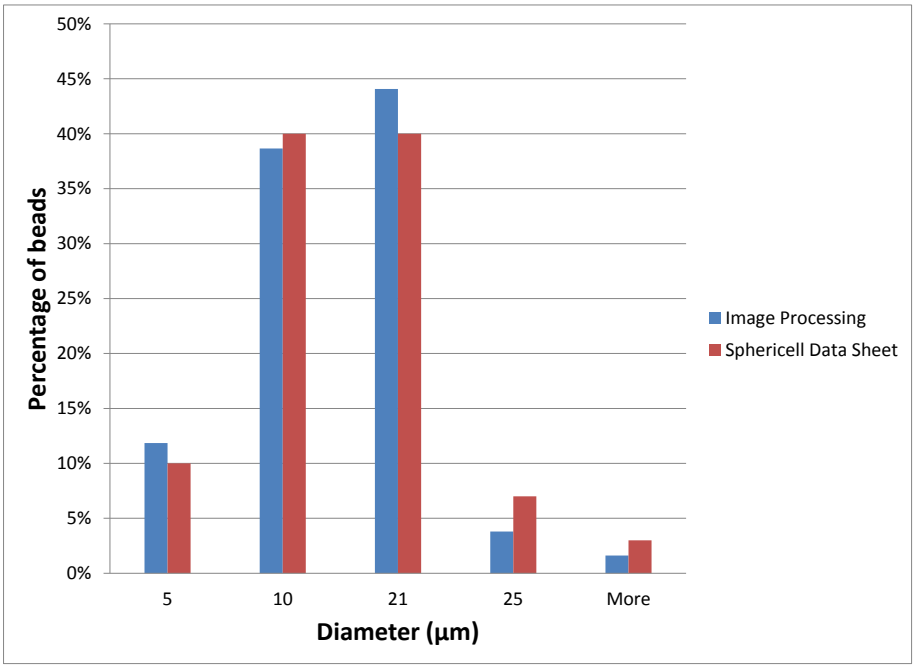

Figure 4.9: Size distribution of the microspheres in the microchannel (blue bars), obtained by MATLAB code processing compared to the manufacturer data [167] (red bars) in terms of sphere diameter.

as that provided by the manufacturer (measured using the laser light scatter technique). Also, due to the glass nature of the microspheres, some of these particles adhered onto the glass side of the microchannel, hence, affecting the distribution of the particles inside the microchannel.

4.2.2 Manual vs. automatic detection of RBC aggregates

To further validate the technique developed, image processing performed with MATLAB and ImageJ (to obtain the aggregate sizes in each image) was compared to manual detection of aggregates. The experiments were performed using human RBCs suspended at three hematocrits and flowing at different flow rates; 5% H with $Q = 10\ \frac{\mu L}{hr}$, 10% H with $Q = 10\ \frac{\mu L}{hr}$ and $Q = 5\ \frac{\mu L}{hr}$, and $15\%H$ with $Q = 10\ \frac{\mu L}{hr}$. Since the manual detection of the aggregates can be time-consuming, the analysis was done on eight images of the flow with an interval of 20 images, resulting in a frame rate of 8 $\frac{frames}{s}$ using the same

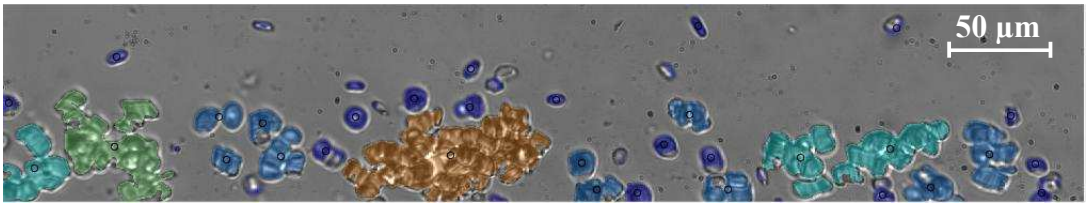

Figure 4.10: Processed image of human RBC aggregates flowing at $Q = 10\ \frac{\mu L}{hr}$ suspended at 10% H using the MATLAB code.

lens magnification of 20X with $NA = 0.4$ and a DOF of 4 μm. The same images were processed with MATLAB and ImageJ. Due to the subjectivity of the manual aggregate detection, the analysis was performed by two researchers without interference. The results are presented as an average of both measurements for each recording.

4.2.2.1 Processing with MATLAB

The code used was previously described in Section 3.1.5 and validated for known size microspheres in Section 4.2.1. Figure 4.10 represents the RBC aggregates detected using the MATLAB code. The average area of RBC aggregates was calculated and compared to the manual detection results.

4.2.2.2 Processing with ImageJ

Using ImageJ, the contrast of each frame is enhanced using the histogram equalization method. The image is then converted into a binary image with a threshold value matching the MATLAB threshold value. The aggregates are detected by using the "Analyze particles" function in ImageJ. To reduce the noise in the image, only particles larger than 100 *pixels* are detected, corresponding to particles with areas larger than of 5.3 μm^2. The measurements performed include the particles' areas, perimeters and centroids. The aggregates detected are outlined and numbered as shown in Fig. 4.11 (b). The average aggregate size is then calculated from the area of the detected particles.

4.2.2.3 Manual detection

The manual detection of the aggregates was performed using a feature of ImageJ to measure the number of pixels in an outlined area of an image. Eight frames were taken

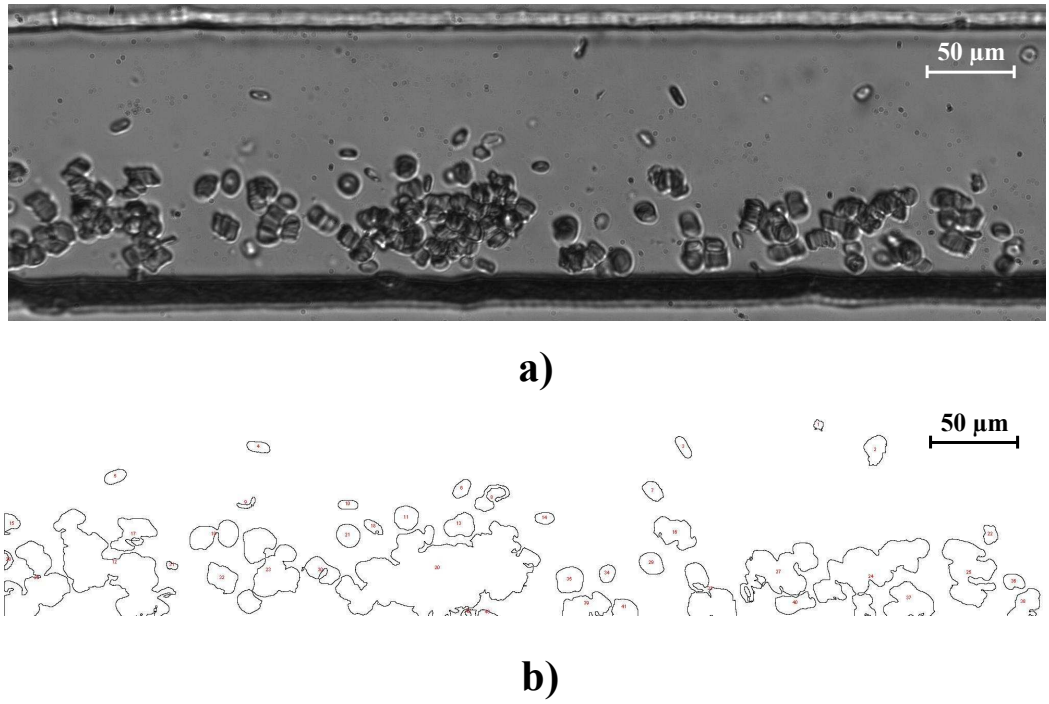

Figure 4.11: Original (a) and outlined (b) images of human RBC aggregates flowing at $Q = 10$ $\frac{\mu L}{hr}$ suspended at 10% H using ImageJ.

from the recorded flow of RBC aggregates for different hematocrits and different flow rates and were processed manually by two individuals. Within each frame, using the free hand selection, each aggregate in the image is outlined and numbered as shown in Fig. 4.12.

4.2.2.4 Results

Results of the detection of aggregates are shown in Figs. 4.10, 4.11 and 4.12 using the developed MATLAB code, ImageJ and manually respectively. Table 4.2 presents the average aggregate sizes (AAS) of the RBCs flowing at 5, 10 and 15% H for different flow rates, calculated using the different methods and the resultant error compared to the manual detection. Both automatic methods give similar results that are comparable to those obtained by manual detection. In fact, the error was found to be the lowest for the MATLAB code developed. However this could be mostly due to the filter applied in the code to reduce the salt and pepper noise in the image, which was not used in the ImageJ processing. We can also see that the error remains minimal for higher hematocrits, where the detection of the aggregates is difficult.

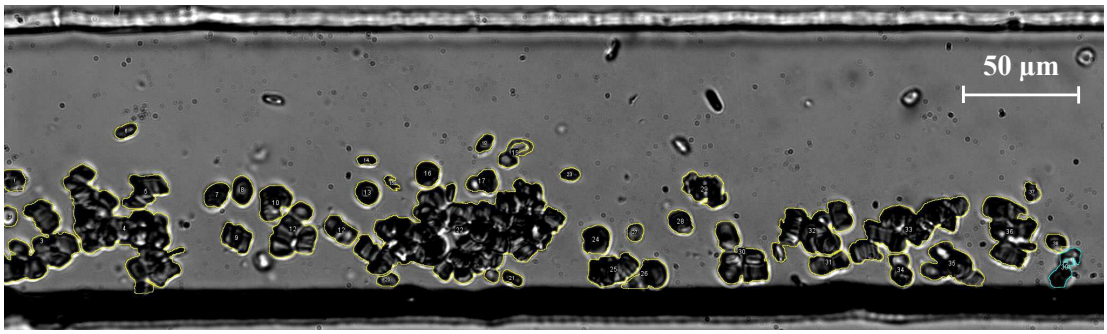

Figure 4.12: RBC aggregates flowing at $Q = 10\ \frac{\mu L}{hr}$ suspended at 10% H manually outlined using ImageJ.

Table 4.2: Average aggregate sizes (AAS) of RBCs flowing at 5, 10 and 15% H for different flow rates, calculated using ImageJ, developed MATLAB code and manually and the resultant error compared to the manual detection.

H (%)	Q ($\frac{\mu L}{hr}$)	AAS manual (μm^2)	AAS Image J (μm^2)	AAS code (μm^2)	Error (ImageJ) (%)	Error (MATLAB) (%)
5	10	308.1	343.1	294.6	11.3	4.3
10	10	202.3	180.0	193.2	11.0	4.5
10	5	221.1	194.9	226.1	11.8	2.2
15	10	374.6	341.2	384.1	8.92	2.5

In summary, the MATLAB code developed was validated using two different methods. It was shown to properly detect RBC aggregates and was proven to provide good results.

4.3 Viscosity measurement technique description and validation

The viscosity measurements are performed based on the theory of optical viscometry with co-flowing fluids previously developed and used in previous studies [21–25]. This methodology is based on the analytical solution of two co-flowing laminar streams of immiscible fluids. This technique relates the flow rate ratio of the two streams to the apparent viscosity ratio as shown in Eq. (3.2). In order to verify the proper implementation of the method, previous results of a glycerol solution (40% wt) entrained with deionized water at $\frac{Q_{glycerol}}{Q_{water}} = 0.25$ in a $150 \times 33\ \mu m$ Y-microchannel [19] were used. It was shown,

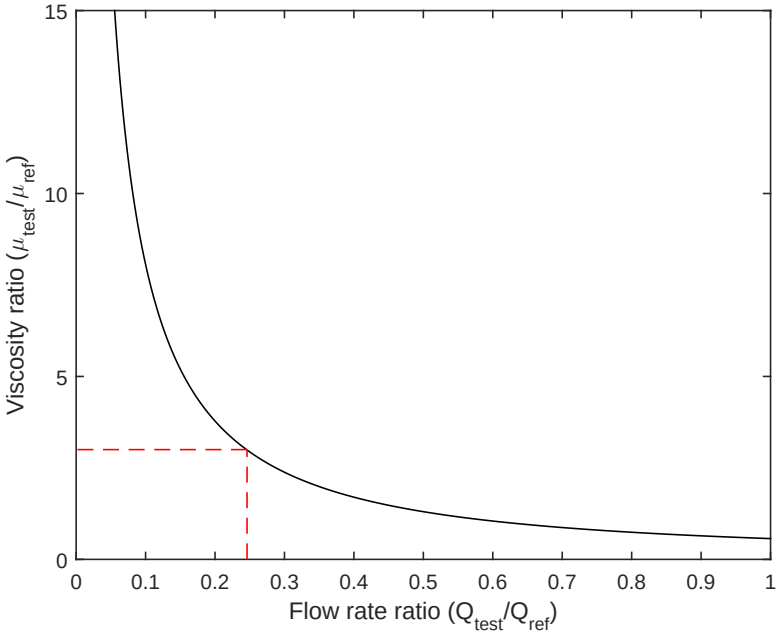

Figure 4.13: Viscosity ratio as a function of the flow rate ratio for the 150×33 μm Y-microchannel [19, 168]. The red lines highlight the viscosity ratio obtained for a flow rate ratio of 0.25.

numerically and experimentally, that with a viscosity ratio of $\frac{\mu_{glycrol}}{\mu_{water}} = 3$, the glycerol solution covers about 40% of the channel thickness, which corresponds to a dimensionless location $Y = -0.1$. Using the channel dimensions and the interface location, we can plot the viscosity ratio as a function of the flow rate ratio as presented in Fig. 4.13. The red lines in the plot highlights the viscosity ratio obtained for a flow rate ratio of 0.25, which is in accordance with the glycerol-water case [19].

To further verify the proper implementation of the analytical solution for blood viscosity measurements, the method was used to measure the viscosity of POLYOX^{TM} for the previously described case in Section 4.1.3. Knowing the flow rate of the fluids at both branches from the μPIV measurements and the location of the interface as shown in Fig. 4.2, the viscosity of the test fluid was found to be $\mu_{exp} = 15.88\ cP$ for a shear rate of $\dot{\gamma} = 6.77\ s^{-1}$, which represents a 5% error compared to the theoretical value obtained using Eq. (4.1).

This method provides good results for the measurement of the viscosity of a test fluid in the double Y-microchannel simultaneously with velocity measurements. However, an error of 4.7% in estimating the dimensionless location of the interface, Y, results in a

17.9% error in estimating the viscosity, whereas an error of 22% in estimating Y results in a 56.62% error in viscosity. This high error is due to the high aspect ratio of the double Y-microchannel which ranges between $\beta = 0.5 - 0.6$. In fact, Solomon and Vanapalli [25] show that this method is more suitable for low aspect ratios. Allowing for a lower aspect ratio for this application, however, will interfere with the aggregate formation and result in erroneous measurements. Since the estimation of the fluid interface location is crucial for this application, it was therefore performed by two independent researchers to avoid subjectivity.

Chapter 5

Red Blood Cell Aggregation Investigation and Characterization

5.1 Experimental procedure

Using the set-up presented in Chapter 3 and validated in Chapter 4, healthy porcine and human RBC aggregates (from different samples) are visualized and investigated in a double Y-microchannel. The porcine and human bloods are cleaned and suspended in their autologous plasma at 5, 10 and 15% H. The blood cleaning and preparation is detailed in Section 3.1.2. For each sample used, the aggregation index of the whole blood is determined based on the light transmission method as described in Section 1.4.5.6 using the RheoScan-A (Rheomeditech, Seoul, Korea) [169]. The hematocrit of the whole blood is also measured for the tests performed at $T = 37°C$ as detailed in Section 3.1.2. Each RBC suspension is tested at different flow rates to quantify the effect of shear rate on RBC aggregate sizes in controlled shear flows. Blood entering from the bottom branch of the microchannel is entrained by a PBS solution entering from the top branch at a flow rate four times higher than that in the blood branch. The flow is recorded using the high speed camera while the velocity field is assessed using the μPIV system. This set-up provides measurable, constant and controlled shear rates within the range of blood aggregation [19]. Shear rates are determined using the experimental velocity profiles measured using the μPIV system, by approximating the velocity within the blood layer to be an approximate linear profile as described in Section 3.1.4. To verify the accuracy of the velocity measurements, the root mean square, RMS, of the experimental velocity is calculated by averaging instantaneous velocity measurements for n_{image} as follows:

$$RMS = \sqrt{\frac{n_{image} \sum_{im=1}^{n_{image}} {x^2}_{im} - \left(\sum_{im=1}^{n_{image}} x_{im} \right)^2}{n_{image} \left(n_{image} - 1 \right)}} \tag{5.1}$$

where n_{image} represents the total number of images and x_{im} the measurement value in image im. The results obtained are given in terms of pixel displacement ΔX which are then scaled to the units of velocity ($\frac{mm}{s}$) based on the time interval between the pair of images, dt, and the scale factor α_{conv} set when calibrating the interline transfer camera as follows:

$$RMS = \frac{\alpha_{conv}\Delta X}{dt}. \tag{5.2}$$

The recordings performed with the high speed camera are processed using the code for image processing detailed and validated in Sections 3.1.5 and 4.2 respectively. This procedure has been published and detailed by Mehri *et al.* [170]. The blood viscosity is estimated based on the μPIV recordings and velocity profile in the branches as detailed and validated in Section 4.3. The viscosity data obtained are fitted using two empirical models commonly used to model blood flow: the Power law and Carreau models [171, 172].

5.2 Porcine RBC aggregation

Porcine RBC suspensions were tested at two different flow rates $Q = 10\ \frac{\mu L}{hr}$ and $Q = 5\ \frac{\mu L}{hr}$ at room temperature. Frames of the videos captured with the high-speed camera are shown in Fig. 5.1 for RBCs suspended at 10% H flowing with (a) $Q = 10\ \frac{\mu L}{hr}$ and (b) $Q = 5\ \frac{\mu L}{hr}$. Figure 5.2, shows the high speed camera captured frames of the RBC suspensions flowing at $Q = 10\ \frac{\mu L}{hr}$ at (a) 5%, (b) 10%, and (c) 15% H. Figure 5.3 shows the corresponding velocity profiles for the RBC suspensions at 5% (red data points), 10% (blue data points), and 15% H (green data points) flowing at $Q = 10\ \frac{\mu L}{hr}$. The width of the bar in the velocity profiles represents the size of the interrogation window used for the cross-correlation method. The RMS of the velocity, also displayed in Fig. 5.3 for each RBC suspension, are relatively small compared to the velocity values, indicating the accuracy of the velocity measurements, and hence shear rates. The interface locations, denoted as 'E' and indicated by solid vertical lines in Fig. 5.3, are obtained from the high-speed camera recordings. Averaging all the frames of the videos captured provides a background image that presents a clear delimitation of the interface. The simulated Newtonian velocity profile is included for comparison.

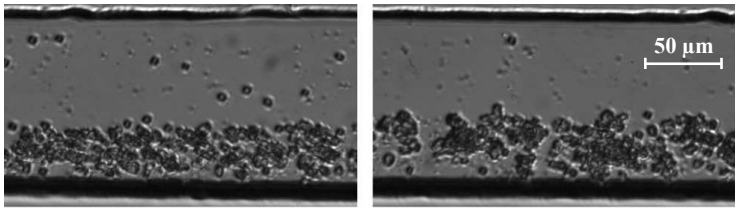

Figure 5.1: Captured high speed camera frames of the porcine RBCs suspended at 10% H flowing with (a) $Q = 10\ \frac{\mu L}{hr}$ and (b) $Q = 5\ \frac{\mu L}{hr}$.

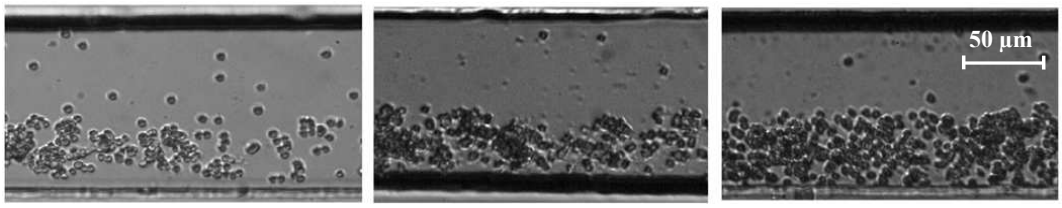

Figure 5.2: Captured high speed camera frames of porcine RBC suspensions flowing at $Q = 10\ \frac{\mu L}{hr}$ at (a) 5%, (b) 10%, and (c) 15% H.

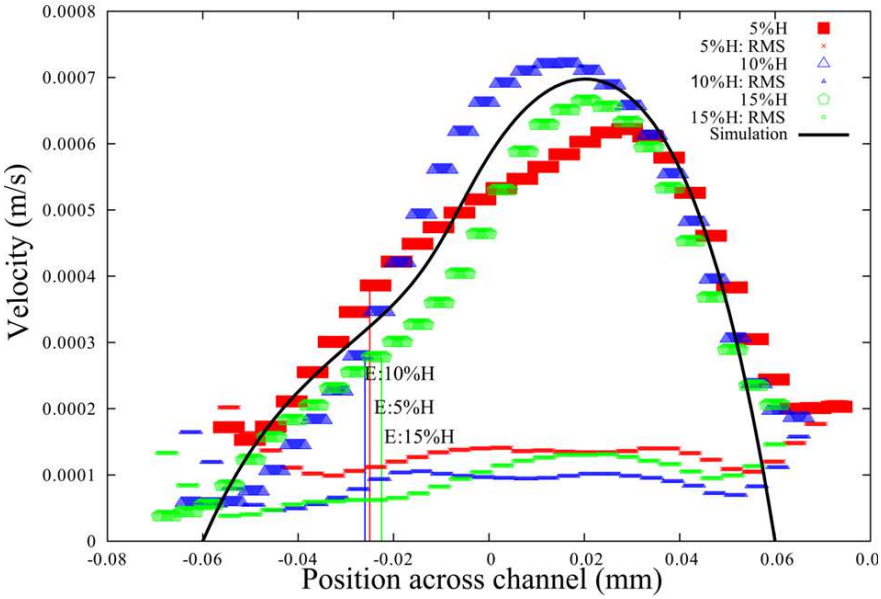

Figure 5.3: Experimental velocity profiles for porcine RBCs in plasma suspended at 5% H (red), 10% H (blue), 15% H (green), and simulated Newtonian velocity profile (solid line) for $110 \times 60\ \mu m$ double Y-microchannel with $Q = 10\ \frac{\mu L}{hr}$. The interface location is denoted by 'E' for the experiments. The corresponding RMS of velocity profiles are displayed.

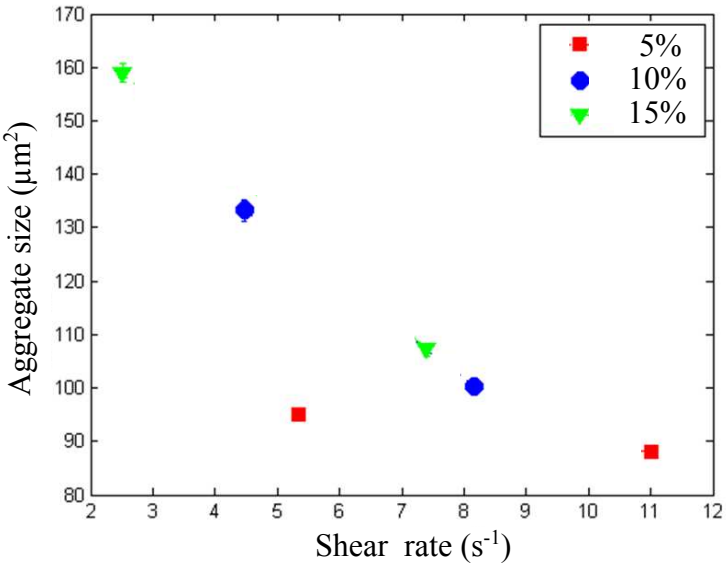

Figure 5.4: Average porcine RBC aggregate size as a function of the corresponding shear rate for the RBC suspensions at 5% (red), 10% (blue) and 15% (green) H.

The average aggregate size for each of the RBC suspensions was calculated as a function of the corresponding shear rate calculated from the μPIV data; the results are shown in Fig. 5.4. Error bars shown for each measurement depict the standard error obtained when averaging the results of several tests $(2-5)$ performed consecutively under the same conditions. Distributions of the number of RBCs in each aggregate for all the RBC suspensions (5%, 10% and 15% H) are shown in Figs. 5.5 (a), 5.5 (b) and 5.5 (c) respectively.

Comparing the average aggregate size for the 5% H suspension provided in Fig. 5.4, we see that the shear rate does not greatly affect the RBC aggregate size. In fact, due to the low RBC concentration in the 5% H suspension, larger aggregates are less likely to form with lower shear rates, confirming the findings of Kim *et al.* [46, 47]. However, for the higher hematocrits of 10% and 15%, larger aggregates are observed for lower shear rate values. It is also important to note that the hematocrit greatly affects the RBC behaviour since larger aggregates are seen with the 15% H suspension when compared to the 10% H suspension for the same range of shear rates. For the higher range of shear rates (7.41 to 11.02 s^{-1}), the average aggregate sizes found for the three different hematocrit levels differ slightly but do not fluctuate greatly (the aggregates range from

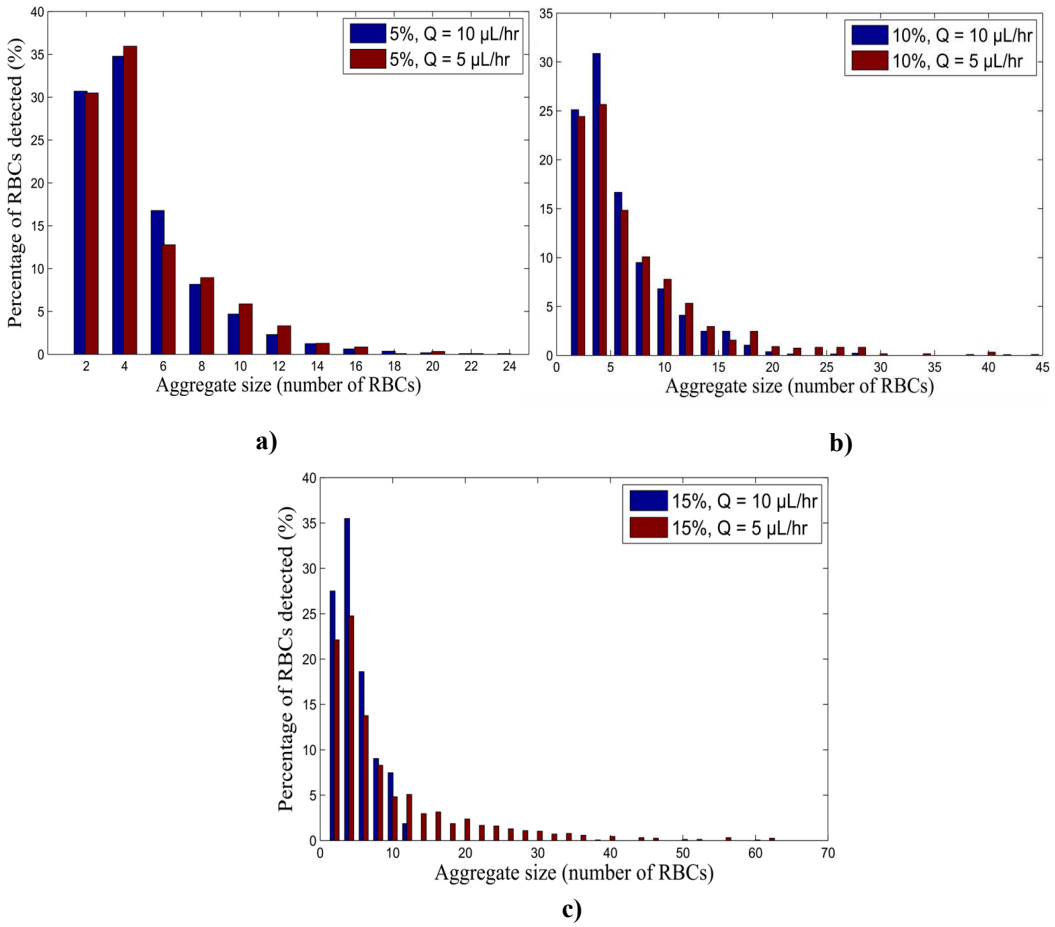

Figure 5.5: RBC Aggregate size distributions for porcine blood samples suspended at (a) 5%, (b) 10% and (c) 15% H flowing at $Q = 10\ \frac{\mu L}{hr}$ and $5\ \frac{\mu L}{hr}$.

87.8 to 107.2 μm^2). However, for the lower range of shear rates (2.51 to 5.36 s^{-1}), the average aggregate sizes greatly depend on the hematocrit level (the aggregates range from 95 to 159 μm^2), as observed in the original recordings in Fig. 5.2. The distribution of the number of RBC in the different aggregate sizes is also presented in Figs. 5.5 (a), 5.5 (b) and 5.5 (c) for 5%, 10% and 15% H, respectively. Again, we find that for the 5% H suspension, the distributions of the RBC aggregates in the blood layer are very similar for the two shear rates (Fig. 5.5 (a)). However, for 10% and 15% H (Figs. 5.5 (b) and 5.5 (c), respectively), larger aggregates were seen for the lower shear rate.

Experiments performed on porcine blood provide quantitative results for the RBC aggregates in a shear rate controlled system to quantify the effect of shear rate and hematocrit for porcine blood. This work provides a proof of concept for the methodology developed [173]. However, properties of porcine RBCs differ from those of human RBCs

(size, deformation and aggregability). Therefore, it is of a great importance to analyze human RBC aggregates.

5.3 Human RBC aggregation characterization

5.3.1 Experiments

Different human RBC suspensions (5%, 10% and 15% H) were tested under different conditions: at five different flow rates (35, 20, 10, 7.5 and 5 $\frac{\mu L}{hr}$) at a temperature of $T = 23°C$ (room temperature) and at $T = 37°C$ (body temperature) to visualize and quantify the effect of hematocrit, shear rate and temperature on the RBC aggregates and blood viscosity in the microfluidic controlled system.

5.3.1.1 Experiments at room temperature

Healthy and fresh human blood samples obtained from six volunteers ($n_{samples} = 6$) are used for the experiments conducted at room temperature. It is important to note that, for the different hematocrits, RBCs are suspended in their native plasma where protein concentration varies from one sample to another, hence affecting the aggregation process. All the RBC suspensions were tested following the procedure detailed in Section 5.1. Figures 5.6 (a), 5.6 (b) and 5.6 (c) show high speed camera captured and processed images of the human RBCs flowing at $Q = 35$ $\frac{\mu L}{hr}$ at 5%, 10%, and 15% H, respectively. The colour coding is performed based on the sizes of the detected RBC aggregates. Aggregates smaller than 100 μm^2 are labelled in blue, aggregates ranging between 100 and 360 μm^2 are labelled in green, while aggregates larger than 360 μm^2 are shown in red. Under the same flow conditions, a higher hematocrit engenders larger aggregates as clearly seen in Fig. 5.6 (c). Figures 5.7 (a) and 5.7 (b) show captured and processed frames of the human RBCs suspended at 10% H flowing with flow rates of 20 $\frac{\mu L}{hr}$ and 7.5 $\frac{\mu L}{hr}$, respectively. The colour coding is performed in the same manner as in Fig. 5.6. Figure 5.7 (b) shows a predominant red colour indicating that the aggregate sizes increase with diminishing flow rate in the channel. To verify the observed aggregate size variation with hematocrit and flow rate, we provide the distribution of the aggregate sizes within each frame for each recording. Figures 5.8 (a), 5.8 (b) and 5.8 (c) show the percentage of RBCs within

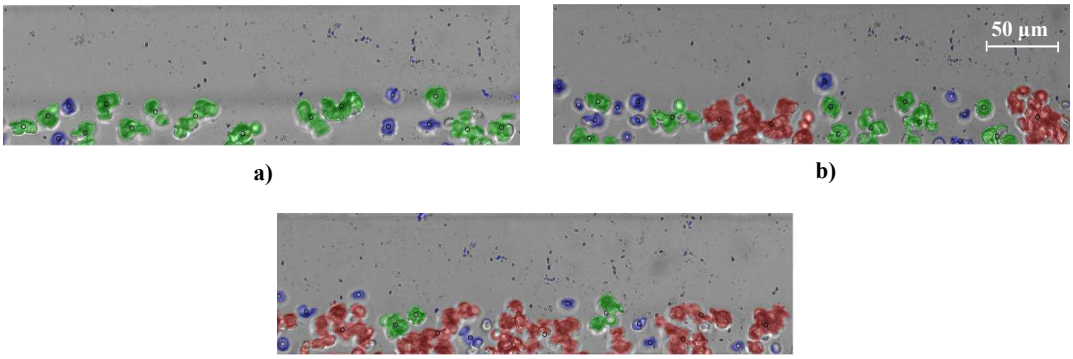

Figure 5.6: High speed camera captured and processed frames of human RBC suspensions flowing at $Q = 35\ \frac{\mu L}{hr}$ at (a) 5%, (b) 10%, and (c) 15% H at room temperature. The blue, green and red RBC aggregates correspond to sizes $< 100\ \mu m^2$, $100 - 360\ \mu m^2$ and $> 360\ \mu m^2$ respectively.

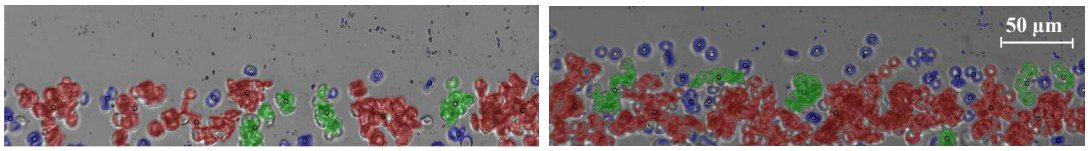

Figure 5.7: High speed camera captured and processed frames of human RBCs suspended at 10% H flowing with (a) $Q = 20\ \frac{\mu L}{hr}$ and (b) $Q = 7.5\ \frac{\mu L}{hr}$ at room temperature. The blue, green and red RBC aggregates correspond to sizes $< 100\ \mu m^2$, $100 - 360\ \mu m^2$ and $> 360\ \mu m^2$ respectively.

different aggregate sizes for 5%, 10% and 15% H, respectively for blood sample Aa03A. Here, the aggregate sizes are shown as a number of estimated RBCs. This estimated number is calculated based on the aggregate sizes measured in pixels divided by the measured size of one RBC (in pixels). For the 5% H suspension (Fig. 5.8 (a)), lowering the flow rate results in slight differences in the aggregate distribution. For a larger flow rate ($20\ \frac{\mu L}{hr}$), 95% of the RBCs form aggregates smaller than 64 estimated RBCs as opposed to 81% for a smaller flow rate ($7.5\ \frac{\mu L}{hr}$). However, for the 10% H suspension, differences in the size distribution are more prominent, where larger aggregates can be found for smaller flow rates. For the 15% H suspension, major differences are noted. More than 90% of the RBCs are detected in the largest aggregate sizes. However, it is important to note that with a larger number of RBCs in the channel flowing at low shear rates (hence forming larger aggregates), the detection of individual aggregates becomes

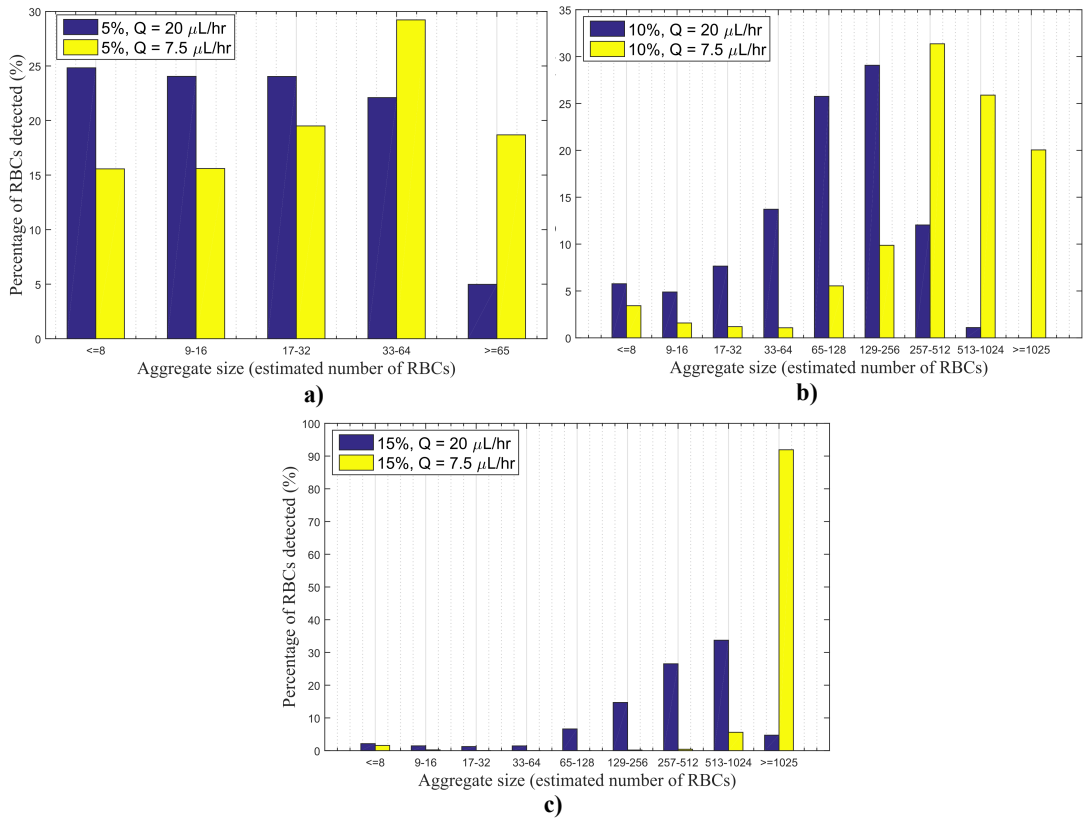

Figure 5.8: Aggregate size distribution for human RBCs suspended at (a) 5% H, (b) 10% and (c) 15% flowing at $Q = 20\ \frac{\mu L}{hr}$ (blue bars) and 7.5 $\frac{\mu L}{hr}$ (yellow bars) for sample Aa03A at room temperature.

difficult due to the lack of contrast with the image background as shown in Fig. 5.9.

Collecting all the measurements of shear rate, viscosity and aggregate sizes, the average aggregate size and viscosity can be plotted as a function of shear rate for each different sample.

Results Figures 5.10 (a), 5.10 (b) and 5.10 (c) represent the average RBC aggregate sizes at 5%, 10% and 15% H, respectively, detected for the corresponding shear rate in the blood layer. Error bars shown for each measurement depict the standard error obtained when averaging the results of several tests $(2-5)$ performed consecutively under the same conditions. The viscosity measured is also plotted as a function of shear rate in Figs. 5.11 (a), 5.11 (b) and 5.11 (b) for 5%, 10% and 15% H, respectively. For the Power law model, the data are fitted using a linear least squares method to minimize the difference between the data set and the linear model. The expression for viscosity (Eq.

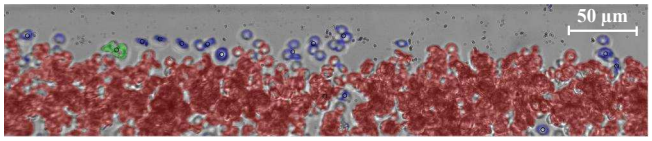

Figure 5.9: High speed camera captured and processed frame of human RBC suspensions flowing at $Q = 7.5\ \frac{\mu L}{hr}$ at 15% H at room temperature. The blue, green and red RBC aggregates correspond to sizes of $< 100\ \mu m^2$, $100 - 360\ \mu m^2$ and $> 360\ \mu m^2$, respectively.

(4.1)) is transformed as follows:

$$log(\mu_{app}) = log(K) + (n-1)log(\dot{\gamma}). \tag{5.3}$$

In this manner, the fluid consistency index K and the non-Newtonian behaviour index n can be found as the intercept and the slope of the regression, respectively. For the Carreau model, the experimental data are fitted using a nonlinear least-squares solver using the Levenberg-Marquart method [174] as follows:

$$min||f(x)||_2^2 = min(f_1(x)^2 + f_2(x)^2 + ... + f_n(x)^2) \tag{5.4}$$

where $f(x)$ represents the function to be minimized, defined as the difference between the experimental data and the model to be fitted and x represents x-abscissa (shear rate in this case). The parameters to be found include the infinite shear viscosity μ_∞, the zero shear viscosity μ_0, the relaxation time λ , and the power law index n. Parameters from the study of Cho and Kensey [79] for viscosity measurements of blood at 45% H at 37°C were used as initial guesses for the nonlinear least-squares method as follows:

$$\begin{aligned} \mu_{\infty_o} &= 3.45\ cP \\ \mu_{0_o} &= 56\ cP \\ n_o &= 0.3568 \\ \lambda_o &= 3.313\ s. \end{aligned}$$

Tables 5.1 and 5.2 summarize the parameters obtained from the Power law and Carreau models respectively for the different hematocrits. The parameters obtained from the fitted curves are used in the numerical simulations. The resultant coefficient of determi-

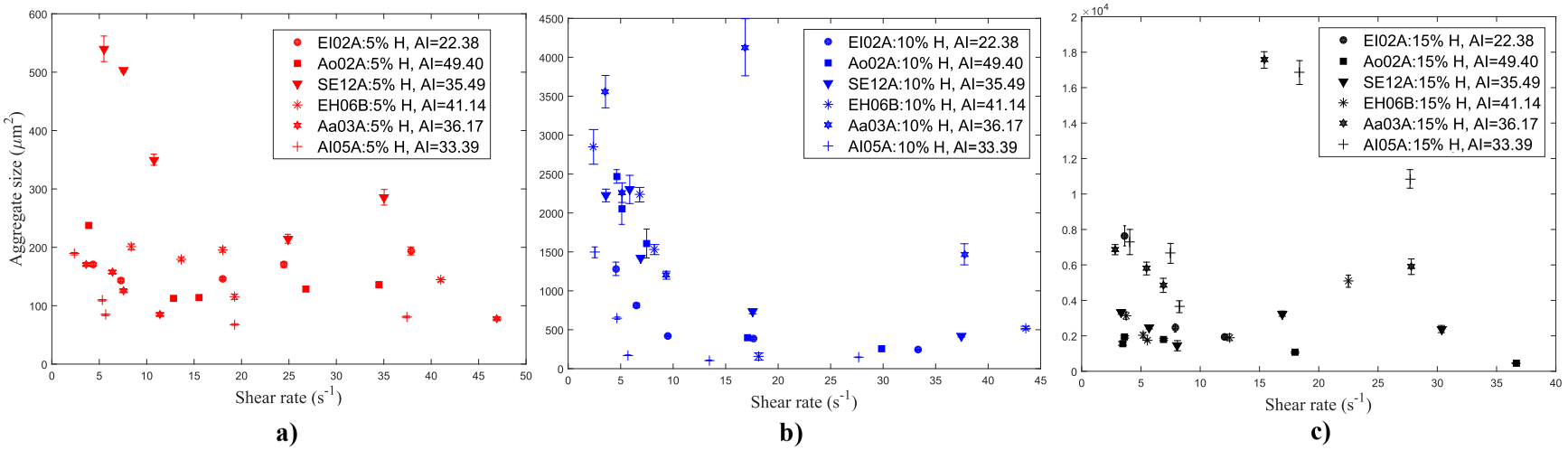

Figure 5.10: Average human RBC aggregate sizes for six different blood samples suspended at (a) 5% (b) 10% and (c) 15% H as a function of shear rate at room temperature. Error bars for each sample are provided for the standard error of several $(2-5)$ tests performed consecutively. The aggregation index (AI) is provided for each sample.

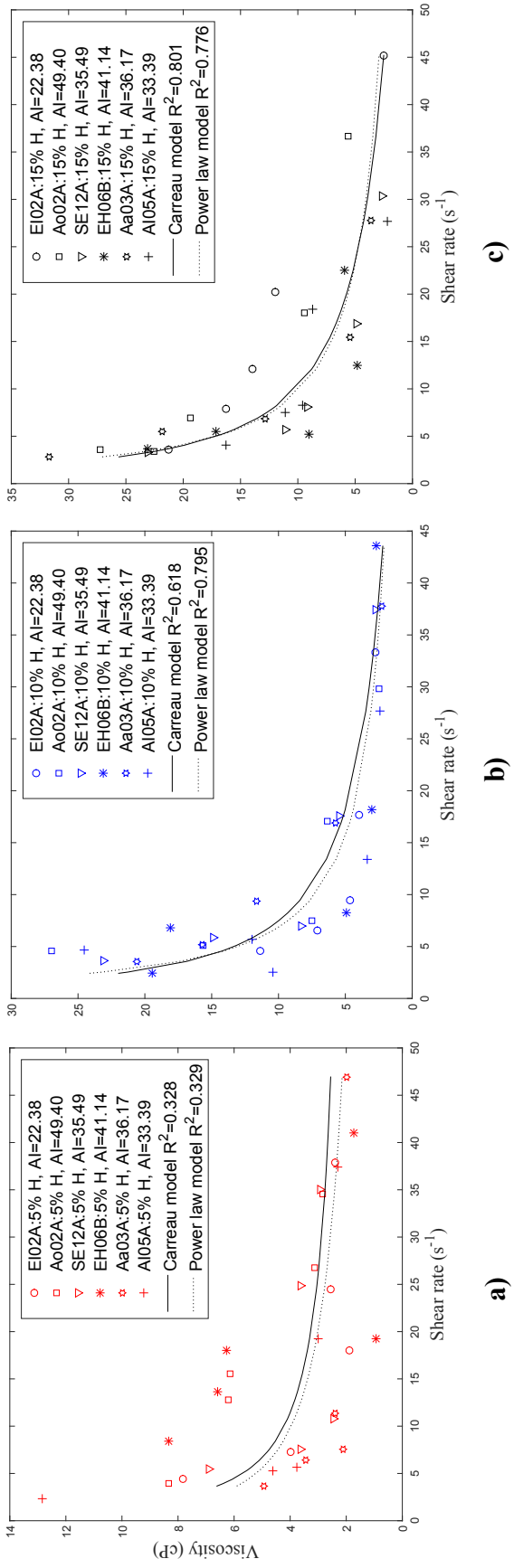

Figure 5.11: Viscosity measurement for six different human blood samples suspended at (a) 5% (b) 10% and (c) 15% H as a function of shear rate at room temperature. Curve fittings of Power law (dotted black curve) and Carreau (solid black curve) models are also shown with the associated R^2 value. The aggregation index (AI) is provided for each sample.

Table 5.1: Summary of the non-Newtonian parameters for the Power law model for human blood suspended at 5%, 10% and 15% H at room temperature with the corresponding R^2 and ${R^2}_{adjusted}$.

Hematocrit (%)	K (cP)	n -	R^2 -	${R^2}_{adjusted}$ -
5%	9.9	0.6032	0.329	0.305
10%	50.9	0.156	0.795	0.788
15%	62.2	0.6032	0.776	0.768

Table 5.2: Summary of the non-Newtonian parameters for the Carreau model for human blood suspended at 5%, 10% and 15% H at room temperature with the corresponding R^2 and RMSE.

Hematocrit (%)	μ_0 (cP)	μ_∞ (cP)	λ (s)	n -	R^2 -	RMSE (cP)
5%	26.9	1.6	3.313	0.353	0.328	1.846
10%	89.9	1.6	3.312	0.369	0.618	4.976
15%	118.6	2.3	3.312	0.362	0.801	3.852

nation, R^2, for both methods is calculated as follows:

$$R^2 = 1 - \frac{\sum_{j=1}^{m} \left({\mu^j}_{exp} - {\mu^j}_{fit}\right)^2}{\sum_{j=1}^{m} \left({\mu^j}_{exp} - \overline{\mu}_{exp}\right)^2} \tag{5.5}$$

where ${\mu^j}_{exp}$ represents the experimental data point j of viscosity, ${\mu^j}_{fit}$ the fitted data point j of viscosity and m the number of data points. For the linear least squares method, increasing the data points results in a higher R^2, which might not correctly reflect the goodness of the fit. Therefore, the adjusted coefficient of determination, ${R^2}_{adjusted}$, that accounts for the number of points and parameters is also provided in Table 5.1. The adjusted coefficient of determination is calculated as follows:

$${R^2}_{adjusted} = 1 - \frac{\sum_{j=1}^{m} \left({\mu^j}_{exp} - {\mu^j}_{fit}\right)^2 / (m-p)}{\sum_{j=1}^{m} \left({\mu^j}_{exp} - \overline{\mu}_{exp}\right)^2 / (m-1)} \tag{5.6}$$

where p is the number of parameters to be determined from the fitted curve. It is important to note that the coefficient of determination is usually calculated for linear

least squares fit and was shown to not be significant for the non-linear least squares model despite its extensive use for biochemical research [175]. The root mean square error (RMSE) is presented in Table 5.2 and is calculated as follows:

$$RMSE = \sqrt{\frac{\sum_{j=1}^{m} \left(\mu^j{}_{exp} - \mu^j{}_{fit}\right)^2}{m - p}}. \tag{5.7}$$

The RMSE estimates the standard deviation of the random component of the data. This measure is intuitive as it has the same units as those of the variable to be fitted. The corresponding coefficients of determination for the different hematocrits are still provided in this study for comparison purposes.

Discussion The results show that for the 5% H suspensions (Fig. 5.10 (a)), changes in shear rates do not greatly influence the aggregate sizes detected, which corresponds to the observations made for the RBC distributions in the different sizes of aggregates for different shear rates (Fig. 5.8 (a)). The aggregate sizes for all the shear rate values range from 100 to 550 μm^2. The error obtained is relatively small for all the measurements with the exception of sample SE12A for the lowest shear rate value. For the 10% H (Fig. 5.10 (b)), decreasing the shear rate in the blood layer translates to a significant increase in the aggregate sizes. For larger shear rates ($> 10\ s^{-1}$), the average size of aggregates ranges between 200 to 1500 μm^2, whereas for shear rates less than 10 s^{-1}, the aggregate sizes reach up to 3150 μm^2. It can be noted that the standard error increases slightly for the lower shear rates, indicating a difference in the average aggregate sizes in time under the exact same conditions. This could be due to an increase in the sedimentation rate in the tubes caused by the hematocrit increase. Increasing the hematocrit to 15%, the aggregate sizes increase for the different shear rates tested. The same trend as for the 10% hematocrit can be noted where the average aggregate size increases significantly for shear rates smaller than 10 s^{-1}. However, for most of the measurements, the error is high compared to the measurement value. Again, due to the difficulty of aggregate detection at small shear rates for the higher hematocrits (10% and 15% H), it becomes difficult to interpret the results with certitude, and therefore, this will require further investigation.

No apparent relationship was noticed between the aggregation index measured for the

whole blood and the average aggregate sizes measured for the different hematocrits. The absence of a relationship between the two methods for aggregate detection can be due to several factors. In fact, the hematocrit of the whole blood was not assessed, which could influence the aggregation index obtained; a high hematocrit leads to a higher aggregation index. Therefore, two samples with the same aggregation index but different hematocrits can engender different results. It was not possible to directly measure the aggregation index for the suspensions prepared at the three different hematocrit levels since the low number of RBCs allows larger gaps between the aggregates resulting in a saturation of the light transmitted in the Rheoscan-A [169].

For the 5% H suspensions (Fig. 5.11 (a)), the data were fitted with a coefficient of determination of $R^2 = 0.329$. This clearly indicates that the data are not well represented by the Power law model considering the low volume of RBCs. The R^2 value for the Carreau model is within the same range as for the Power law model. Therefore, the same conclusion can be drawn. However, the RMSE value (Table 5.2) indicates a relatively small error, which indicates small variation of the random component of the data. The fitted data and the non-Newtonian parameters are used in the numerical code for velocity profiles comparison. The data are better represented by the Power law and Carreau models for higher hematocrits as shown in Figs. 5.11 (b) and 5.11 (c). For the Power law model, the coefficient of determination increases to $R^2 = 0.795$ and $R^2 = 0.776$ for 10% and 15% H, respectively. The adjusted R^2 value was found to be ${R^2}_{adjusted} = 0.788$ and ${R^2}_{adjusted} = 0.768$ for 10% and 15% H, respectively, which do not show a significant difference. This indicates that increasing the number of points does not improve the fit. For the Carreau model, the coefficient of determination increases to $R^2 = 0.618$ and $R^2 = 0.801$ for 10% and 15% H respectively. The RMSE value found for 10% and 15% H (4.976 cP and 3.852 cP, respectively) indicates a lower variation of the random component of the data for the 15% H, which indicates a better fit for the higher hematocrit.

Although a trend can be seen when combining all the samples in Figs. 5.10 and 5.11, discrepancies between the blood samples are clearly present, which give rise to randomness in the variance of the data. This is mainly due to the physiological nature of blood varying from an individual to another. Although some factors are being controlled, such

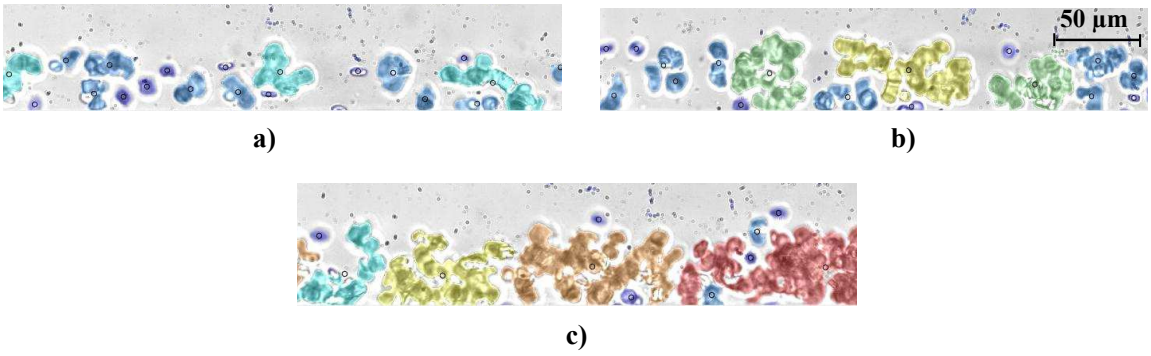

Figure 5.12: High speed camera captured and processed frames of human RBC suspensions flowing at $Q = 35\ \frac{\mu L}{hr}$ at (a) 5%, (b) 10%, and (c) 15% H at 37°C. The colour coding of the aggregate sizes is detailed in Table 5.3.

as the hematocrit and shear rate, other factors may greatly influence the results. For instance, the aggregation index measured was found to vary significantly between the different samples. It was shown, by Baskurt *et al.* [45], that this variation was solely due to physiological differences between donors and that these differences persist when using an artificial medium (polymer) instead of autologous plasma. Also, as previously mentioned, the hematocrit of the whole sample may affect the aggregation index measurement. The concentration of fibrinogen in the plasma also affects the aggregation mechanism: it does not remain constant from donor to donor. Plasma viscosity has been shown to be indicative of the molecular weight and molecular shape of the protein [176]. Therefore, plasma viscosity can be used as another controlling factor to compare the aggregation size and viscosity between samples. However, it is important to note that plasma viscosity is not directly linked to fibrinogen concentration and hence cannot fully explain the differences between the samples.

5.3.1.2 Experiments at body temperature T=37° C

For the tests performed at $T = 37$°C, healthy and fresh human blood samples, obtained from five healthy volunteers ($n_{samples} = 5$), were used. As for the tests performed at room temperature, all the RBC suspensions were tested following the procedure detailed in Section 5.1. Figures 5.12 (a), 5.12 (b) and 5.12 (c) show high speed camera captured and processed images of the human RBCs flowing at $Q = 35\ \frac{\mu L}{hr}$ at 5%, 10%, and 15% H, respectively at 37°C. The colour coding is performed based on the sizes of the detected

Table 5.3: Colour coding of the detected aggregates based on the different sizes.

Area (μm^2)	Colour
< 100	
$100 - 499$	
$500 - 999$	
$1000 - 1499$	
$1500 - 1999$	
$2000 - 2999$	
$>= 3000$	

aggregates. Table 5.3 summarizes the range of aggregate sizes corresponding to each colour in the image. A visual inspection the aggregate sizes in the images shows that an increase in the hematocrit corresponds to an increase in the aggregate sizes. The data were collected in the same manner as that described in Section 5.3.1.1.

Results Figures 5.13 (a), 5.13 (b) and 5.13 (c) represent the average RBC aggregate sizes detected for the corresponding shear rate in the blood layer at 5%, 10%, and 15% H, respectively at 37°C. Error bars shown for each measurement depict the standard error obtained when averaging the results of several tests performed consecutively under the same conditions. The aggregation index, the hematocrit of the whole blood as well as the plasma viscosity μ_p are provided for comparison purposes. The plasma viscosity was measured using the m-VROC^{TM} viscometer (Rheosence Inc., USA) with temperature control. The measured apparent viscosity is plotted as a function of shear rate as shown in Figs. 5.14 (a), 5.14 (b) and 5.14 (b) for 5%, 10% and 15% H, respectively. In order to obtain more control over the viscosity data, the apparent viscosity is divided by the donor-specific plasma viscosity to obtain the relative viscosity $\mu_{relative}$. The relative viscosity is shown as a function of shear rate in Figs. 5.14 (d), 5.14 (e) and 5.14 (f) for 5%, 10% and 15% H, respectively.

Table 5.4 summarizes the non-Newtonian parameters obtained for the Power law model fit to the apparent viscosity data and the corresponding R^2 and $R^2{}_{adjusted}$ calculated using Eqs. (5.5) and (5.6), respectively. Table 5.5 summarizes the non-Newtonian parameters obtained for the Carreau model fit to the apparent viscosity data and the corresponding R^2 and RMSE calculated using Eqs. (5.5) and (5.7), respectively.

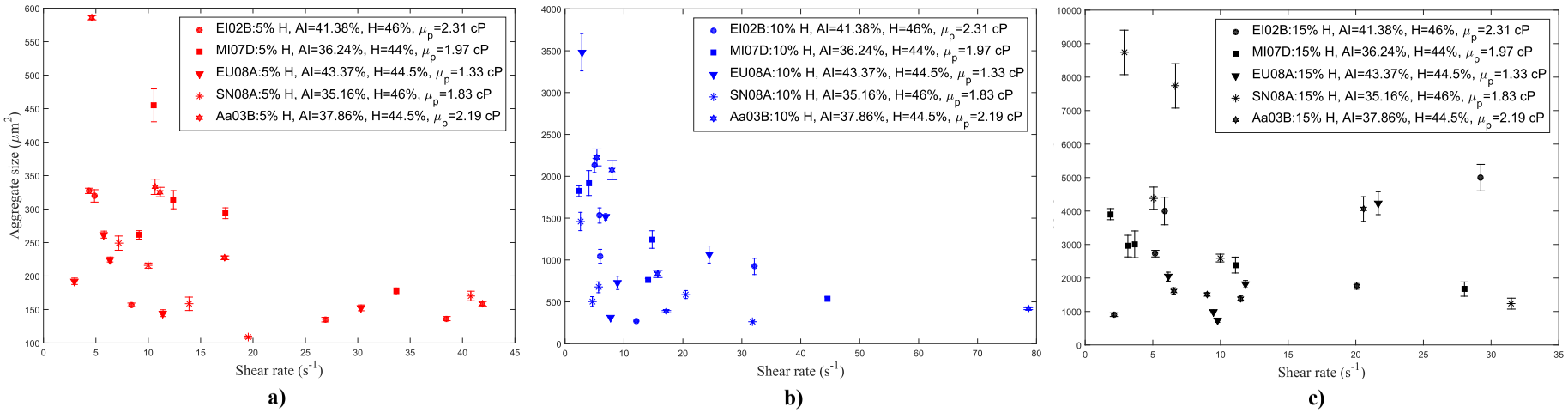

Figure 5.13: Average human RBC aggregate sizes for five different blood samples suspended at (a) 5% (b) 10% and (c) 15% H as a function of shear rate at 37°C. Error bars for each sample are provided for the standard error of several $(2-5)$ tests performed consecutively. The aggregation index (AI), the hematocrit of the whole blood and the plasma viscosity μ_p are also provided.

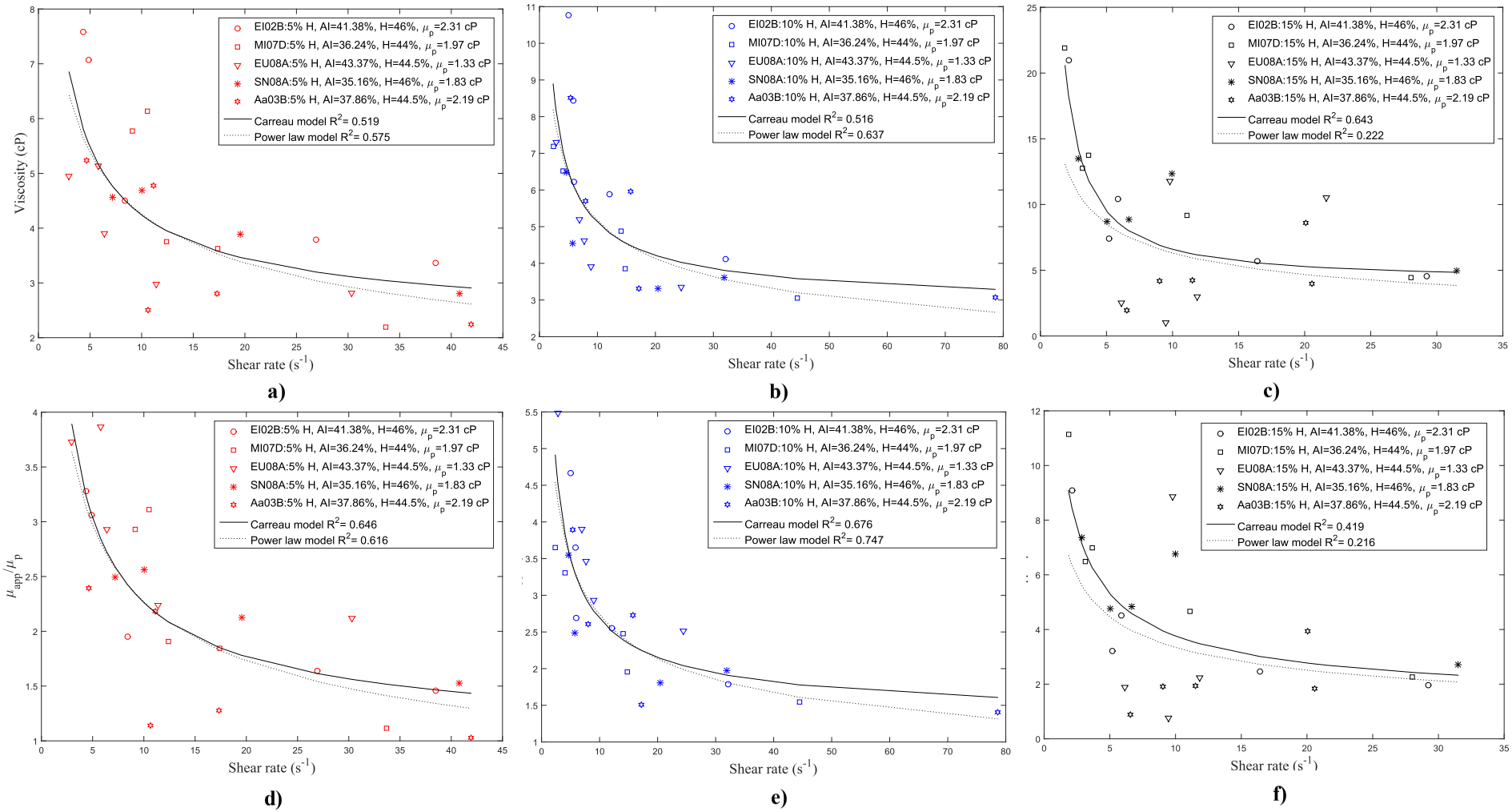

Figure 5.14: Apparent viscosity measurement for five different human blood samples suspended at (a) 5% (b) 10% and (c) 15% H as a function of shear rate and relative viscosity measurement for five different blood samples suspended at (d) 5% (e) 10% and (f) 15% H as a function of shear rate at 37°C. Curve fittings of Power law (dotted black curve) and Carreau (solid black curve) models are also shown with the associated R^2 value. The AI, the hematocrit of the whole blood and the plasma viscosity are provided for each sample.

Table 5.4: Summary of the non-Newtonian parameters for the Power law model for human blood suspended at 5%, 10% and 15% H fit to the apparent viscosity data, with the corresponding R^2 and $R^2_{adjusted}$ at 37°C. The parameters that are currently used in the literature for blood at 45% H tested at 37°C are provided.

Hematocrit (%)	K (cP)	n -	R^2 -	$R^2_{adjusted}$ -
5%	9.3	0.6604	0.575	0.5561
10%	10.8	0.6798	0.637	0.6212
15%	17.1	0.5678	0.222	0.1882
45%	35	0.6	Cho and Kensey [79] (1991)	
45%	17	0.708	Shibeshi and Collins [177] (2005)	

Table 5.5: Summary of the non-Newtonian parameters for the Carreau model for human blood suspended at 5%, 10% and 15% H fit to the apparent viscosity data, with the corresponding R^2 and RMSE at 37°C. The parameters that are currently used in the literature for blood at 45% H tested at 37°C are provided.

Hematocrit (%)	μ_0 (cP)	μ_∞ (cP)	λ (s)	n -	R^2 -	RMSE (cP)
5%	23.3	2.0	3.313	0.3527	0.519	1.057
10%	26.4	2.6	3.313	0.3534	0.516	1.466
15%	139.5	4.2	3.314	−0.152	0.643	3.489
45%	56	3.45	3.313	0.356	Cho and Kensey [79] (1991)	

Table 5.6 summarizes the non-Newtonian parameters obtained for the Power law model fit to the relative viscosity data and the corresponding R^2 and $R^2_{adjusted}$. Table 5.7 summarizes the non-Newtonian parameters obtained from the Carreau model fit to the relative viscosity and the corresponding R^2 and RMSE. Figures 5.15 (a), 5.15 (b) and 5.15 (c) present the relative viscosity as a function of the average aggregate sizes for 5%, 10% and 15% H, respectively at 37°C. The aggregation index (AI) is provided for each sample.

Discussion The average RBC aggregate sizes found for the 5% H blood samples in Fig. 5.13 (a) do not vary greatly with the shear rate as in the room temperature case. The samples that present higher average aggregate sizes ($159 - 586\ \mu m^2$) for different shear rates ($4.6 - 41.9\ s^{-1}$) have a relatively high plasma viscosity $\mu_{pAa03B} = 2.19 \pm 0.13$

Table 5.6: Summary of the non-Newtonian parameters for the Power law model for human blood suspended at 5%, 10% and 15% H fit to the relative viscosity data, with the corresponding R^2 and $R^2{}_{adjusted}$ at 37°C.

Hematocrit (%)	K $\times$ μ_p	n -	R^2 -	$R^2{}_{adjusted}$ -
5%	5.6	0.6106	0.616	0.5986
10%	6.2	0.6463	0.747	0.7361
15%	8.7	0.5859	0.216	0.1821

Table 5.7: Summary of the non-Newtonian parameters for the Carreau model for human blood suspended at 5%, 10% and 15% H fit to the relative viscosity data, with the corresponding R^2 and RMSE at 37°C.

Hematocrit (%)	μ_0 $\times$ μ_p	μ_∞ $\times$ μ_p	λ (s)	n -	R^2 -	RMSE $\times$ μ_p
5%	14.1	0.9	3.313	0.3524	0.644	0.507
10%	15.3	1.2	3.313	0.3529	0.676	0.617
15%	27.3	1.0	3.314	0.3539	0.419	2.347

cP and an average AI, $AI_{Aa03B} = 37.86 \pm 0.21$. However, for the sample with the highest aggregation index, $AI_{SN08A} = 43.37 \pm 0.27$, and the lower plasma viscosity, $\mu_{pSN08A} = 1.33 \pm 0.05cP$, lower average aggregate sizes ($145 - 262\ \mu m^2$) were found for the varying shear rates ($2.9 - 30.3\ s^{-1}$). For the 10% H suspensions (Fig. 5.13 (b)), the average aggregate size does vary with the shear rate and increases especially at low shear rates ($< 10\ s^{-1}$). However, for intermediate shear rates ($10 - 30\ s^{-1}$), a large spread of data can be noted. The samples with higher aggregation indices ($AI_{SN08A} = 43.37 \pm 0.27$ and $AI_{EI02B} = 41.38 \pm 1.09$) present a rapid decrease of aggregate sizes for lower shear rates ($2.84 - 8\ s^{-1}$), which was not the case for the samples with smaller aggregation indices. As for the 5% H suspensions, the higher aggregation sizes are found for the samples with higher plasma viscosities ($\mu_{pEI02A} = 2.31 \pm 0.08cP$ and $\mu_{pAa03A} = 2.19 \pm 0.13$ cP), with the exception of sample SN08A with the lowest plasma viscosity. For the smallest shear rate of $\dot{\gamma} = 2.84\ s^{-1}$, a high standard error was found for the aggregation size: for this case, with small shear rate and high aggregation of the sample (from AI measured), aggregate size detection was difficult to perform accurately. For the 15% H

suspensions, no clear trend could be detected due to the different outliers. The average aggregate sizes above 4000 μm^2 presented high standard errors and were difficult to detect due to the compactness of the RBCs in the channel as demonstrated in Fig. 5.9. It is difficult to interpret the results with certitude at 15% H. The same trend was found for aggregate sizes obtained at room temperature and body temperature, with lower aggregate sizes at body temperature. It is well known that temperature greatly affects blood behaviour [45]. The temperature effect is commonly reported in the viscosity measurements, however no quantification of the temperature effect is provided in terms of aggregate sizes. Neumann *et al.* [52] did show the temperature dependence of RBC aggregation and stated that a decrease in temperature engenders a higher resistance of the RBC aggregates to the hydrodynamic dispersion and hence would increase the absorption energy of the aggregates due to an increase in molecular adsorption stress. However, this temperature dependence was not directly related to RBC aggregate sizes.

The measured apparent viscosity is plotted as a function of shear rate for 5%, 10% and 15% H in Figs. 5.14 (a), 5.14 (b) and 5.14 (c), respectively. Analyzing the fitted curves obtained for the 5% H shows that the Power law and the Carreau models explain about 50% of the variance of the data ($R^2 = 0.575$ and $R^2 = 0.519$ for Power law and Carreau models respectively). Increasing the hematocrit to 10% and 15% H slightly improves the corresponding coefficient of determination. For the Carreau model, the RMSE value for 10% H (Table 5.5) was found to be relatively small (RMSE= 1.466 cP) and hence indicates a small variation of the random component of the data. The highest R^2 was found to correspond to the fitted curve of the Carreau model for the 15% H suspensions with a value of $R^2 = 0.643$ with RMSE= 3.489 cP, which is slightly more significant compared to the experimental data, indicating a larger standard deviation of the random component of the data. In order to generalize the data and avoid donor-specific variations in viscosity, the relative viscosity is plotted as a function of the shear rate for 5%, 10% and 15% H in Figs. 5.14 (d), 5.14 (e) and 5.14 (f), respectively. Looking at the relative viscosity values for the 5% H suspensions, higher relative viscosity was found for the samples with the highest aggregation indices (SN08A and EI02A). It can be noted that for the 5% H suspensions a slightly higher R^2 was found for both models

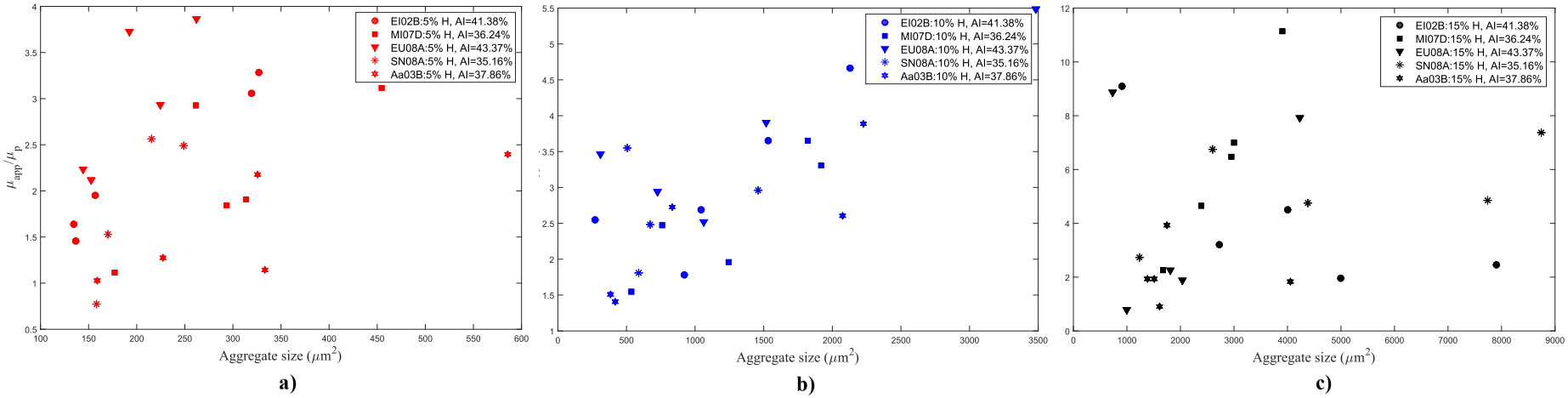

Figure 5.15: Relative viscosity measurement for five different human blood samples suspended at (a) 5% (b) 10% and (c) 15% H as a function of average aggregate size at 37°C. The AI is also provided for each sample.

(R^2 = 0.616 and R^2 = 0.646 for Power law and Carreau models respectively). This clearly indicates a smaller unexpected variation of the relative viscosity. The adjusted coefficient of determination was found to be $R^2_{adjusted} = 0.598$ for the Power law model as reported in Table 5.6. The RMSE for the Carreau model was found to be $0.5078 \times \mu_p$ as reported in Table 5.7.

For the 10% H suspensions, the Power law and Carreau models explain slightly better the variation of the relative viscosity since the R^2 was again found to be slightly higher ($R^2 = 0.747$ and $R^2 = 0.676$ for Power law and Carreau models respectively). The RMSE for the Carreau model was found to be 0.617 as reported in Table 5.7 and $R^2_{adjusted} =$ 0.736 for the Power law model as reported in Table 5.6. Here, higher relative viscosities are associated with the samples with higher aggregation indices as it was found for the 5% H suspensions.

For the 15% H suspensions, the relative viscosity variation is not well represented by the Power law model considering the very small R^2 (R^2 = 0.216). The coefficient of determination for the Carreau model was found to be slightly higher (R^2 = 0.419). However, a relatively large RMSE value was found (RMSE= $2.34 \times \mu_p$). The relative viscosity data for 15% H are not well represented by either non-Newtonian models.

The relative viscosity is plotted as a function of the average aggregate sizes for 5%, 10% and 15% H in Figs. 5.15 (a), 5.15 (b) and 5.15 (c), respectively. The trend for the combined samples shows that an increase in the aggregate sizes appears to result in an increase in viscosity, although for the smallest aggregate sizes the relative viscosity is higher for some samples. In fact, an increase in aggregation does not translate into a linear increase of the blood viscosity as previously stated by Kaliviotis and Yianneskis [178]. This relationship could be due to differences in the structural integrity of the RBC network. For the 5% and 10% H, the samples with higher aggregation indices (SN08A and EI02B) showed higher viscosities for the same average aggregate sizes compared to the samples with lower AI. This clearly indicates that the samples with higher AI form a stronger network of aggregates that are more difficult to disaggregate, resulting in higher viscosity values. This phenomenon could be explained by a potential increase in fibrinogen concentration as shown in the study of Brust *et al.* [44]. Further investigation of the aggregates molecular interaction is required in order to interpret the results with

certitude. The rate of change of viscosity with the aggregate sizes does not only vary from sample to sample but also varies with the hematocrit. In fact, an increase in blood hematocrit results in an increase of the rate of variation of viscosity with the aggregate sizes.

5.3.2 Numerical simulations

5.3.2.1 Procedure

The procedure used to implement the cases for the numerical simulation was briefly described in Sections 3.1.7.3 and 4.1.2 and is further explained in the present section. The grids were constructed based on the microscopic images (from the μPIV) at the intersection and the middle of the microchannel (1300 μm from the intersection). The length of the microchannel was based on the design imprinted on the transparency photomask. An example of the channel mesh near the intersection is shown in Fig. 5.16. In order to efficiently solve for the interface between both fluids, elements are concentrated at the intersection and in the middle of the channel width. Each grid consists of 2260 and 1820 elements for the 5% and 10% H cases, respectively. The order of the highest Legendre polynomial, N, for the double Y-microchannel configuration was set to be $N = 6$ and was shown to provide a smooth solution within each element. Here, PBS is treated and solved as a Newtonian fluid with a viscosity measured using the m-VROC^{TM} viscometer (Rheosence Inc., USA). To simulate the blood viscosity, the Power law and Carreau models are used with the fitted parameters obtained previously. Specifically, inlet boundary conditions are prescribed at the entrance of both branches for the velocity and viscosity. The velocity is set as previously described in 4.1.2.1 with Eqs. (4.7) and (4.8) for both branches. For the PBS branch, the power law index is set as $n = 1$ (for a Newtonian fluid), while for blood n varies depending on the hematocrit as shown in Table 5.4. At the entrance of the channel branches, the fluids are assumed to enter with a constant viscosity. For the PBS, the viscosity value is converted from the experimental measured value using Eq. (4.18). For blood, the consistency index K and the viscosity at low shear rates μ_0 are used as viscosity values in the Power law and the Carreau models, respectively. No-slip boundary conditions are set at the walls of the microchannel, while a normal outflow boundary condition is set at both exit branches of the microchannel.

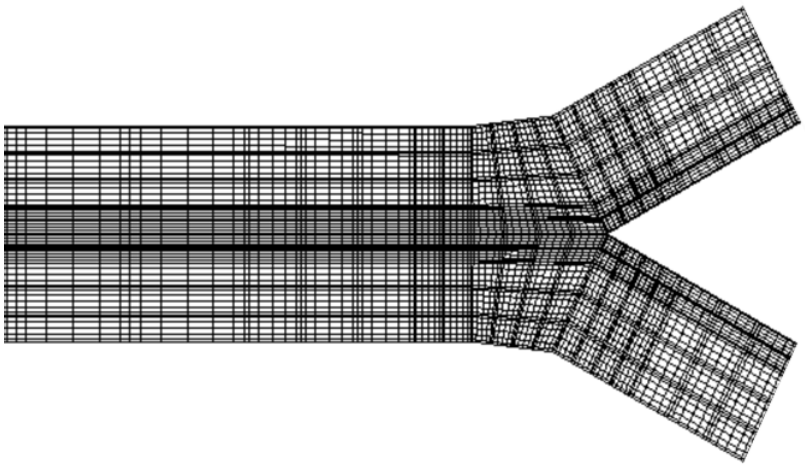

Figure 5.16: Microchannel Spectral Element grid for the numerical simulations. The grid consists of 2260 elements for the 5% H and 1820 elements for 10% H with 7 points in direction in each element (order of highest Legendre polynomial N= 6).

Initial conditions are set similarly to the boundary conditions in terms of velocity and viscosity. In order to solve properly for the interface between the both fluids in the channel, the viscosity used in the Navier-Stokes equations is solved by a passive scalar advection diffusion equation as described in Section 3.1.7.1, with Eq. (3.6). It is necessary to interpolate the viscosity in the channel and the diffusion layer as follows:

$$\mu_{sim} = \mu_{PBS} + (\mu_{blood} - \mu_{PBS})(\frac{\phi - \mu_{PBS}}{K - \mu_{PBS}}) \tag{5.8}$$

where μ_{sim} is the viscosity to be solved, μ_{PBS} is the viscosity of PBS in simulation units, μ_{blood} represents the blood viscosity using the specified non-Newtonian model in simulation units, ϕ is the value of the passive scalar found using Eq. (5.8) and K is the consistency index for the Power law model (μ_0 is used in Carreau model) in simulation units. The diffusion coefficient used between both fluids is set to mimic the diffusion coefficient between two miscible fluids, based on the value for glycerol and water obtained experimentally. This is a valid assumption, considering that the plasma and PBS are two miscible fluids.

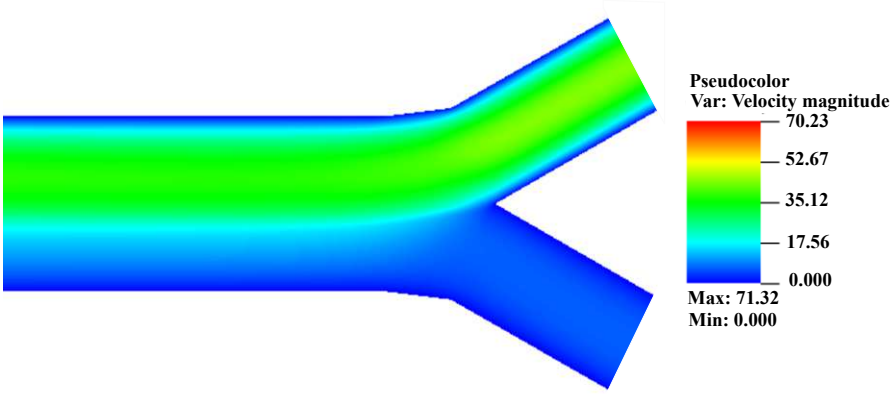

Figure 5.17: Numerical non-dimensional velocity magnitude distribution for blood flowing at 5% H with $Q = 20\ \frac{\mu L}{hr}$ using the Power law model at room temperature at $z = 0$. Blood flows in the bottom branch while PBS flows in the top branch. The velocity is normalized by the reference value $\frac{\mathcal{T}}{\mathcal{L}} = 50.16 \times 10^{-6}\ \frac{m}{s}$.

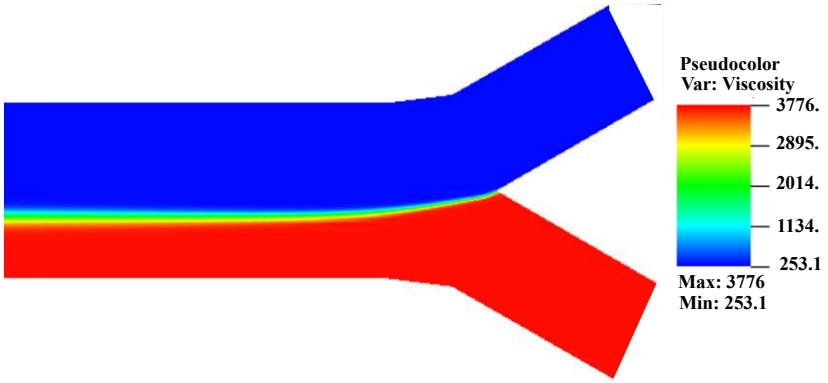

Figure 5.18: Numerical non-dimensional viscosity distribution for blood flowing at 5% H with $Q = 20\ \frac{\mu L}{hr}$ using the Power law model at room temperature at $z = 0$. Blood flows in the bottom branch while PBS flows in the top branch. The viscosity is normalized by the reference value $\frac{\mathcal{LT}}{\mathcal{M}} = 2.5 \times 10^{-6}\ Pa.s$.

5.3.2.2 Comparison between simulations and experiments

The simulations were performed to replicate the experiments at room and body temperature. At room temperature, the simulation was performed using the Power law model for blood at 5% H (using the fitted parameters obtained in Table 5.1) and a flow rate of $Q = 7.5\ \frac{\mu L}{hr}$. Figures 5.17 and 5.18 show the velocity and viscosity distributions respectively in the mid-plane of the microchannel depth. The velocity profile was extracted at 1800 μm from the intersection of both branches and compared to the experimental velocity profile extracted at the same location in the channel for sample Aa03A at 5% H

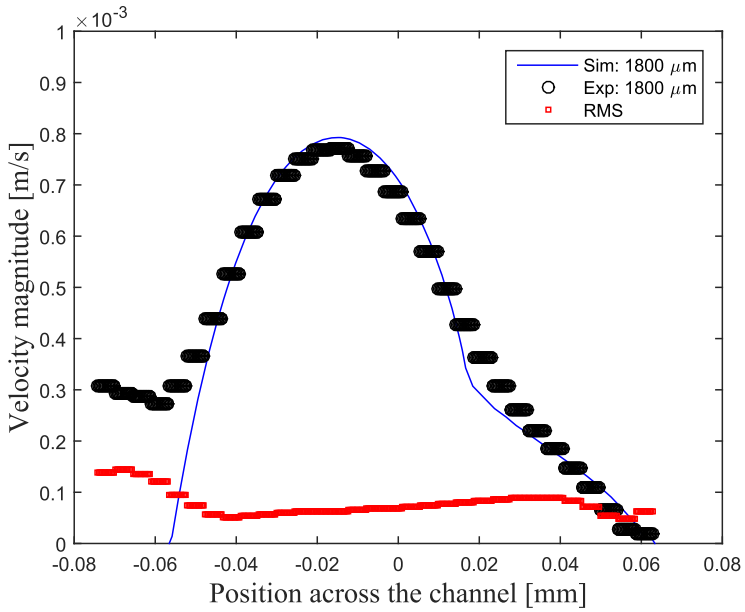

Figure 5.19: Numerical velocity profile using the Power law model (blue curve) at 5% H (Table 5.1) compared to the experimental velocity profile (black data points) for human blood at 5% H (Aa03A) flowing at $Q = 7.5\ \frac{\mu L}{hr}$ at room temperature. The red data points show the RMS of the experimental velocity profile.

in Fig. 5.19. The RMS of the experimental velocity profile is also provided in Fig. 5.19 and shows a very small standard deviation. Very good agreement was found between the simulation and experiment which added confidence to the experimental findings. This similitude between the simulations and experiments is due to the goodness of the fit for the samples used since the simulation grids and inlet boundary conditions were replicated from the specific sample experiment.

At body temperature, the simulations were performed using the Power law and Carreau models for blood at 5% and 10% H (using the fitted parameters obtained in Tables 5.4 and 5.5) and flow rates of $Q = 20\ \frac{\mu L}{hr}$ and $Q = 7.5\ \frac{\mu L}{hr}$. The profiles were extracted at two different locations in the channel, matching the experimental ones. Figure 5.20 compares the numerical simulations performed with the Power law and Carreau models (green and blue curves respectively) to the experimental velocity profile (SN08A) for 5% H flowing at $Q = 20\ \frac{\mu L}{hr}$ at (a) $x = 140\ \mu m$ and (b) $x = 1300\ \mu m$ from the intersection. Again, good agreement was found between the simulation and experiment, especially with the Carreau model. Figure 5.21 compares the numerical simulations performed with the Carreau model (blue curve) to the experimental velocity profile (SN08A) for

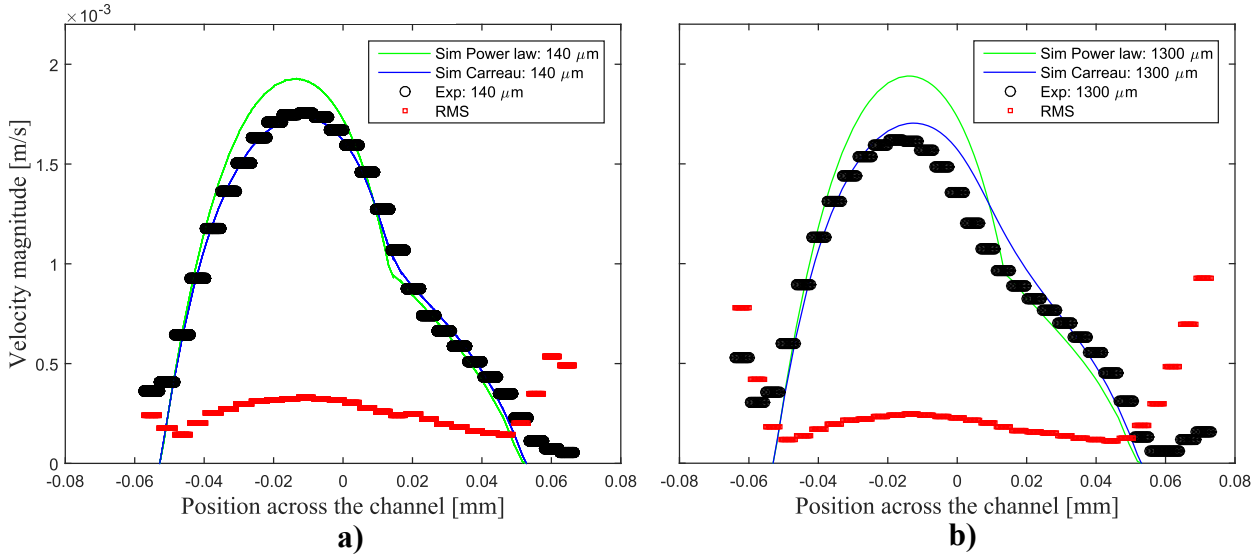

Figure 5.20: Numerical velocity profiles at (a) $x = 140\ \mu m$ and (b) $x = 1300\ \mu m$ from the intersection, using the Power law model (green curve) and the Carreau model (blue curve) at 5% H (using parameters from Tables 5.4 and 5.5 respectively) compared to the experimental velocity profiles (SN08A) for human blood at 5% H flowing at $Q = 20\ \frac{\mu L}{hr}$ at $T = 37°C$. The red data points show the RMS of the experimental velocity profile.

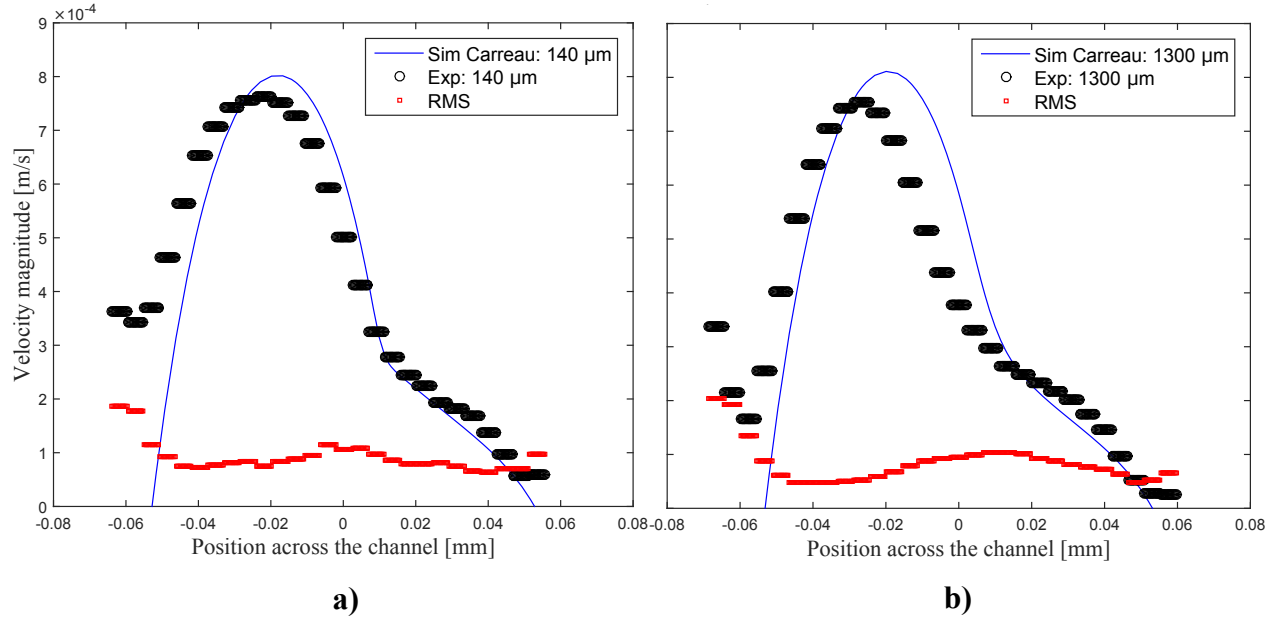

Figure 5.21: Numerical velocity profiles at (a) $x = 140\ \mu m$ and (b) $x = 1300\ \mu m$ from the intersection, using the Carreau model (blue curve) at 5% H (using parameters from Table 5.5 respectively) compared to the experimental velocity profile (SN08A) for human blood at 5% H flowing at $Q = 7.5\ \frac{\mu L}{hr}$ at $T = 37°C$. The red data points show the RMS of the experimental velocity profile.

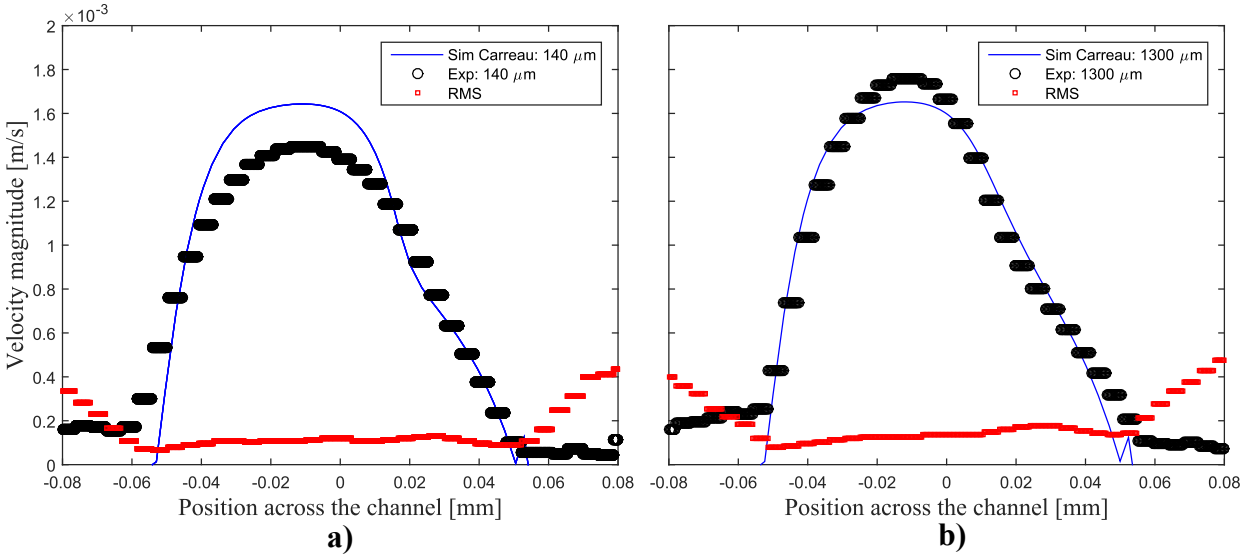

Figure 5.22: Numerical velocity profiles at (a) $x = 140\ \mu m$ and (b) $x = 1300\ \mu m$ from the intersection, using the Carreau model (blue curve) at 10% H (using parameters from Table 5.5) compared to the experimental velocity profiles (MI07D) for human blood at 10% H flowing at $Q = 20\ \frac{\mu L}{hr}$ at $T = 37°\text{C}$. The red data points show the RMS of the experimental velocity profile.

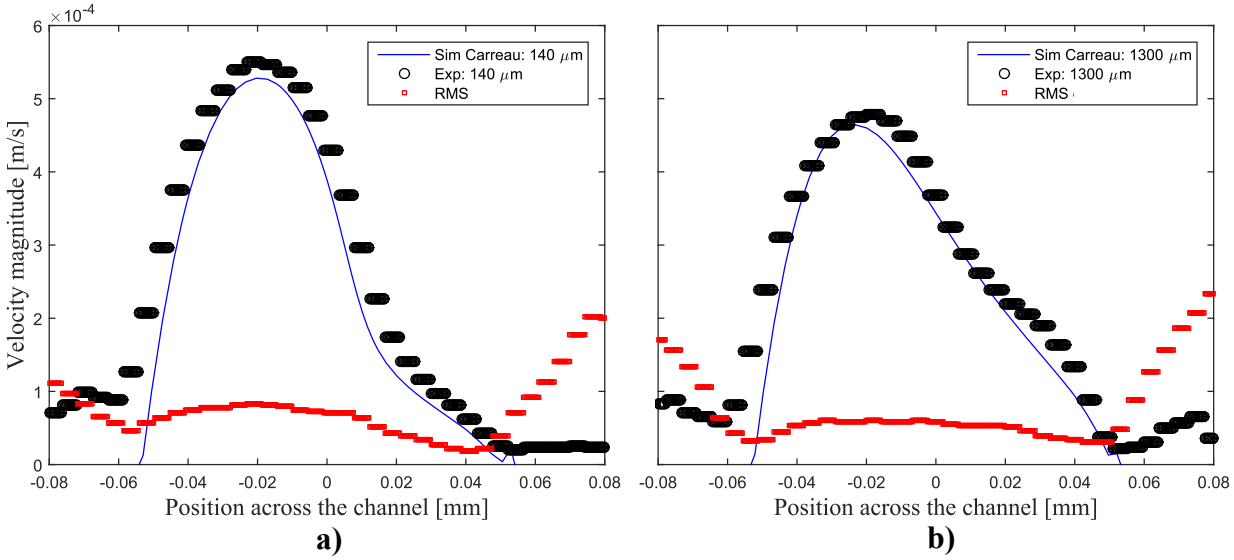

Figure 5.23: Numerical velocity profiles at (a) $x = 140\ \mu m$ and (b) $x = 1300\ \mu m$ from the intersection, using the Carreau model (blue curve) at 10% H (using parameters from Table 5.5) compared to the experimental velocity profiles (MI07D) for human blood at 10% H flowing at $Q = 7.5\ \frac{\mu L}{hr}$ at $T = 37°\text{C}$. The red data points show the RMS of the experimental velocity profile.

5% H flowing at $Q = 7.5\ \frac{\mu L}{hr}$ at (a) $x = 140\ \mu m$ and (b) $x = 1300\ \mu m$ from the intersection. Good agreement was found between the simulation and experimental velocity profiles. However, it is important to note that the experimental channel width is slightly larger than the channel width in the simulation, which can alter the flow conditions. In fact, it was found that a trapezoidal channel cross-section existed instead of a rectangular one, resulting from an imperfect fabrication process. Similar simulations were performed for blood at body temperature at 10% H at $Q = 20\ \frac{\mu L}{hr}$ and $Q = 7.5\ \frac{\mu L}{hr}$ as shown in Figs. 5.22 and 5.23 respectively at two different locations in the channel. Very good agreements between the simulations and experiments were found for all the cases, hence adding confidence to the experimental findings.

5.4 Summary

In this chapter, results for porcine and human blood were obtained using the previously described (Chapter 3) and validated methodology (Chapter 4). For human blood, the average RBC aggregate size and the viscosity were related quantitatively to the corresponding and measured shear rate for different hematocrits. A relationship was also determined between the viscosity and average aggregate size within the same microfluidic set-up. The blood viscosities for the different hematocrits were fitted with two empirical models, that were then used in the numerical simulations. Very good agreements between the numerical and experimental velocity profiles were found adding confidence to the experimental results. This study establishes validation of the implementation of such experimental results into numerical simulations for the modeling of blood accounting for RBC aggregation.

Chapter 6

Measurement Uncertainty and Influencing Factors

The work presented in this thesis provides a novel method for quantifying and characterizing RBC aggregation and a new experimental-based viscosity model for blood accounting for RBC aggregate behaviour in microcirculation. Inherent to experimental work, uncertainties and errors associated with the measurements must be quantified. In this chapter, we present the measurement uncertainties related to the experimental procedures, instruments and results. We also provide a summary of possible factors affecting the experiments and simulations and the solutions employed to remedy these possible issues.

6.1 Measurement uncertainty

Based on the experimental procedure, measurement errors can affect the RBC aggregation sizes, the shear rate and the apparent viscosity used in the experimental work. Errors affecting each of these factors are discussed in the following sections. Precision, δ_p, and bias errors, δ_b, were estimated in these sections as follows [179]:

$$\delta_p = \sqrt{\sum_{n=1}^{M} \left(\frac{\partial Meas}{\partial X_n} \delta_{p_n} \right)^2} \tag{6.1}$$

$$\delta_b = \sqrt{\sum_{n=1}^{M} \left(\frac{\partial Meas}{\partial X_n} \delta_{b_n} \right)^2} \tag{6.2}$$

where $Meas = f(X_1, X_2, ..., X_n)$ represents the quantity to be measured and $p_1, p_2, ...p_n$ and $b_1, b_2, ...b_n$ represent the corresponding precision and bias errors for parameters $X_1, X_2, ...X_n$ respectively. The total uncertainty of each measurement δ_T, combining the precision and the bias errors, is calculated as follows:

$$\delta_T = \sqrt{{\delta_p}^2 + {\delta_b}^2}. \tag{6.3}$$

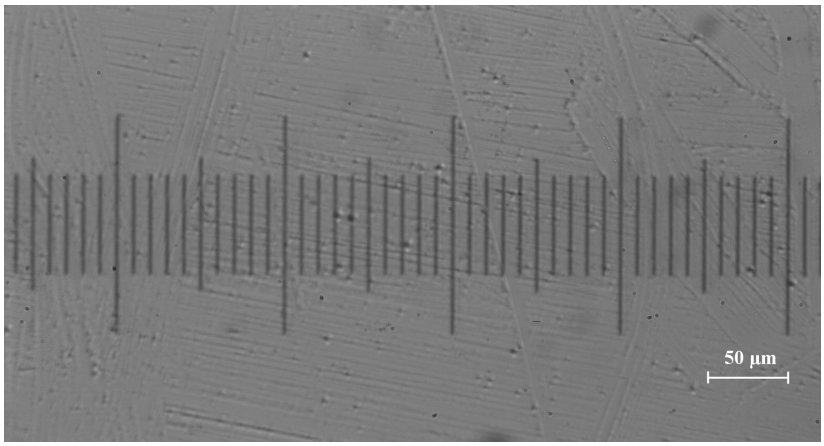

Figure 6.1: Image of the microscale recorded using the high speed camera under a 20X lens.

6.1.1 Aggregate size

Factors affecting the measurement uncertainties of the aggregate size include the measurement of the aggregates, in pixels, and the lens calibration for the size estimation. The lens calibration constitutes a bias error as it propagates and affects all the measurements in the same manner.

In order to estimate the precision error for the aggregate size measurements, the standard error calculated based on the different tests performed is used. The precision error was estimated for the different hematocrits as an average of all the samples, in percentage. For the 5% H suspensions, the average precision error was found to be $\delta_{5\%p} = 2.75\%$. Larger precision errors were found for the higher hematocrits. For the 10% and 15% H suspensions, the average errors were found to be $\delta_{10\%p} = 6.32\%$ and $\delta_{15\%p} = 7.62\%$, respectively. This again confirms that the results with higher hematocrits, specifically at 15% H, introduce higher uncertainties due to the difficulty of aggregate detection. The bias error was assumed to arise from the optics calibration and was estimated in the following manner. Figure 6.1 was used to convert the pixels in the image to micrometers. The smallest increment of the microscale is 10 μm, hence providing a distance of 100 μm between the two consecutive largest ticks. The number of pixels was measured between the largest ticks and was used as a scaling factor. However, the largest ticks had a thickness of 7 *pixels* in the image, hence providing a bias error of $\delta_b = 1.66\%$ error in the scaling factor. Using Eq. (6.3), the uncertainty of the aggregate size measurement, δ_T, combining the precision, δ_p, and the bias error, δ_b, was found to

be $\delta_{5\%} = 3.21\%$, $\delta_{10\%} = 6.53\%$ and $\delta_{15\%} = 7.79\%$ for the 5%, 10% and 15% H samples respectively.

6.1.2 Shear rate

Uncertainties in the shear rates measurements arise from errors in the μPIV measurements as well as the blood layer measurements. Errors affecting each of these factors are discussed below.

μPIV Errors affecting the velocity measurements performed include the DOC based on the particle sizes, the Brownian motion of the particles in the flow, the timing between the frames, the particle displacement and the camera calibration.

The DOC is affected by the presence of the particles and hence does not only depend on the fluorescent particle sizes. However, it is not possible to estimate precisely the extent of the effect of RBC on the DOC. Therefore, the proper and best pre-processing and processing method (comparing different existing methods) was used to minimize the effect of the RBC flow as discussed in Section 3.1.3. This effect was hence neglected as it was ensured that it does not contribute to the experimental uncertainties. The Brownian motion of the particles is known to be important especially in μPIV [112]. As a result, the velocity vectors are averaged for 100 frames, hence reducing the random motion of the particles in the flow. The standard deviation, resulting from the data averaging, was reported as the RMS and was used to calculate the experimental precision error as follows:

$$\delta_p = \frac{2 \times RMS}{\sqrt{100}}. \tag{6.4}$$

Using Eq. (6.4), the velocity vector averaging was found to contribute an average of 4.10% to the measurement uncertainty. This average value is affected by the large RMS velocity at the walls of the microchannel. In fact, near the microchannel walls, the cross-correlation is performed in the correlation window that includes particles inside the channel as well as the channel wall itself where no particles are present, hence increasing the error estimation. Another precision error that could occur during the correlation process is due to the mis-matching of particle images. The Specialist Committee on Uncertainty Analysis of the 25th ITTC [180] states that this precision is on the order

of 0.2 *pixels* which results in a maximum of 3% of the particle displacement. The timing interval between the two pulses was controlled by the timing unit which has an uncertainty of 5 ns according to the LaVision manual. Therefore, the total uncertainty in the time interval between two pulses was 10 ns. For the smallest time interval used, 2000 μs, the uncertainty was 0.0005% which was neglected in the combined uncertainties calculation. The camera calibration was performed as described in Section 6.1.1 where a bias error of 1.66% was estimated affecting all the measurements equally.

The total uncertainty combining the bias and precision errors for the velocity measurement was found to be on the order of 5.34%.

Blood layer Precision errors for the blood layer thickness were estimated to be the size of a fluorescent particle on both sides of the blood layer (wall and diffusion layer) of 2×2.85 *pixels*. This results in a precision limit of ± 1.58 μm resulting in an error of 3.82% for a blood layer thickness of 41.27 μm. Combining the bias error, resulting from the camera calibration and the precision error, the total uncertainty for the blood layer thickness measurement was estimated to be 4.17%.

Summary Combining the velocity and blood layer measurement uncertainties, the total combined uncertainty for the shear rate measurement was estimated to be 6.76%.

6.1.3 Apparent viscosity

Several factors can contribute to the errors in the viscosity measurements. These factors include the blood layer thickness, the microchannel width and the flow rate ratio between both branches. Here the camera calibration constitutes the bias error estimated to be 1.66% and propagates to affect equally the above mentioned measurements. The precision error arises from factors previously mentioned. The precision limit of the blood layer was estimated to be 4.17% in Section 6.1.2. The channel width was estimated in the same manner as for the blood layer and hence presents the same precision limit of $\pm$ 1.58 μm resulting in an error of 1.49% for a channel width of 108.02 μm. Combining the blood layer and the channel width uncertainties, uncertainty for the non-dimensional interface location Y in Eq. 3.3 was found to be 11.22%. Errors in the flow rate measurements were due to the velocity profile measurements and extrusion to 3D and were estimated to be

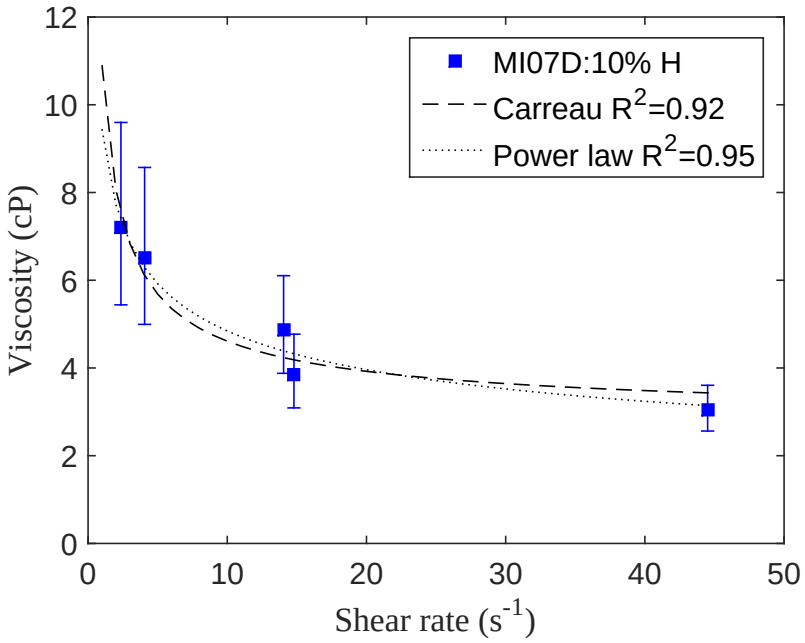

Figure 6.2: Apparent viscosity of human blood sample MI07D at 10% H at $T = 37°C$ with associated error bars translating the experimental uncertainty.

8.8%. The total error propagates and results in an absolute minimum error in viscosity of 0.29% and an absolute maximum error of 33.46%. Figure 6.2 shows the viscosity values for sample MI07D at 10% H with the associated error bars representing the maximum experimental uncertainty.

6.2 Influencing factors

6.2.1 Hematocrit variation

Although the hematocrit of the suspensions was measured and controlled before being injected into the microchannel, the hematocrit of the blood flowing in the field of view of the channel cannot be precisely controlled. As the blood is injected into the microchannel, it first passes through the tubes connecting the syringe to the microchannel, where blood is flowing downwards as shown in the experimental set-up in Fig. 3.1. This downwards flow may cause faster sedimentation of the blood in the tubes and in the inlet of the microchannel, which would affect the local hematocrit entering the blood branch. The use of native plasma, which promotes the natural RBC aggregation process, engenders

a faster sedimentation process. In order to avoid RBC sedimentation in the system, the blood was refilled in the syringes and the tubes every two minutes (approximately) and was refilled for each flow rate tested. Although all the necessary precautions were taken, a hematocrit difference was noted for the different cases tested supposedly under the same hematocrit (5%, 10% and 15%) under the microscope. In order to account for this difference, hematocrit was calculated from the microscopic images based on the aggregates detected in the microchannel. The estimated hematocrit $H_{estimated}$ is calculated as follows:

$$H_{estimated} = \frac{N_{RBC} \times V_{RBC}}{V_{blood\ layer}} \tag{6.5}$$

where V_{RBC} represents the volume of one RBC found to be 90 μm^3, the number of RBCs estimated in the images N_{RBC} is found using:

$$N_{RBC} = \sum_{n=1}^{n_{aggregates}} \frac{Aggregate\ size(n)}{Area_{1\ RBC}} \tag{6.6}$$

where $Area_{1\ RBC}$ is the area of one RBC and $V_{blood\ layer}$ is the volume of the blood layer:

$$V_{blood\ layer} = L_{field\ of\ view} \times h \times w_2 \tag{6.7}$$

where $L_{field\ of\ view}$ is the length of the field of view of the image, h is the depth of the microchannel, w_2 is the blood layer thickness in the microchannel. This method of hematocrit estimation, being solely dependent on the RBC images, cannot properly estimate the hematocrit for blood suspensions of 10% H or larger. The results are presented in Table 6.1 for the estimated hematocrit of the blood suspensions at 5% at $T = 23°C$ for five samples. Table 6.1 and Fig. 5.10 (a) (in Section 5.3.1.1) show that the highest hematocrit ($H_{estimated} = 9.8\%$) corresponds to the sample that shows the highest aggregate sizes (SE12A), which could explain the fact that the largest aggregates were found for an intermediate aggregation index ($AI = 35.49$). However, since the hematocrit is estimated based on the sizes of the aggregates detected, the estimated number of RBCs based on the RBC area and the blood layer thickness, the results are considered biased and hence will always agree with the average sizes found. Therefore, the estimated hematocrit values were not considered in this study since they do not represent a certain assessment of the hematocrit of the suspension. In order to reduce

Table 6.1: Estimated hematocrit based on microscopic images of the flow for five samples of human RBC suspensions at 5% H.

Sample -	$\dot{\gamma}$ (s^{-1})	$H_{estimated}$ (%)
SE12A	35.04	5.57
SE12A	24.89	4.52
SE12A	10.76	9.86
SE12A	7.56	9.59
SE12A	5.49	9.77
EI02A	37.83	5.30
EI02A	24.48	4.05
EI02A	18.00	5.02
EI02A	7.26	4.24
EI02A	4.37	2.02
Ao02A	34.52	1.98
Ao02A	26.77	2.05
Ao02A	12.81	2.25
Ao02A	15.50	2.33
Ao02A	3.93	5.05
EH06B	41.01	3.50
EH06B	19.23	3.04
EH06B	17.99	4.74
EH06B	13.65	4.26
EH06B	8.404	4.04
Aa03A	46.92	1.73
Aa03A	11.39	1.15
Aa03A	7.55	2.56
Aa03A	6.37	3.23
Aa03A	3.66	2.50

the effect of possible hematocrit variation in the channel, several tests $(2-5)$ were performed consecutively under the exact same conditions (30 seconds between tests). The results of the aggregate sizes were averaged for all the tests performed under the same conditions and the standard error between the tests was reported in Figs 5.10 and 5.13.

6.2.2 Shearing history

It is also known that different shearing histories of the blood suspensions affect blood behaviour and engender variations in aggregate behaviour under the same conditions [83]. Therefore, in order to provide the same shearing history for all the samples, the blood is injected in the channel at a flow rate of 250 $\frac{\mu L}{hr}$ and decreased gradually to 125, 60, 35, 20, 10, 7.5 and 5 $\frac{\mu L}{hr}$. The measurements were taken starting from $Q = 35$ $\frac{\mu L}{hr}$. This was done each time the syringe was refilled (to avoid RBC sedimentation in the tubes).

6.2.3 Effect of sample variation

The aggregates' behaviour at different hematocrit was successfully investigated and related to the corresponding shear rate in the blood layer. However, in order to relate the findings to previously existing aggregate measurement methods, the aggregation index measured for each sample was used to compare to the aggregate sizes obtained as shown in Section 5.3.1.2. It is important to note (as mentioned in Section 5.1) that the AI was measured (using the light transmission method) with whole blood (donor-specific hematocrit) kept at a constant temperature. The donor-specific hematocrit, changing from one individual to another, alters the aggregation curve shown in Fig. 1.5. In order to effectively compare the data, the aggregation index was measured in the same manner for all the samples and the whole blood hematocrit was also provided at body temperature.

In the previously discussed experiments, several samples were used and the measurements were combined to find a generic relationship for the viscosity and aggregate sizes as a function of the shear rate applied. Due to the different blood nature between samples, important variations of viscosity and aggregation sizes were found, as previously confirmed by Baskurt *et al.* [45, 48]. They showed the existence of a linear relationship

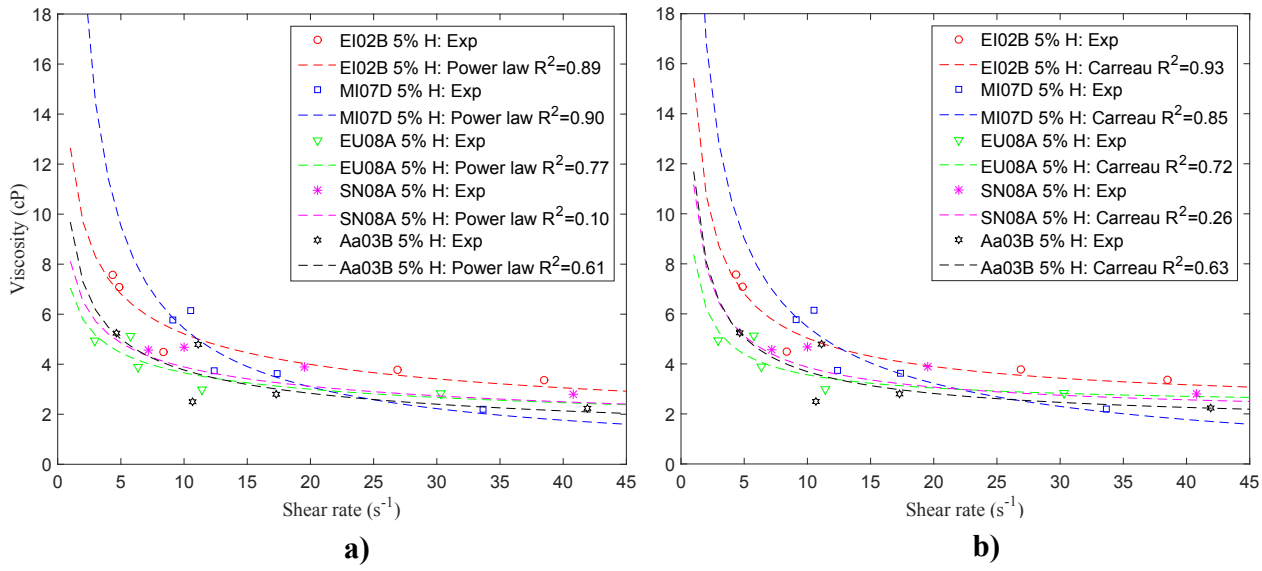

Figure 6.3: Apparent viscosity measurement as a function of shear rate for five different human blood samples suspended at 5% H at 37°C. Each sample is separately fitted with the Power law (a) and Carreau (b) models and shown with the associated R^2 value.

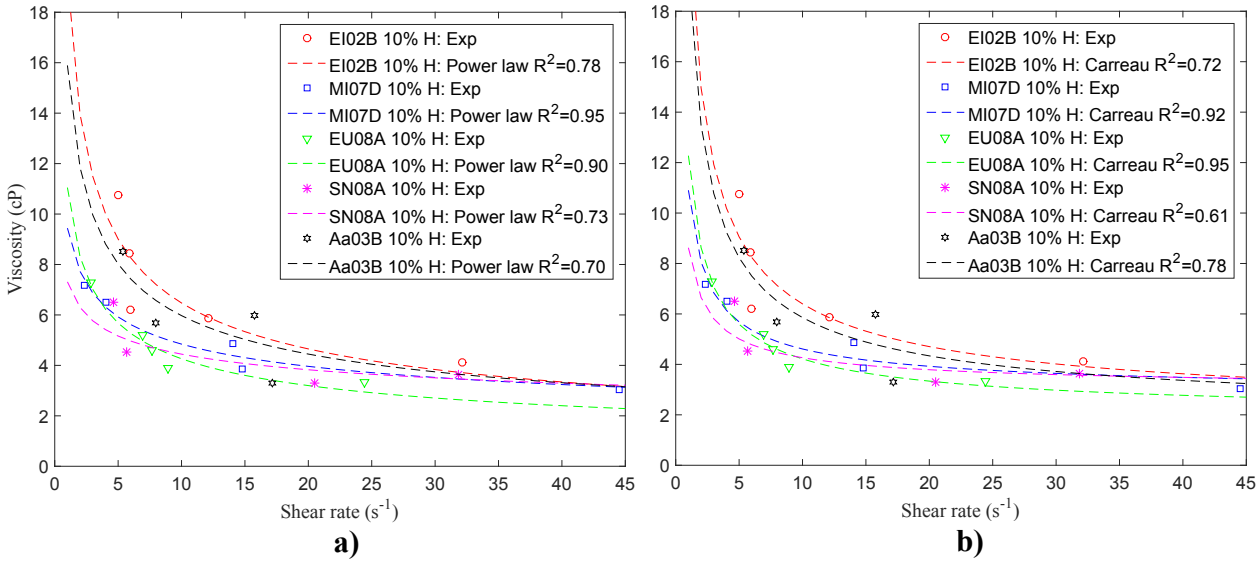

Figure 6.4: Apparent viscosity measurement as a function of the shear rate for five different human blood samples suspended at 10% H at 37°C. Each sample is separately fitted with the Power law (a) and Carreau (b) models and shown with the associated R^2 value.

between the aggregation index of blood in plasma and the aggregation index of blood in Dextran, hence showing an effect of the RBC properties (size, deformability, etc) on the aggregation mechanism. In order to investigate the behaviour of the different blood samples, the viscosity was fitted separately for each sample as shown in Figs. 6.3 (a) and 6.3 (b) for the samples suspended at 5% H using the Power law and Carreau models, respectively and in Figs. 6.4 (a) and 6.4 (b) for the samples suspended at 10% H using the Power law and Carreau models respectively. Here, the Power law and Carreau models provide a better representation of the individual samples as demonstrated by the curves fitted and the high R^2 values for both hematocrits. However, the viscosity data obtained were only provided for five shear rate values for each sample, which do not represent sufficient data to properly analyze the blood behaviour in microcirculation. Therefore, multiple samples were used to analyze RBC aggregates as previously shown in Section 5.3. The effect of the sample variation can also be seen when analyzing the non-Newtonian parameters currently used in the literature, reported in Table 5.4 [79, 177]. The Power law parameters obtained from viscosity measurements of two different studies (in 1991 and 2005) of human blood suspended at 45% H at $T = 37°C$ yielded different results under the same conditions.

The viscosity results obtained from all the samples were fitted to the two non-Newtonian models and the parameters were used in the numerical simulations, the results of which compared very well with the experiments. However, due the varying nature of blood and the different samples' behaviour, a further analysis of the numerical simulation results was performed. The sensitivity of the code to the non-Newtonian parameters used was tested by performing simulations using different Carreau parameters for the exact same case. The velocity profiles were then compared and analyzed. The tests performed and results obtained are detailed in Section 6.2.4.

6.2.4 Numerical simulation sensitivity to sample parameters

The results described in Section 5.3.2.2 show very good agreement of experimental and numerical velocity profiles. The numerical simulations were performed, however, with the experimental viscosity fitted models for all the samples. To assess the reliability of

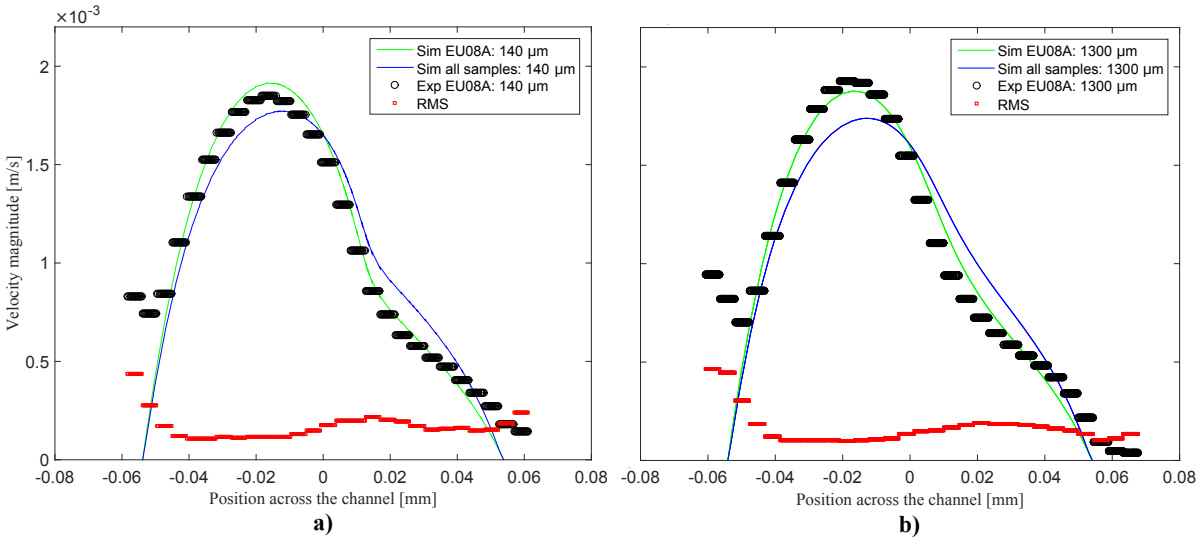

Figure 6.5: Numerical velocity profiles at (a) $x = 140\ \mu m$ and (b) $x = 1.3\ mm$ from the intersection, using the non-Newtonian parameters from human blood sample EU08A (green curve) and the non-Newtonian parameters from all the samples (blue curve) at 5% H compared to the experimental velocity profile (EU08A) for the 5% H flowing at $Q = 20\ \frac{\mu L}{hr}$ at $T = 37°\text{C}$. The red curve shows the RMS of the experimental velocity profile.

those findings, we investigated the sensitivity of the numerical simulations to the non-Newtonian parameters used to calculate the viscosity in the blood layer. In order to achieve this task, the non-Newtonian parameters obtained from the fitted viscosity data of sample EU08A using a Carreau model with a coefficient of determination $R^2 = 0.72$ were used. The numerical simulations were conducted to mimic the experimental conditions of sample EU08A at 5% H flowing at $Q = 20\ \frac{\mu L}{hr}$. The experimental velocity profiles at $x = 140\ \mu m$ and $x = 1300\ \mu m$ from the intersection were compared to the numerical simulations performed with the non-Newtonian parameters obtained for sample EU08A and for all the samples (Section 5.3.2.2), as shown in Fig. 6.5. Although using non-Newtonian Carreau parameters from all the samples combined offers a good agreement with the experimental results, mimicking the experimental conditions of the specific sample significantly improves the agreement with the experimental velocity profiles at the two different locations, as expected. This proves that the numerical results are influenced by the experimental case being simulated.

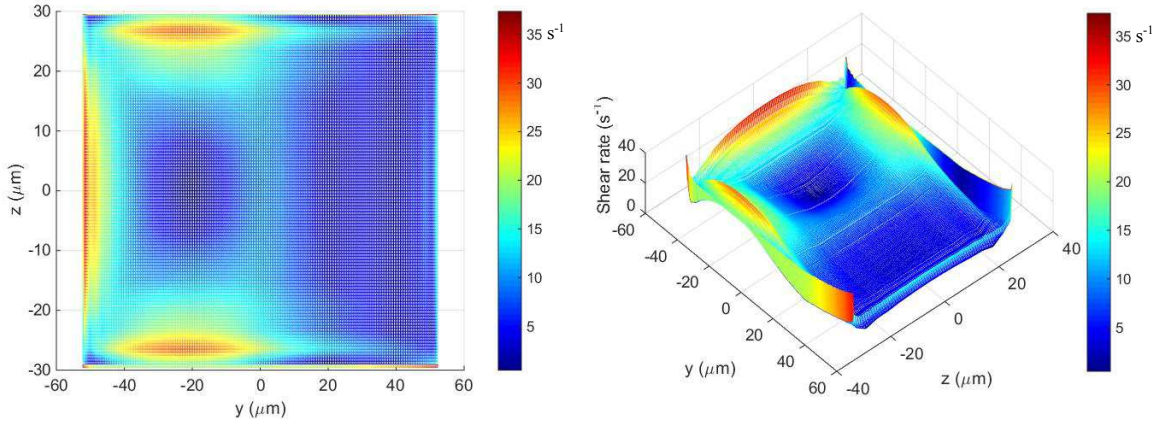

Figure 6.6: Numerical shear rate distribution for human RBCs flowing at 10% H at a flow rate of $Q = 7.5\ \frac{\mu L}{hr}$ within the microchannel cross-section at $x = 1300\ \mu m$ from the intersection in (a) 2D and in (b) 3D.

6.2.5 Three dimensional shear rate

The design of the microfluidic device was previously verified experimentally and numerically by Mehri *et al.* [19], using mid-plane results to provide a constant shear rate within the blood layer under certain conditions. However, due to the microchannel confinement, the shear rate varies considerably at the microchannel walls, where the cell free layer is formed, due to the no-slip boundary assumption on the channel walls. Gliah *et al.* [181] showed that the CFL thickness augments with diminishing flow rate in the channel. Considering the low flow rates and shear rates used in this study, the CFL thickness is expected to be significant in comparison to the blood layer thickness. In order to analyze the confinement effect on the 3D shear rate distribution, results from the numerical simulations were used. The shear rate was analyzed for the case of RBCs flowing at 10% H at a flow rate of 7.5 $\frac{\mu L}{hr}$. Figures 6.6 (a) and 6.6 (b) show the two-dimensional and three-dimensional shear rate distributions in the entire microchannel cross-section at $x = 1300\ \mu m$ from the intersection. Figure 6.7 represents the shear rate across the microchannel width (y-direction) for several z-planes, varying from $-30\ \mu m$ (microchannel wall) to $0\ \mu m$ (mid-plane). The blood layer (right side) is delimited as shown in Fig. 6.7 at $y = 12.54\ \mu m$. Differences in the shear rate within the blood layer become significant starting from a z-plane $5\ \mu m$ away from the microchannel wall. To

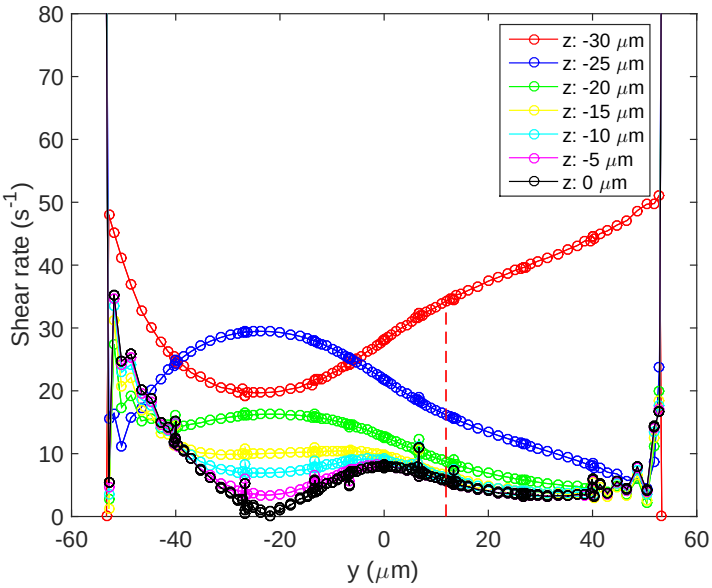

Figure 6.7: Numerical shear rate distribution across the microchannel width for several z-planes, varying from $-30\ \mu m$ (microchannel wall) to $0\ \mu m$ (mid-plane) for the microchannel cross-section at $x = 1300\ \mu m$ from the intersection. The blood layer (right side) is delimited by the red dashed line at $y = 12.54\ \mu m$.

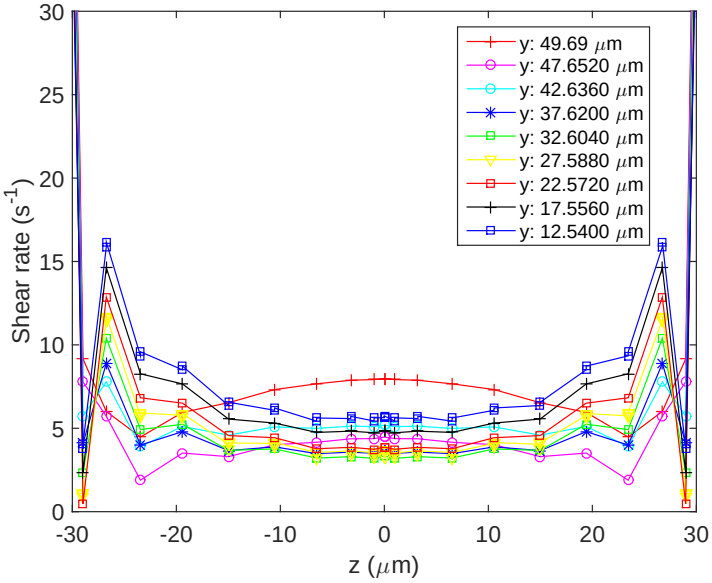

Figure 6.8: Numerical shear rate distribution across the microchannel depth for several y-planes, varying from 49.69 μm (near the channel wall) to 12.5 μm (middle of the diffusion layer) for the microchannel cross-section at $x = 1300\ \mu m$ from the intersection.

further investigate the shear rate distribution, the shear rate across the microchannel depth (z-direction) is shown for several y-planes starting near the microchannel wall and progressing towards the middle of the diffusion layer at $y = 12.54\ \mu m$ (Fig. 6.8). The shear rate was also found to be more constant further from the microchannel walls, as for the experimental findings. However, larger shear rates were found at the diffusion layer $y = 12.54\ \mu m$. Comparing the numerical three-dimensional shear rate to that of the experimental findings, the shear rate variation was quantified. A variation of 0.45% to 23% was found relative to the experimental shear rate value within the microchannel (5 μm away from the wall). These numbers confirm that away from the channel walls, the shear rate is fairly constant within the blood layer. The high shear rate near the channel walls corresponds to the location of the CFL where no RBCs are found. The shear rate in the microchannel mid-plane ($z = 0\ \mu m$) was calculated in the same manner as experimentally (Section 3.1.4) from the numerical velocity profile in the blood layer. The shear rate was found to be about 3.93 s^{-1}, which indicates a 3.1% difference relative to the experimental value.

6.2.6 Confinement effects on the RBC aggregates and apparent blood viscosity

The viscosity of blood is known to vary with vessel diameter [2, 65]. The formation of the RBC aggregates is therefore believed to be influenced by the microchannel size. In order to test the confinement effect on the RBC aggregate sizes, the same blood sample, suspended at two different hematocrits (5% and 10% H), was tested in two different microchannel sizes ($110 \times 60\ \mu m$ and $180 \times 53\ \mu m$) under the same conditions (velocity ratio and shear rates). In order to compare the channel sizes efficiently, the hydraulic diameter of the blood layer was calculated as follows, based on the estimation of the blood layer thickness:

$$D_H = \frac{4A}{Pe} \tag{6.8}$$

where A represents the rectangular cross-sectional area of the blood layer in the microchannel and Pe represents the perimeter of the blood layer rectangular cross-section. For the smaller microchannel size ($110 \times 60\ \mu m$), the hydraulic diameter was found to vary between 31 and 53 μm, while, for the larger microchannel ($180 \times 53\ \mu m$) the

hydraulic diameter was found to vary between 37 and 69 μm.

Figures 6.9 (a) and 6.9 (b) show average RBC aggregate sizes tested in two different channel sizes (110×60 μm and 180×53 μm) for 5 % and 10% H respectively. Figure 6.9 (a) shows slightly larger aggregate sizes for the smaller channel size, especially for high shear rates (difference of about 20 μm^2). However, for 10% H (Fig. 6.9 (b)), larger discrepancies exist: a difference of about 200 μm^2 was found where larger aggregates were associated with the smaller microchannel. To further investigate the discrepancies found, the apparent viscosity was also measured (using the optical viscometer method) in the two channel sizes (110×60 μm and 180×53 μm) for 5 % and 10% H in Figs. 6.10 (a) and 6.10 (b), respectively.

The viscosity obtained agrees with the aggregation size measurements. The apparent viscosity of blood at 5% H measured for both microchannels did not differ at low shear rates (0.7% difference within the smaller channel size at 9 s^{-1}). However, for 10% H (Fig. 6.10 (b)) different viscosity values were found for the two different channel sizes. For a shear rate of approximately 27 s^{-1} the viscosity of blood in the smaller channel was found to be higher than the viscosity of blood in the larger channel with a difference of 48% relative to the smaller channel size. A 13% difference in the hydraulic diameter may explain the viscosity difference.

Based on the present comparison between two microchannel sizes, a confinement effect does seem to exist and hence could influence the experimental data. The smaller microchannel size (used for this work) better represents the confinement found in microcirculation and hence better mimics blood behaviour at that scale. Also, RBC aggregates are free to form in 3D since the smaller microchannel offers less of a constraint on the aggregate formation due to the larger microchannel depth.

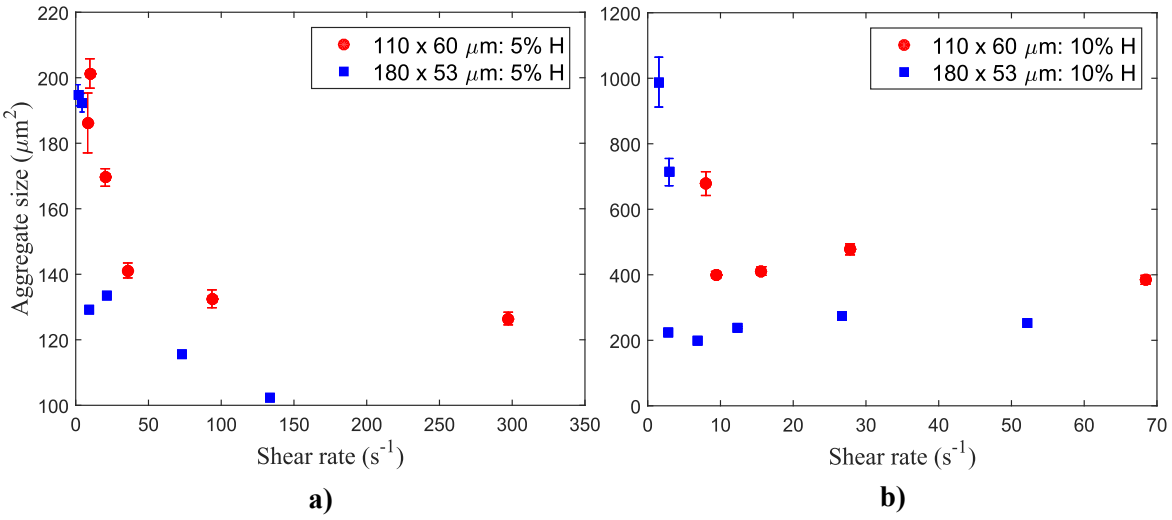

Figure 6.9: Average human RBC aggregate size as a function of the corresponding shear rate for the RBC suspensions at (a) 5% H and (b) 10% H in 110×60 μm (red) and 180×53 μm (blue) microchannels at room temperature.

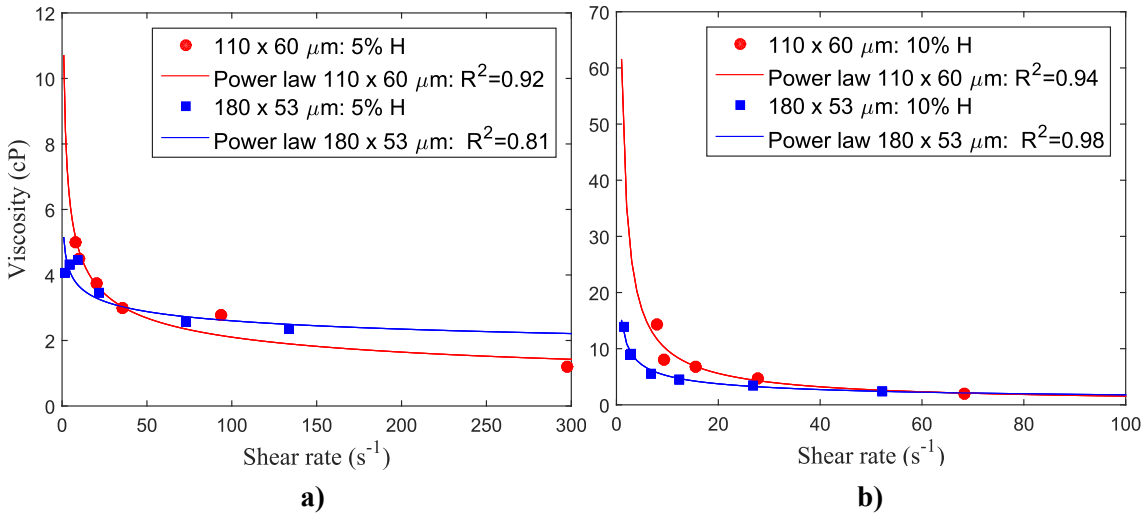

Figure 6.10: Apparent human blood viscosity as a function of the corresponding shear rate for the RBC suspensions at (a) 5% H and (b) 10% H in 110×60 μm (red) and 180×53 μm (blue) microchannels, temperature, fitted using the Power law (red and blue solid lines respectively). The corresponding R^2 values are also provided for both channels sizes.

Chapter 7

Conclusions and Recommendations

7.1 Summary of results

This research investigated blood behaviour in a controlled microfluidic system, under different conditions at different hematocrits. Within this microfluidic system, blood suspensions were entrained using a solution of PBS flowing faster in the microchannel. Measurements of blood behaviour were performed in a PDMS microchannel, fabricated in the laboratory with an approximate cross-section of $110 \times 60\ \mu m$. Velocity measurements were performed using a micro particle image velocimetry system to determine the shear rate within the blood layer. Aggregate sizes were determined based on the microscopic images of the RBC flow in the microchannel, using image processing techniques. Blood apparent viscosity was measured using the theory of optical viscometers based on the analytical solution of two co-flowing laminar, miscible fluids in a rectangular channel. The measurements were performed for porcine and human blood for different hematocrits under different conditions. Porcine blood suspended at 5, 10 and 15% H was tested at room temperature with flow rates in the channel of $Q = 10$ and $5\ \frac{\mu L}{hr}$. Human blood suspended at 5, 10 and 15% H was tested at room and body temperatures with flow rates in the channel of $Q = 35$, 20, 10, 7.5 and $5\ \frac{\mu L}{hr}$. The temperature was controlled via a heating lamp and a thermocouple positioned at the exit of the channel to avoid flow disturbances. Six samples (from six different individuals) were used for the tests performed at room temperature, while five samples were used for the tests performed at body temperature.

From this work, a systematic methodology was developed for the characterization of RBC aggregates in a controlled microfluidic environment providing controlled and measurable shear rates. A code for aggregate size detection based on microscopic images was developed and validated using two different methods. Known particle size ranges, injected in a PDMS microchannel, were measured using the developed code and compared to the manufacturer product sheet for those particles. A similar particle size distribution

was found. The code was also validated by comparing the results of the aggregate sizes obtained to those measured by hand (results of two researchers).

Porcine blood measurements provided quantitative results of the RBC aggregate sizes in a controlled microfluidic environment as a function of the corressponding shear rates. The effect of shear rate and hematocrit were quantified for porcine blood. These measurements also represent a proof of concept for the methodology developed.

Human RBC aggregate sizes were plotted as a function of the corresponding shear rates and were analysed for different hematocrits at room temperature. It was found that, for all the samples suspended at 5% H, varying the shear rate did not result in a significant increase of the aggregate sizes, which is in agreement with the findings of Kim *et al.* [46, 47]. Whereas, for the 10% H suspensions, lowering the shear rate below 10 s^{-1} resulted in a significant increase of the RBC aggregate sizes. The same trends were obtained at higher temperatures, however, with smaller aggregate sizes for all the hematocrits, thus providing quantitative results of the temperature effect on the RBC aggregate sizes. These results confirm the conclusions of Neumann *et al.* [52].

Apparent viscosity and the resultant relative viscosities were plotted as a function of the corresponding shear rates and were analyzed for the different hematocrits. Higher viscosities were found for higher hematocrits, as expected. Viscosity was found to increase with decreasing shear rate, showing the non-Newtonian shear-thinning behaviour of blood. However, the different samples used, showing different non-Newtonian behaviours, produced significant variations in viscosity, predominantly for the 5% H suspensions. Less variations were found between the samples for the relative viscosity since it takes into account the donor's plasma (suspending medium) viscosity. Higher viscosities were recorded for samples with higher aggregation indices (AI). Brust *et al.* [44] found that samples with higher AI form a stronger network of aggregates that are more difficult to disaggregate resulting in higher viscosity values due to the potential increase in fibrinogen concentration. The viscosity data were fitted with two empirical models previously developed to analyze the non-Newtonian behaviour of polymers: the Power law model and Carreau model. The non-Newtonian parameters associated with these models through fitting of the experimental data were used for further analysis of the experimental results.

Numerical simulations were performed replicating the experimental case, using the non-Newtonian parameters from both models. The non-Newtonian capabilities of the code were first validated using a power law fluid (POLYOX^{TM} WSR 301) experimentally in a double Y-microchannel configuration. An excellent agreement was found between the experiments and numerical simulations, showing the proper implementation of the non-Newtonian case. The numerical simulations were performed for the samples suspended at 5% and 10% H flowing at $Q = 20\ \frac{\mu L}{hr}$ and $Q = 7.5\ \frac{\mu L}{hr}$ for both hematocrits. The velocity profiles were extracted at two different locations in the microchannel (140 μm and 1.3 mm from the intersection) matching the experimental locations visualized. The numerical velocity profiles compared very well with the experimental μPIV data for the specific samples, hence confirming the experimental findings.

7.2 Summary of contributions

This work provides important contributions to the understanding of blood behaviour in microcirculation and the hemorheology field. The major accomplishments follow:

1. A novel methodology and procedure were developed to detect and analyze RBC aggregates in controlled conditions with controlled and measurable shear rates. This work was published in the Journal of Visualized Experiments in 2015 [170].

2. Porcine RBC aggregate sizes were analyzed in the controlled microcfluidic environment, which provided a proof of concept for the procedure developed. This work was published in the Journal of Medical and Biomedical Engineering in 2014 [173].

3. The results obtained for human blood constitute a major finding in the hemorheology research field as they fill a gap in the literature, providing better understanding of human RBC aggregates in microcirculation:

    (a) For the first time, a direct relationship between human RBC aggregate sizes and the applied shear rate was established and analyzed under several conditions (varying flow rate, hematocrit and temperature) via a controlled microfluidic shearing system.

(b) Within the same environment, viscosities of flowing human RBC aggregate suspensions were measured and related to the corresponding shear rate. Consequently a relationship between RBC aggregate sizes and viscosity was found and established for several hematocrits.

(c) The results obtained at room temperature constitute a framework for the design of lab-on-chip devices and artificial organs on chips.

(d) Numerical blood viscosity models that incorporate human RBC aggregation behaviour, as measured from experiments at body temperature, were developed and shown to be reliable in predicting low hematocrit blood flow in microchannels.

4. The non-Newtonian implementation in the CFD software verified experimentally (mimicking experiments performed with a Power law fluid (POLYOX^{TM}) in a Y-microchannel entrained by deionized water flowing at 10 $\frac{\mu L}{hr}$) constitutes another contribution, ensuring the proper implementation of the non-Newtonian cases and the proper resolution of viscosities between the Newtonian and non-Newtonian fluids at the interface. This work provides a framework for simulations of flows of RBC suspensions, exhibiting very good agreement between simulations and experiments.

7.3 Recommendations for future work

As previously mentioned, this work has some limitations as is inherent to experimental work. These possible factors influencing the results were discussed in Section 6.2.2, together with the solutions employed to remedy these possible issues. However, one major limitation remains persistent and should be the subject of future work. Using the methodology described in this thesis, higher hematocrits cannot be easily visualized in this microfluidic environment due to the superposition of the aggregates in the image and the microchannel confinement. In fact, difficulties were encountered in the visualization of the aggregates in the microchannel at 15% H. Therefore, analyzing blood behaviour at higher hematocrits (reaching up to 20% H in microcirculation [182]) would require further investigation. Decreasing the microchannel depth could remedy this situation. However, this could alter the formation of the RBC aggregates in two ways: 1) it will

result in a 2D formation of the aggregates as they will be constrained in the z-direction and 2) the effect of the shear rate at the microchannel walls could dominate, eliminating the constant distribution in the blood layer. For future work, we suggest exploring the use of a confocal microscope coupled to the μPIV system and the high speed camera with the same methodology described to analyze the RBC aggregates. A confocal microscope could provide information on 3D aggregate formation and hence provide a better visualization with higher hematocrits up to 20% (the hematocrit value in human microcirculation).

The RBC aggregates were successfully analyzed in the controlled microfluidic environment of a straight channel with a rectangular cross-section. Future work can extend this study to anatomically correct microchannel geometries (as shown in Figs. 7.1 and 7.2 with a rectangular cross-section) where different shear rate distributions are expected across the channel width. In order to test the feasibility of such a study, preliminary work was performed to fabricate the microchannels and to generate suitable numerical grids. The geometries shown in Figs. 7.1 and 7.2 were created based on real microcirculation networks extracted from veins and arteries of the human retina and capillaries of a cat mesentery [182]. In order to create these geometries in CAD files, several points across the centreline of the channel were selected and a spline was calculated across their offset by the width of the channel to obtain the points across the boundaries. The channels were fabricated using the standard photolithography methods as described in Section 3.1.6. An elliptic grid generator was created in order to generate suitable spectral element grids for these complex microchannels configurations [183]. To obtain realistic channel boundaries, a spline interpolation, based on the channel length, was used between the reference points. A uniform distribution of the points was ensured by linearly approximating the distance between the reference points, while the boundary points were determined based on the channel length. If a non-uniform distribution is required, grid refinement can be used in those areas. The grid generator developed creates a mesh for each daughter branch bifurcating from the mother branch, with a smooth transition between the two. This ensures better control of the grid for each branch. The 3D mesh was generated based on the 2D mesh by extruding it in the third direction. Due to the curvilinear nature of the boundaries created, the collocation points were not

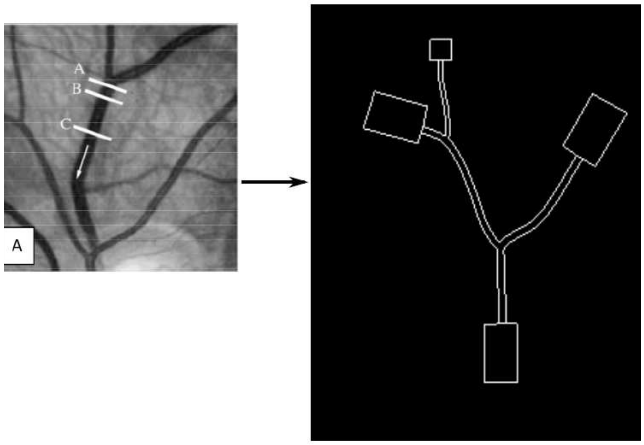

a) b)

Figure 7.1: (a) Image of veins and arteries of the human retina [182] and (b) corresponding channel created using a CAD program.

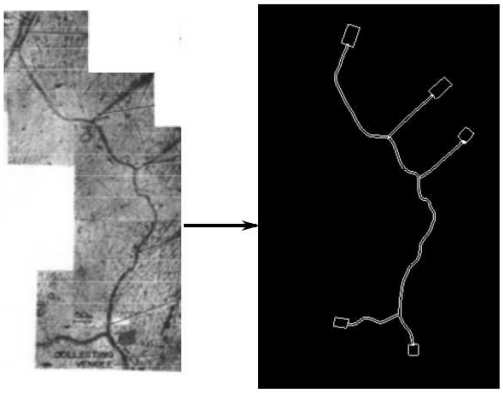

a) b)

Figure 7.2: (a) Image of capillaries of a cat mesentery [182] and (b) corresponding channel created using a CAD program.

generated automatically but were provided to the solver as known parameters. The collocation points were distributed based on the arc length of each element. Preliminary simulations in the generated grids with varying viscosities have been successfully tested [183]. Comparison of the experimental flows and the numerical simulations for these more anatomically realistic geometries will provide further understanding of the RBC behaviour in microcirculation networks.

As a further improvement, thereafter, round cross-section microchannels, mimicking more closely the microcirculation, should be used to compare simulated and *in vitro* flows of RBC aggregates to *in vivo* studies.

References

[1] J. J. Bishop, A. S. Popel, M. Intaglietta, and P. C. Johnson. Rheological effects of red blood cell aggregation in the venous network: a review of recent studies. *Biorheology*, 38(2-3):263–274, 2001.

[2] A. R. Pries, D. Neuhaus, and P. Gaehtgens. Blood viscosity in tube flow: dependence on diameter and hematocrit. *The American Journal of Physiology*, 263(6 Pt 2):H1770–8, 1992.

[3] G R Cokelet. Rheology and hemodynamics. *Annual Review of Physiology*, 42(1):311–322, 1980.

[4] H. Schmid-Schönbein, E. Volger, and H. J. Klose. Microrheology and light transmission of blood. *Pflügers Archiv European Journal of Physiology*, 333:140–155, 1972.

[5] H. Schmid-Schönbein, P. Gaehtgens, and H. Hirsch. On the shear rate dependence of red cell aggregation *in vitro*. *The Journal of Clinical Investigation*, 47(6):1447–1454, 1968.

[6] R. M. Bauersachs, R. B. Wenby, and H. J. Meiselman. Determination of specific red blood cell aggregation indices via an automated system. *Clinical Hemorheology*, 9(1):1–25, 1989.

[7] M. R. Hardeman, J. G. Dobbe, and C. Ince. The laser-assisted optical rotational cell analyzer (LORCA) as red blood cell aggregometer. *Clinical Hemorheology and Microcirculation*, 25(1):1–11, 2001.

[8] E. Kaliviotis, J. Dusting, and S. Balabani. Spatial variation of blood viscosity: Modelling using shear fields measured by a μPIV based technique. *Medical Engineering & Physics*, 33(7):824 – 831, 2011.

[9] J. Dusting, E. Kaliviotis, S. Balabani, and M. Yianneskis. Coupled human erythrocyte velocity field and aggregation measurements at physiological haematocrit levels. *Journal of Biomechanics*, 42(10):1438 – 1443, 2009.

[10] J. M. Sherwood, E. Kaliviotis, J. Dusting, and S. Balabani. Hematocrit, viscosity and velocity distributions of aggregating and non-aggregating blood in a bifurcating microchannel. *Biomechanics and Modeling in Mechanobiology*, 13(2):259–273, 2014.

[11] S. Chen, G. Barshtein, B. Gavish, Y. Mahler, and S. Yedgar. Monitoring of red blood cell aggregability in a flow-chamber by computerized image analysis. *Clinical Hemorehology*, 14(4):497–508, 1994.

[12] Y. Liu and Wing K. Liu. Rheology of red blood cell aggregation by computer simulation. *Journal of Computational Physics*, 220(1):139–154, 2006.

[13] J. Zhang, P. C. Johnson, and A. S. Popel. Red blood cell aggregation and dissociation in shear flows simulated by lattice Boltzmann method. *Journal of Biomechanics*, 41(1):47–55, 2008.

[14] P. Bagchi, P. C. Johnson, and A. S. Popel. Computational fluid dynamic simulation of aggregation of deformable cells in a shear flow. *Journal of Biomechanical Engineering*, 127(7):1070–1080, 2005.

[15] M. Fenech, D. Garcia, H. J. Meiselman, and G. Cloutier. A particle dynamic model of red blood cell aggregation kinetics. *Annals of Biomedical Engineering*, 37(11):2299–2309, 2009.

[16] A. Jafari, S. M. Mousavi, and P. Kolari. Numerical investigation of blood flow. Part I: In microvessel bifurcations. *Communications in Nonlinear Science and Numerical Simulation*, 13(8):1615–1626, 2008.

[17] A. Jafari, P. Zamankhan, S. M. Mousavi, and P. Kolari. Numerical investigation of blood flow. Part II: In capillaries. *Communications in Nonlinear Science and Numerical Simulation*, 14(4):1396–1402, 2009.

[18] C. Sun and L. L. Munn. Lattice Boltzmann simulation of blood flow in digitized vessel networks. *Computers & Mathematics With Applications*, 55(7):1594–1600, 2008.

[19] R. Mehri. Micro PIV and Numerical Investigation of a Micro-Couette Blood Flow. Master's thesis, University of Ottawa, Mechanical Engineering Department, 2012.

[20] J. Perkkio and R. Keskinen. Hematocrit reduction in bifurcations due to plasma skimming. *Bulletin of Mathemotical Biology*, 45:41–50, 1983.

[21] P. Galambos and F. Forster. An optical micro-fluidic viscometer. In *ASME International Mechanical Engineering Congress & Exposition*, volume 66, pages 187–191, 1998.

[22] J. Lee and A. Tripathi. Intrinsic viscosity of polymers and biopolymers measured by microchip. *Analytical Chemistry*, 77(22):7137–7147, 2005.

[23] P. Guillot, P. Panizza, J. B. Salmon, M. Joanicot, Colin A., C. H. Bruneau, and T. Colin. Viscosimeter on a microfluidic chip. *Langmuir*, 22(14):6438–6445, 2006.

[24] S. Choi and J-K. Park. Microfluidic rheometer for characterization of protein unfolding and aggregation in microflows. *Small*, 6(12):1306–1310, 2010.

[25] D. E. Solomon and S. A. Vanapalli. Multiplexed microfluidic viscometer for high-throughput complex fluid rheology. *Microfluidics and Nanofluidics*, 16(4):677–690, 2014.

[26] E. Evans and Y. C. Fung. Improved measurements of the erythrocyte geometry. *Microvascular Research*, 4(4):335–347, 1972.

[27] J. Fine L. Waite. *Applied Biofluid Mechanics*, chapter Hematology and Blood Rheology. McGraw-Hill Education, New York, 2007.

[28] M. F. Perutz. Structure of hemoglobin. *Brookhaven Symposia in Biology*, 13:165–183, 1960.

[29] C. Vera, R. Skelton, F. Bossens, and L. Sung. 3-D nanomechanics of an erythrocyte junctional complex in equibiaxial and anisotropic deformations. *Annals of Biomedical Engineering*, 33:1387–1404.

[30] N. Mohandas and P. G. Gallagher. Red cell membrane: past, present, and future. *Blood*, 112(10):3939–3948, 2008.

[31] S. Chien, K. L. Sung, R. Skalak, S. Usami, and A. Tözeren. Theoretical and experimental studies on viscoelastic properties of erythrocyte membrane. *Biophysical Journal*, 24(2):463–487, 1978.

[32] E. A. Evans and R. M. Hochmuth. Membrane viscoplastic flow. *Biophysical Journal*, 16(1):13–26, 1976.

[33] R. Skalak, N. Ozkaya, and T. C. Skalak. Biofluid mechanics. *Annual Review of Fluid Mechanics*, 21(1):167–200, 1989.

[34] R. Fåhraeus. The suspension stability of the blood. *Physiological Reviews*, 9(2):241–274, 1929.

[35] M. H. Knisely. The settling of sludge during life. First observations, evidences, and significances. A contribution to the biophysics of disease. *Acta Anatomica. Supplementum*, 44(41):1–64, 1961.

[36] F. Harding and M. H. Knisely. Settling of sludge in human patients; a contribution to the biophysics of disease. *Angiology*, 9(6):317–341, 1958.

[37] M. H. Knisely, E. H. Bloch, T. S. Eliot, and L. Warner. Sludged blood. *Science*, 106(2758):431–440, 1947.

[38] R. Malcolm, H.I. Bicher, R. C. Duncan, and M. H. Knisely. Behavioral effects of erythrocyte aggregation. *Microvascular Research*, 4(1):94–97, 1972.

[39] S. Chien and K. M. Jan. Ultrastructural basis of the mechanism of rouleaux formation. *Microvascular Research*, 5(2):155–166, 1973.

[40] B. Neu and H. J. Meiselman. Depletion-mediated red blood cell aggregation in polymer solutions. *Biophysical Journal*, 83(5):2482–2490, 2002.

[41] E. W. Merrill, G. C. Cokelet, A. Britten, and R. E. Wells Jr. Non-Newtonian rheology of human blood–effect of fibrinogen deduced by "subtraction". *Circulation Research*, 13:48–55, 1963.

[42] S. Chien, S. Usami, R. J. Dellenback, and M. I. Gregersen. Shear-dependent interaction of plasma proteins with erythrocytes in blood rheology. *American Journal of Physiology – Legacy Content*, 219(1):143–153, 1970.

[43] H. L. Goldsmith and R. Skalak. Hemodynamics. *Annual Review of Fluid Mechanics*, 7(1):213–247, 1975.

[44] M. Brust, O. Aouane, M. Thiébaud, C. Flormann, D.and Verdier, L. Kaestner, M. W. Laschke, H. Selmi, A. Benyoussef, T. Podgorski, G. Coupier, C. Misbah, and C. Wagner. The plasma protein fibrinogen stabilizes clusters of red blood cells in microcapillary flows. *Scientific Reports*, 4(4348):1–6, 2014.

[45] O. K. Baskurt, B. Neu, and H. J. Meiselman. *Red Blood Cell Aggregation*. CRC Press, Boca Raton, 2011.

[46] S. Kim, A. S. Popel, M. Intaglietta, and P. C. Johnson. Aggregate formation of erythrocytes in postcapillary venules. *American Journal of Physiology - Heart and Circulatory Physiology*, 288(2):H584–H590, 2005.

[47] S. Kim, J. Zhen, A. S. Popel, M. Intaglietta, and P. C. Johnson. Contributions of collision rate and collision efficiency to erythrocyte aggregation in postcapillary venules at low flow rates. *American Journal of Physiology - Heart and Circulatory Physiology*, 293(3):H1947–H1954, 2007.

[48] O. K. Baskurt. *Handbook of Hemorheology and Hemodynamics*. Biomedical and Health Research. IOS Press, Amsterdam, 2007.

[49] I. Cicha, Y. Suzuki, N. Tateishi, and N. Maeda. Changes of RBC aggregation in oxygenation-deoxygenation: pH dependency and cell morphology. *American Journal of Physiology - Heart and Circulatory Physiology*, 284(6):H2335–42, 2003.

[50] H. J. Meiselman. Red blood cell role in RBC aggregation: 1963-1993 and beyond. *Clinical Hemorheology*, (5):575–592, 1993.

[51] J. Barbee. Concentration reduction and dilatant flow behavior in suspensions of hardened human red cells. *Transactions of the Society of Rheology*, 17(3):413–423, 1973.

[52] F. J. Neumann, H. Schmid-Schönbein, and H. Ohlenbusch. Temperature-dependence of red cell aggregation. *Pflügers Archiv*, 408(5):524–530.

[53] E. Biernacki. Samoistna sedymentacja krwi jako naukowa, praktyczno-kliniczna metoda badania. *Gazeta Lekarska*, 17:962–996, 1897.

[54] J. Mayer, Z. Pospisil, and J. Litzman. The mechanism of erythrocyte sedimentation in Westergren's examination. *Biorheology*, 29(2-3):261–271, 1992.

[55] M. W. Rampling. Red cell aggregation and yield stress. *Clinical Blood Rheology, CRC Press, Boca Raton, FL*, 1988.

[56] G. Potron, D. Jolly, P. Nguyen, J. L. Mailliot, and B. Pignon. Approach to erythrocyte aggregation through erythrocyte sedimentation rate: application of a statistical model in pathology. *Nouvelle revue francaise d'hématologie*, 36(3):241–247, 1994.

[57] O. K. Baskurt, M. Uyuklu, P. Ulker, M. Cengiz, N. Nemeth, T. Alexy, S. Shin, M. R. Hardeman, and H. J. Meiselman. Comparison of three instruments for measuring red blood cell aggregation. *Clinical Hemorheology and Microcirculation*, 43(4):283–298, 2009.

[58] T. Alexy, R. B. Wenby, E. Pais, L. J. Goldstein, W. Hogenauer, and H. J. Meiselman. An automated tube-type blood viscometer: Validation studies. *Biorheology*, (3):237, 2005.

[59] P. Foresto, M. D'Arrigo, L. Carreras, R. E. Cuezzo, J. Valverde, and R. Rasia. Evaluation of red blood cell aggregation in diabetes by computerized image analysis. *Medicina*, 60(5 Pt 1):570–572, 2000.

[60] R. Rotstein, R. Fusman, D. Zeltser, I. Shapira, E. Shabtai, D. Avitzour, N. Sadees, D. Levartovsky, N. Arber, A. Eldor, and S. Berliner. The picture of inflammation: a new concept that combines the white blood cell count and erythrocyte sedimentation rate into a new hematologic diagnostic modality. *Acta Haematologica*, 106(3):106–114, 2001.

[61] S. Ramakrishnan A. Kavitha. Assessment of human red blood cell aggregation using image processing and wavelets. *Measurement Science Review*, 7(5), 2007.

[62] O. K. Baskurt, M. Boynard, G. C. Cokelet, P. Connes, B. M. Cooke, S. Forconi, F. Liao, M. R. Hardeman, F. Jung, H. J. Meiselman, G. Nash, N. Nemeth, B. Neu, B. Sandhagen, S. Shin, G. Thurston, J. L. Wautier, and International Expert Panel for Standardization of Hemorheological Methods. New guidelines for hemorheological laboratory techniques. *Clinical Hemorheology and Microcirculation*, 42(2):75–97, 2009.

[63] K. K. Shung and G. A. Thieme. *Ultrasonic Scattering in Biological Tissues*. CRC Press, Boca Raton, 1992.

[64] G. Cloutier and Z. Qin. Shear rate dependence of ultrasound backscattering from blood samples characterized by different levels of erythrocyte aggregation. *Annals of Biomedical Engineering*, 28:399–407, 2000.

[65] R. Fåhraeus and T. Lindqvist. The viscosity of the blood in narrow capillary tubes. *American Journal of Physiology – Legacy Content*, 96(3):562–568, 1931.

[66] A. R. Pries and T. W. Secomb. Rheology of the microcirculation. *Clinical Hemorheology and Microcirculation*, 29(3-4):143–148, 2003.

[67] A. S. Popel and P. C. Johnson. Microcirculation and hemorheology. *Annual Review of Fluid Mechanics*, 37:43–69, 2005.

[68] H. L. Goldsmith. Red cell motions and wall interactions in tube flow. *Federation Proceedings*, 30(5):1578–1590, 1971.

[69] H. L. Goldsmith. The microrheology of red blood cell suspensions. *The Journal of General Physiology*, 52(1):5–28, 1968.

[70] G. R. Cokelet and H. L. Goldsmith. Decreased hydrodynamic resistance in the two-phase flow of blood through small vertical tubes at low flow rates. *Circulation Research*, 68(1):1–17, 1991.

[71] J. H. Barbee and G. R. Cokelet. Prediction of blood flow in tubes with diameters as small as 29 μ. *Microvascular Research*, 3(1):17 – 21, 1971.

[72] M. Reiner. *Rhéologie théorique*. Dunod, Paris, 1955.

[73] R. B. Bird. Useful non-Newtonian models. *Annual Review of Fluid Mechanics*, 8(1):13–34, 1976.

[74] S. Kim. *A Study of Non-Newtonian Viscosity and Yield Stress of Blood in a Scanning Capillary-Tube Rheometer*. PhD thesis, Drexel University, 2002.

[75] B. M. Johnston, P. R. Johnston, S. Corney, and D. Kilpatrick. Non-Newtonian blood flow in human right coronary arteries: steady state simulations. *Journal of Biomechanics*, 37(5):709–720, 2004.

[76] E. C. Bingham. *An Investigation of the Laws of Plastic Flow*. Bulletin of the Bureau of Standards. US. Govt. Print. Off., Washington, 1917.

[77] F. Caton. The sol-gel transition of blood. Presented at the Workshop Agrégation érythrocytaire & écoulement sanguin, Marseille, France, 2015.

[78] N. Casson. A flow equation for pigment-oil suspensions of the printing ink type. *Rheology of Disperse Systems*, 1959.

[79] Y. I. Cho and K. R. Kensey. Effects of the non-Newtonian viscosity of blood on flows in a diseased arterial vessel. Part 1: Steady flows. *Biorheology*, 28(3-4):241–262, 1991.

[80] K. Yasuda. *Investigation of the Analogies Between Viscometric and Linear Viscoelastic Properties of Polystyrene Fluids*. PhD thesis, Massachusetts Institute of Technology, Dept. of Chemical Engineering, 1979.

[81] F. J. Walburn, D. J. Schneck, and American Society of Mechanical Engineers. A constitutive equation for whole human blood. *Bioengineering Division. Winter Annual Meeting*, 1975.

[82] W. Herschel and R. Bulkley. Konsistenzmessungen von gummi-benzollösungen. *Colloid & Polymer Science*, 39:291–300.

[83] M. Bureau, J. C. Healy, D. Bourgoin, and M. Joly. Rheological hysteresis of blood at low shear rate. *Biorheology*, 17(1-2):191–203, 1980.

[84] R. G. Owens. A new microstructure-based constitutive model for human blood. *Journal of Non-Newtonian Fluid Mechanics*, 140(1-3):57–70, 2006.

[85] S. Novais, D. Pinho, D. Bento, E. Pinto, T. Yaginuma, C. S. Fernandes, V. Garcia, A. I. Pereira, J. Lima, M. Mujika, R. Dias, S. Arana, and R. Lima. *Visualization and Simulation of Complex Flows in Biomedical Engineering*, volume 12 of *Lecture Notes in Computational Vision and Biomechanics*, chapter Cell-Free Layer (CFL) Measurements in Complex Geometries: Contractions and Bifurcations, pages 119–132. Springer, Dordrecht, Heidelberg, London, New York, 2013.

[86] T. W. Secomb. *Modeling and Simulation of Capsules and Biological Cells*, chapter Mechanics of red blood cells and blood flow in narrow tubes, pages 163–198. Chapman & Hall/CRC, Boca Raton, 2003.

[87] C. Pozrikidis. Numerical simulation of the flow-induced deformation of red blood cells. *Annals of Biomedical Engineering*, 31:1194–1205, 2003.

[88] C. Pozrikidis. *Computational Hydrodynamics of Capsules and Biological Cells*. Chapman and Hall/CRC mathematical & computational biology series. CRC Press, Boca Raton, 2010.

[89] C. S. Peskin. Numerical analysis of blood flow in the heart. *Journal of Computational Physics*, 25(3):220–252, 1977.

[90] S. Li and W.K. Liu. *Meshfree Particle Methods*. Springer, Berlin, Heidelberg, New York, 2004.

[91] C. D. Eggleton and A. S. Popel. Large deformation of red blood cell ghosts in a simple shear flow. *Physics of Fluids*, 10(8):1834–1845, 1998.

[92] P. Bagchi. Mesoscale simulation of blood flow in small vessels. *Biophysical Journal*, 92(6):1858–1877, 2007.

[93] G. Tryggvason, B. Bunner, A. Esmaeeli, D. Juric, N. Al-Rawahi, W. Tauber, J. Han, S. Nas, and Y.-J. Jan. A front-tracking method for the computations of multiphase flow. *Journal of Computational Physics*, 169(2):708–759, 2001.

[94] C. Sun and L. L. Munn. Particulate nature of blood determines macroscopic rheology: A 2-D Lattice Boltzmann analysis. *Biophysical Journal*, 88(3):1635 – 1645, 2005.

[95] P. L. Bhatnagar, E. P. Gross, and M. Krook. A model for collision processes in gases. I. Small amplitude processes in charged and neutral one-component systems. *Physical Review*, 94:511–525, 1954.

[96] A. Iolov, A. S. Kane, Y. Bourgault, R. G. Owens, and A. Fortin. A finite element method for a microstructure-based model of blood. *International Journal for Numerical Methods in Biomedical Engineering*, 27(9):1321–1349, 2011.

[97] D. A. Fedosov, B. Caswell, and Karniadakis G. E. A multiscale red blood cell model with accurate mechanics, rheology, and dynamics. *Biophysical Journal*, 98(10):2215–2225, 2010.

[98] D. A. Fedosov, H. Noguchi, and Gompper G. Multiscale modeling of blood flow: from single cells to blood rheology. *Biomechanics and Modeling in Mechanobiology*, 13(2):239–258, 2013.

[99] W. Deuling and H. J. Helfrich. Red blood cell shapes as explained on the basis of curvature elasticity. *Biophysical Journal*, 16(8):861–868, 1976.

[100] W. Pan, B. Caswell, and G. E. Karniadakis. A low-dimensional model for the red blood cell. *Soft Matter*, 6:4366–4376, 2010.

[101] X. Li, A. S. Popel, and G. E. Karniadakis. Blood-plasma separation in Y-shaped bifurcating microfluidic channels: a dissipative particle dynamics simulation study. *Physical Biology*, 9(2):026010, 2012.

[102] D. Xu, E. Kaliviotis, A. Munjiza, E. Avital, C. Ji, and J. Williams. Large scale simulation of red blood cell aggregation in shear flows. *Journal of Biomechanics*, 46(11):1810 – 1817, 2013.

[103] G. Bugliarello and J. W. Hayden. High-speed microcinematographic studies of blood flow *in vitro*. *Science*, 138(3544):981–983, 1962.

[104] P. Gaehtgens, H. J. Meiselman, and H. Wayland. Velocity profiles of human blood at normal and reduced hematocrit in glass tubes up to 130 μ diameter. *Microvascular Research*, 2(1):13 – 23, 1970.

[105] M. Baker. *Double-slit Photometric Measurement of Velocity Profiles for Blood in Microvessels and Capillary Tubes*. PhD thesis, California Institute of Technology, year = 1972.

[106] S. Einav, J. Avidor, and B. Vidne. Haemodynamics of coronary artery - saphenous vein bypass. *Journal of Biomedical Engineering*, 7(4):305 – 309, 1985.

[107] C Tropea. Laser doppler anemometry: recent developments and future challenges. *Measurement Science and Technology*, 6(6):605, 1995.

[108] R. Lima, S. Wada, M. Takeda, K. Tsubota, and T. Yamaguchi. *In vitro* confocal micro-PIV measurements of blood flow in a square microchannel: The effect of the haematocrit on instantaneous velocity profiles. *Journal of Biomechanics*, 40(12):2752 – 2757, 2007.

[109] J. G. Santiago, S. T. Wereley, C. D. Meinhart, D. J. Beebe, and R. J. Adrian. A particle image velocimetry system for microfluidics. *Experiments in Fluids*, 25(4):316–319, 1998.

[110] B. J. Kim, Y. Z. Liu, and H. J. Sung. Micro PIV measurement of two-fluid flow with different refractive indices. *Measurement Science and Technology*, 15(6):1097–1103, 2004.

[111] C. D. Meinhart, S. T. Wereley, and M. H. B. Gray. Volume illumination for two-dimensional particle image velocimetry. *Mechanical Engineering*, 11(6):809–814, 2000.

[112] S. T. Wereley, L. Gui, and C. D. Meinhart. Advanced algorithms for microscale particle image velocimetry. *AIAA Journal*, 40(6):1047–1055, 2002.

[113] H. Becker and L. E. Locascio. Polymer microfluidic devices. *Talanta*, 56(2):267 – 287, 2002.

[114] K. Pitts and M. Fenech. Blood velocity profile measurements in microchannels using micro-particle image velocimetry. In *Proceedings of the ASME 2012 10th International Conference on Nanochannels, Microchannels, and Minichannels*, 2012.

[115] H. Wayland and P. C. Johnson. Erythrocyte velocity measurement in microvessels by a two-slit photometric method. *Journal of Applied Physiology*, 22(2):333–337, 1967.

[116] C. D. Meinhart, S. T. Wereley, and J. G. Santiago. PIV measurements of a microchannel flow. *Experiments in Fluids*, 27(5):414–419, 1999.

[117] M. Raffel, C. E. Willert, and J. Kompenhans. *Particle Image Velocimetry: a Practical Guide*. Springer-Verlag, Berlin, 1998.

[118] J. Westerweel. Fundamentals of digital particle image velocimetry. *Measurement Science and Technology*, 8:1379–1392, 1997.

[119] R. J. Adrian. Twenty years of particle image velocimetry. *Experiments in Fluids*, 39(2):159–169, 2005.

[120] H. Bruus. *Development of micro-PIV Techniques for Applications in Microfluidic Systems*. PhD thesis, Technical University of Denmark, 2008.

[121] A. Kloosterman, C. Poelma, and J. Westerweel. Flow rate estimation in large depth-of-field micro-PIV. *Experiments in Fluids*, 50(6):1587–1599, 2011.

[122] M. G. Olsen and R. J. Adrian. Out-of-focus effects on particle image visibility and correlation in microscopic particle image velocimetry. *Experiments in Fluids*, 29(1):S166–S174, 2000.

[123] Y. Sugii, K. Okamoto, S. Nishio, and A. Nakano. Evaluation of velocity measurement in micro tube by highly accurate piv technique. In *4 th International Symposium on Particle Image Velocimetry(PIV'01)*, pages 1–5, 2001.

[124] L. Bitsch, L. H. Olesen, C. H. Westergaard, H. Bruus, H. Klank, and J. P. Kutter. Micro particle-image velocimetry of bead suspensions and blood flows. *Experiments in Fluids*, 39(3):507–513, 2005.

[125] K. Pitts, R. Mehri, M. Fenech, and C. Mavriplis. Micro-particle image velocimetry measurement of blood flow: Validation and analysis of data pre-processing and processing methods. *Measurement Science and Technology*, 23(10):105302, 2012.

[126] L. Gui and S. T. Wereley. A correlation-based continuous window-shift technique to reduce the peak-locking effect in digital PIV image evaluation. *Experiments in Fluids*, 32(4):506–517, 2002.

[127] C. V. Nguyen, A. Fouras, and J. Carberry. Improvement of measurement accuracy in micro PIV by image overlapping. *Experiments in Fluids*, 49(3):701–712, 2010.

[128] Y. Sugii, R. Okuda, K. Okamoto, and H. Madarame. Velocity measurement of both red blood cells and plasma of *in vitro* blood flow using high-speed micro PIV technique. *Measurement Science and Technology*, 16(5):1126, 2005.

[129] R. Lima, S. Wada, K. Tsubota, and T. Yamaguchi. Confocal micro-PIV measurements of three-dimensional profiles of cell suspension flow in a square microchannel. *Measurement Science and Technology*, 17(4):797, 2006.

[130] W. Yang, A. B. Kostinski, and R. A. Shaw. Phase signature for particle detection with digital in-line holography. *Optics Letters*, 31(10):1399–1401, 2006.

[131] C. Willert. Stereoscopic digital particle image velocimetry for application in wind tunnel flows. *Measurement Science and Technology*, 8(12):1465, 1997.

[132] R. Lima, S. Wada, S. Tanaka, M. Takeda, T. Ishikawa, K. Tsubota, Y. Imai, and T. Yamaguchi. *In vitro* blood flow in a rectangular PDMS microchannel: experimental observations using a confocal micro-PIV system. *Biomedical Microdevices*, 10(2):153–167, 2008.

[133] S. K. Sia. Microfluidic devices fabricated in poly(dimethylsiloxane) for biological studies. *Electrophoresis*, 24(21):3563–3576, 2003.

[134] B. S. Hardy, K. Uechi, J. Zhen, and H. Pirouz Kavehpour. The deformation of flexible PDMS microchannels under a pressure driven flow. *Lab on a chip*, 9(7):935–938, 2009.

[135] A. H. Ng, U. Uddayasankar, and A. R. Wheeler. Immunoassays in microfluidic systems. *Analytical and Bioanalytical Chemistry*, 397(3):991–1007, 2010.

[136] Y. H. Dou, N. Bao, J. J. Xu, F. Meng, and H. Y. Chen. Separation of proteins on surface-modified poly(dimethylsiloxane) microfluidic devices. *Electrophoresis*, 25(17):3024–3031, 2004.

[137] J. Zhou, A. Vera Ellis, and N. H. Voelcker. Recent developments in PDMS surface modification for microfluidic devices. *Electrophoresis*, 31(1):2–16, 2010.

[138] J. Krüger, K. Singh, A. O'Neill, C. Jackson, A. Morrison, and P. O'Brien. Development of a microfluidic device for fluorescence activated cell sorting. *Journal of Micromechanics and Microengineering*, 12(4):486, 2002.

[139] S. R. Whittaker and F. R. Winton. The apparent viscosity of blood flowing in the isolated hindlimb of the dog, and its variation with corpuscular concentration. *The Journal of Physiology*, 78(4):339–369, 1933.

[140] R. Y. Chen, R. D. Carlin, S. Simchon, K. M. Jan, and S. Chien. Effects of dextran-induced hyperviscosity on regional blood flow and hemodynamics in dogs. *The American Journal of Physiology*, 256(3 Pt 2):H898–905, 1989.

[141] A. M. Benis, S. Usami, and S. Chien. Effect of hematocrit and inertial losses on pressure-flow relations in the isolated hindpaw of the dog. *Circulation Research*, 27(6):1047–1068, 1970.

[142] J. J. Durussel, M. F. Berthault, G. Guiffant, and J. Dufaux. Effects of red blood cell hyperaggregation on the rat microcirculation blood flow. *Acta Physiologica Scandinavica*, 163(1):25–32, 1998.

[143] O. Yalcin, M. Uyuklu, J. K. Armstrong, H. J. Meiselman, and O. K. Baskurt. Graded alterations of RBC aggregation influence *in vivo* blood flow resistance. *American Journal of Physiology - Heart and Circulatory Physiology*, 287(6):H2644–50, 2004.

[144] M. Cabel, H. J. Meiselman, A. S. Popel, and P. C. Johnson. Contribution of red blood cell aggregation to venous vascular resistance in skeletal muscle. *The American Journal of Physiology*, 272(2 Pt 2):H1020–32, 1997.

[145] J. J. Bishop, P. R. Nance, A. S. Popel, M. Intaglietta, and P. C. Johnson. Effect of erythrocyte aggregation on velocity profiles in venules. *American Journal Physiology - Heart and Circulatory Physiology*, 280(1):H222–H236, 2001.

[146] J. J. Bishop, A. S. Popel, M. Intaglietta, and P. C. Johnson. Effect of aggregation and shear rate on the dispersion of red blood cells flowing in venules. *American Journal of Physiology - Heart and Circulatory Physiology*, 283(5):H1985–H1996, 2002.

[147] J. J. Bishop, A. S. Popel, M. Intaglietta, and P. C. Johnson. Effects of erythrocyte aggregation and venous network geometry on red blood cell axial migration. *American Journal of Physiology - Heart and Circulatory Physiology*, 281(2):H939–H950, 2001.

[148] J. J. Bishop, P. R. Nance, A. S. Popel, M. Intaglietta, and P. C. Johnson. Relationship between erythrocyte aggregate size and flow rate in skeletal muscle venules. *American Journal of Physiology - Heart and Circulatory Physiology*, 286(1):H113–H120, 2004.

[149] LaVision. Imager intense. http://www.lavision.de/en/techniques/piv.php.

[150] J. Boudreau. Co-op report, University of Ottawa, 2015.

[151] Micro-Chem. $NANO^{TM}$ SU-8 Negative Tone Photoresists Formulation 50 & 100.

[152] M. A. Eddings, M. A. Johnson, and B. G. Gale. Determining the optimal PDMS-PDMS bonding technique for microfluidic devices. *Journal of Micromechanics and Microengineering*, 18(6):067001, 2008.

[153] S. Bhattacharya, A. Datta, J. M. Berg, and S. Gangopadhyay. Studies on surface wettability of poly(dimethyl) siloxane (PDMS) and glass under oxygen-plasma treatment and correlation with bond strength. *Journal of Microelectromechanical Systems*, 14(3):590–597, June 2005.

[154] P. J. Stiles and D. F. Fletcher. Hydrodynamic control of the interface between two liquids flowing through a horizontal or vertical microchannel. *Lab Chip*, 4:121–124, 2004.

[155] F. Neuwald. Rheological studies of new cream of bases with the Brookfield Synchro-Lectric viscometer. *Journal of the Society of Cosmetic Chemists*, 17(4):213–233, 1966.

[156] J. Chevalier and F. Ayela. Microfluidic on chip viscometers. *Review of Scientific Instruments*, 79(7):076102–1–076102–3, 2008.

[157] J. W. Lottes P. F. Fischer and S. G. Kerkemeier. nek5000 Web page, 2008. http://nek5000.mcs.anl.gov.

[158] A. T. Patera. A spectral element method for fluid dynamics: Laminar flow in a channel expansion. *Journal of Computational Physics*, 54(3):468–488, 1984.

[159] P. F. Fischer and J. W. Lottes. *Domain Decomposition Methods in Science and Engineering*, chapter Hybrid Schwarz-Multigrid Methods for the Spectral Element Method: Extensions to Navier-Stokes, pages 35–49. Springer, Berlin, Heidelberg, 2005.

[160] Y. Maday and A. T. Patera. Spectral element methods for the incompressible Navier–Stokes equations. In A. K. Noor and J. T. Oden, editors, *State-of-the-art Surveys on Computational Mechanics*, pages 71–142, New York, 1989. ASME.

[161] P. Gervasio and F. Saleri. Stabilized spectral element approximation for the Navier–Stokes equations. *Numerical Methods for Partial Differential Equations*, 14(1):115–141, 1998.

[162] M. Laporte, R. Mehri, and C. Mavriplis. Non-Newtonian simulations for the design of a micro-Couette blood flow device. Presented at the 23rd Annual Conference of the Computational Fluid Dynamics Society of Canada, Waterloo, Ontario, Canada, 2015.

[163] B. J. Briscoe, P. F. Luckham, and S. R. Ren. An assessment of a rolling-ball viscometer for studying non-Newtonian fluids. *Colloids and Surfaces*, 62(1):153–162, 1992.

[164] Dow Corning Inc. *POLYOX^{TM} Water-Soluble Resins Dissolving Techniques*, 2003.

[165] P. Tabeling. *Introduction to Microfluidics*. Oxford University Press, Oxford, 2005.

[166] C. A. Schneider, W. S. Rasband, and K. W. Eliceiri. NIH image to ImageJ: 25 years of image analysis. *Nature Methods*, 9:671–675, 2012.

[167] Potters Industries Inc., Engineered glass material division. *SPHERICELL® Typical Product Characteristics*, 2011.

[168] R. Mehri, C. Mavriplis, and M. Fenech. Design of a microfluidic system for red blood cell aggregation investigation. *Journal of Biomechanical Engineering*, 136(6):064501, 2014.

[169] S. Shin, Y. Yang, and J. S. Suh. Measurement of erythrocyte aggregation in a microchip stirring system by light transmission. *Clinical Hemorheology and Microcirculation*, 41(3):197–207, 2009.

[170] R. Mehri, C. Mavriplis, and M. Fenech. Controlled microfluidic environment for dynamic investigation of red blood cell aggregation. *Journal of Visualized Experiments*, (100):e52719, 2015.

[171] B. M. Johnston, P. R. Johnston, S. Corney, and D. Kilpatrick. Non-Newtonian blood flow in human right coronary arteries: Steady state simulations. *Journal of Biomechanics*, 37(5):709–720, 2004.

[172] C. H. Hsu, H. H. Vu, and Y. H. Kang. The rheology of blood flow in a branched arterial system with three-dimensional model: A numerical study. *Journal of Mechanics*, 25:N21–N24, 2009.

[173] R. Mehri, J. Laplante, C. Mavriplis, and M. Fenech. Investigation of blood flow analysis and red blood cell aggregation. *Journal of Medical and Biological Engineering*, 34(5):469–474, 2014.

[174] J. J. Moré. *Numerical Analysis*, chapter The Levenberg-Marquardt Algorithm: Implementation and Theory, pages 105–116. Lecture Notes in Mathematics. Springer, Berlin, Heidelberg, 1977.

[175] A. Spiess and N. Neumeyer. An evaluation of R^2 as an inadequate measure for nonlinear models in pharmacological and biochemical research: A Monte Carlo approach. *BioMed Central Pharmacology*, 10(6):1–11, 2010.

[176] G. Késmárky, P. Kenyeres, M. Rábai, and K. Tóth. Plasma viscosity: A forgotten variable. *Clinical Hemorheology and Microcirculation*, 41:243–246, 2009.

[177] S. S. Shibeshi and W. E. Collins. The rheology of blood flow in a branched arterial system. *Applied Rheology*, 15(6):398–405, 2005.

[178] E. Kaliviotis and M. Yianneskis. On the effect of microstructural changes of blood on energy dissipation in Couette flow. *Clinical Hemorheology and Microcirculation*, 39:235–242, 2008.

[179] *Measurement in Fluid Mechanics*, chapter Measurement uncertainty, pages 45–54. Cambridge University Press, New York, 2009.

[180] The Specialist Committee on Uncertainty Analysis. 2008 recommended procedures and guidelines - uncertainty analysis of particle image velocimetry. Technical report, 25th International Towing Tank Conference, 2008.

[181] O. Gliah, R. Mehri, and M. Fenech. Determination of the cell free layer thickness in PDMS microchannels: Experimental investigation. Manuscript in preparation, 2016.

[182] R. F. Tuma, W. N. Durán, and K. Ley. *Microcirculation*. Handbook of Physiology. Academic Press, San Diego, Burlington, London, Amsterdam, 2011.

[183] J. Laplante, R. Mehri, and C. Mavriplis. Spectral element grid generation and numerical simulation for blood microcirculation. *22nd Annual Conference of the CFD Society of Canada*. 2014.